Water in Confined Geometry of Carbon Nanomaterials

: Structure, Dynamics, and Phase Behavior

Haruka Kyakuno

Department of Physics, Graduate School of Science and Engineering, Tokyo Metropolitan University
1-1 Minami-Osawa, Hachioji, Tokyo 192-0397, Japan

February 2014

Contents

Chapter 1

Introduction

Water is one of the most familiar and crucial substances for humans. It exists everywhere on earth including our bodies. Actually, 71% of the earth's surface is covered with water. The total volume of water on earth is estimated to be about 1.4×10^{18} m^3, wherein 96.5% in oceans, 1.69% underground, 1.76% in glaciers, 0.0265% in lakes and rivers, 0.0009% in the air as vapor, and 0.0001% within living bodies. For us, humans, water accounts for about 70-80% of our bodies and plays a crucial role in maintaining our vital activities, such as metabolic processes, protein functionality, chemical reactions, blood circulation, and transport of biochemical. It also has a huge effect on our daily lives and environments: climate, agriculture, industry, engineering, and so on.

Meanwhile, it is not only a ubiquitous substance, but also has plenty of mysterious properties such as the density maximum at 277 K.[1-5] That is why it has attracted the interest of many researchers for so long and various hypotheses have been developed to solve the mysteries.[6-10] It is known that the anomalous properties of liquid water are more pronounced when supercooled.[1-3] For example, thermodynamic response functions and characteristic relaxation times appear to diverge at a singularity temperature.[1-3] The origin of this behavior has not been fully understood so far. Moreover, upon rapid cooling, experimental studies have revealed the presence of at least two amorphous phases in water: low density amorphous

ice (LDA) and high density amorphous ice (HDA).[1, 2, 8] Furthermore, LDA and HDA are expected to connect to two liquid states, low density liquid (LDL) and high density liquid (HDL), under supercooled regime, respectively.[1-3, 8] Although the idea seems to hold the key to solve overall mysteries of water, the experimental studies are hampered by 'no man's land' region in temperature-pressure (T-P) plane, wherein supercooled water crystallizes immediately. [1-3, 8] Accordingly, alternative approaches have been attempted using nano-confined water[11-17] and aqueous solutions[18-22], wherein the "supercooled state" or liquid state is stabilized even below the freezing temperature of bulk water.

In the present study, we thus focused on nano-confined water inside carbon nanomaterials, namely, single-walled carbon nanotubes (SWCNTs)[23] and zeolite-templated carbon (ZTC)[24]. A great advantage of using SWCNTs is their controllable diameters. It may be expected that systematic studies with SWCNTs of various diameters (D) clarify the structure, dynamics and phase behavior of water which link to the bulk region.

In previous studies, structures and phase transitional behavior of water inside SWCNTs with $1.17 < D < \sim 1.4$ nm have been revealed by powder X-ray diffraction (XRD) experiments[25-28] as well as molecular dynamics (MD) simulations[29-31]. It was found that the confined water undergoes a liquid-solid like transition and forms tubule ice structures, ice nanotubes (ice NTs). On the other hand, studies with thicker SWCNTs were carried out very recently. However, few experimental studies have been done until now.

In this work, we used thicker SWCNTs with $D > \sim 1.4$ nm to establish a

global T-D phase diagram of the confined water as well as to clarify the structure, dynamics and phase behavior linking to those in the bulk region. As for ZTC, this is the first report on its water adsorption properties. ZTC would provide a new platform to study three-dimensional "supercooled" water.

Chapter 2

What is Water?

2.1. Water in Bulk

2.1.1. Water as a Molecule

A water molecule consists of two hydrogen atoms covalently bonded to one oxygen atom, as shown in **Fig. 2.1 (a)**. Water is a polar molecule with an electrical dipole moment, and interacts with different water molecules through hydrogen bonding. For example, each water molecule in ordinary hexagonal ice (Ih) has four nearest neighbors and the hydrogen bonds sustain the tetrahedrally coordinated network of the ice. In ice Ih, the O-O distance is 2.76 Å, and the OOO angle is 109.4° at 223 K, comfortably close to the ideal tetrahedral angle of 109.47° and the average HOH angle of the individual water molecule of 104.52°.[32] **Figure 2.1 (b)** shows the structure of ice Ih. Because of the strong directionality of the hydrogen bonds, ice Ih has open channels through the structure. The strength of a hydrogen bond is about 20 kJ/mol.[1, 32] This is intermediate between a simple van der Waals interaction and an ionic interaction. It is equivalent to approximately 10 times a typical thermal fluctuation at room temperature. The heat of fusion of ice Ih at atmospheric pressure is 6.0 kJ/mol,[32] implying that the majority of hydrogen bonds do not break upon melting. Thus, liquid water close to the melting point has local tetrahedral symmetry, although this order is transient and short-ranged.

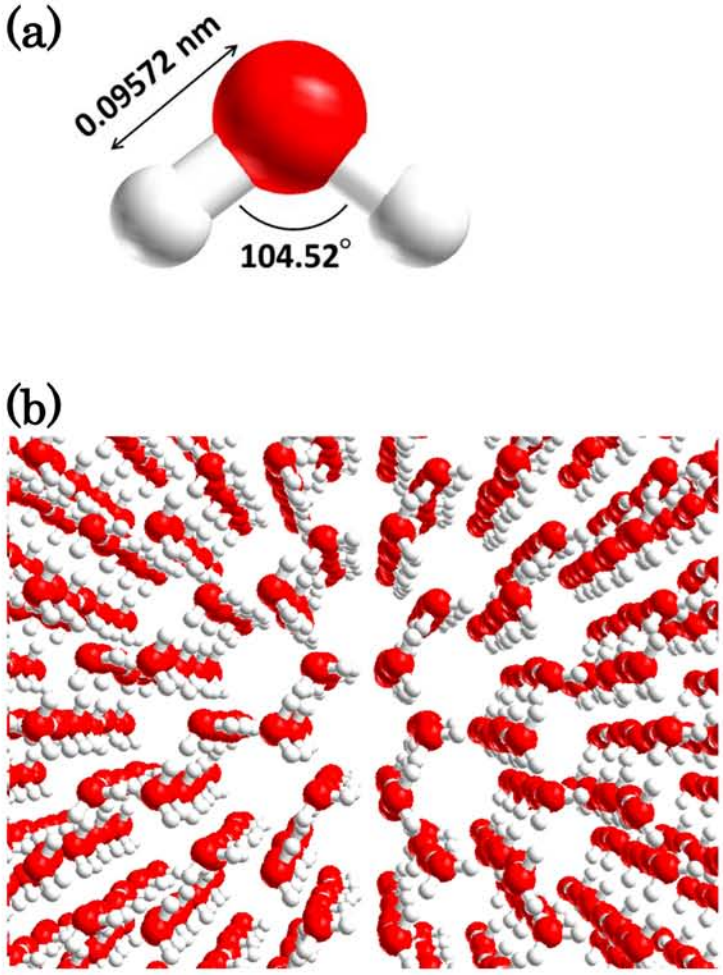

Figure 2.1. Water molecule and ice Ih. (a) The geometry of a water molecule. Red and white spheres represent oxygen (O) and hydrogen (H) atoms, respectively. The O-H bond length and HOH angle presented in the figure is from ref. 32. (b) Structure of ice Ih. Although the positions of hydrogen atoms are ordered in the figure, they are disordered in a real system.

2.1.2. Anomalous Properties of Water

Water is not only a ubiquitous substance, but also has a number of anomalous properties.[1-5] That is why it attracts the interest of many researchers for so long. For example, it is the only chemical compound that occurs naturally in all three states of matter (solid, liquid and vapor). The dielectric constant of liquid water is unusually large. In the crystalline state, it can exist in thirteen different crystalline forms (**Fig. 2.2**). This is called 'polymorphism of ice'. It is known that ices II, III, V, VI, VII, VIII, X, XI and Ih are stable over a certain range of temperature and pressure, while ices IV, IX, XII and cubic ice (Ic) are metastable.[1, 32] Moreover, water can be cooled even below its freezing point without crystallization (supercooled).

Before discussing in detail the anomalous properties of water in supercooled regime, we shall start reviewing some of their behaviors in the stable liquid range in the T-P plane. In water, unlike typical liquids, isothermal compressibility (K_T) and isobaric heat capacity (c_p) increase below 319 K and 308 K, respectively, and thermal expansion coefficient (α) becomes negative below 277 K at ambient pressure.[1-3] **Figure 2.3** shows the comparison of these thermodynamic response functions between water and a simple liquid. These dramatic changes have a close relation to fluctuation of volume and entropy upon cooling.[1-3] In most liquids, volume and entropy fluctuations become smaller with lowering temperature, and are positively correlated: a decrease in volume results in a decrease in entropy. In water, on the other hand, volume and entropy fluctuations become more pronounced as the temperature decreases, and are anti-correlated below 277 K. Here, the

anti-correlation is caused by the formation of an open hydrogen bonded network, wherein a decrease in orientational entropy is accompanied by a volume increase. Since K_T, c_p, and α reflect the volume fluctuation, entropy fluctuation, and the correlation between volume and entropy fluctuation, respectively, they show dramatic changes upon cooling.

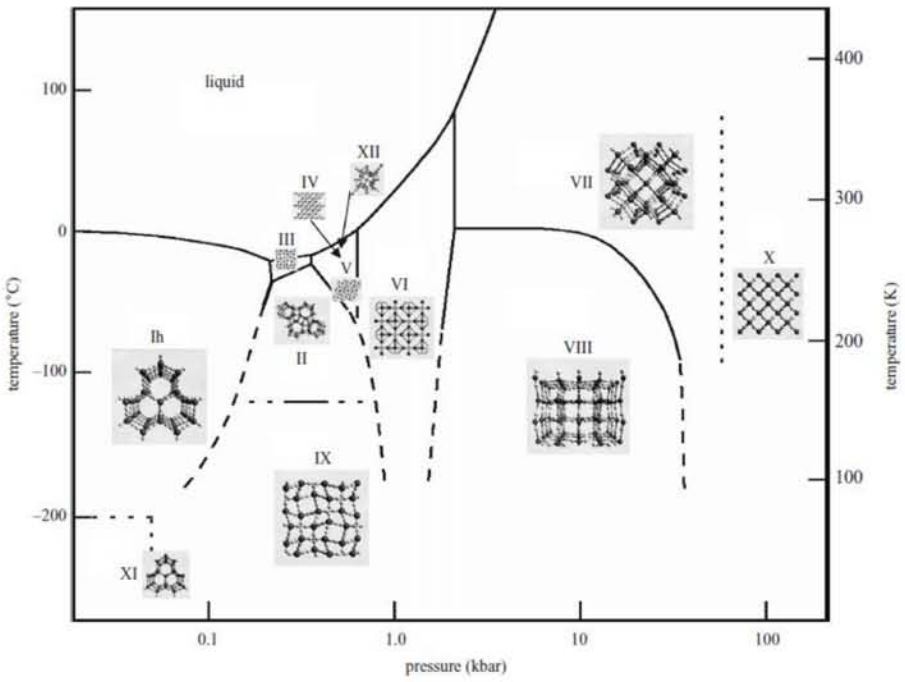

Figure 2.2. The phase diagram of ice. (from Ref. 32)

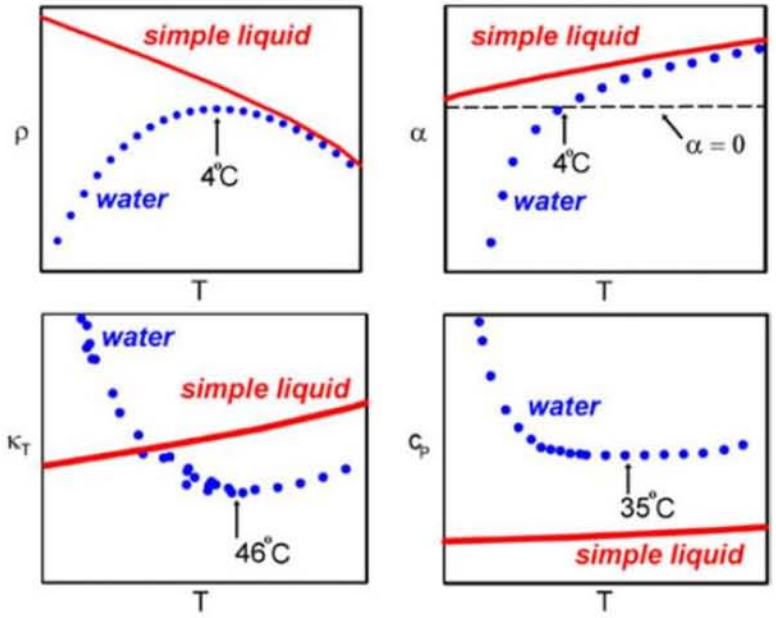

Figure 2.3. The temperature dependence of the density ρ, thermal expansion coefficient α, isothermal compressibility K_T, and isobaric heat capacity c_p for water. Those for a simple liquid are also shown for comparison. (from Ref. 1)

2.1.3. Supercooled and Glassy Water

Water can be supercooled below its freezing point without crystallization. This metastable liquid state is retained down to about 235 K under atmospheric pressure, at which the crystallization occurs spontaneously.[1-3, 8] This temperature is often referred to as a 'homogeneous nucleation temperature (T_H)'. T_H in the T-P plane is shown in **Fig. 2.4**. Interestingly, T_H and melting temperature (T_M) shows similar trend in the pressure dependence.[1]

When supercooled, the anomalous properties of liquid water are more pronounced.[1-3, 8] For instance, thermodynamic response functions and characteristic relaxation times (e.g. rotational correlation time) appear to diverge at a singularity temperature (T_S), when extrapolated slightly beyond T_H. T_S is estimated to be ~228 K at atmospheric pressure, applying a power-law fit to the measured data. The origin of this behavior has not been fully understood so far. It is therefore seen as a key to solve overall mysteries of water.

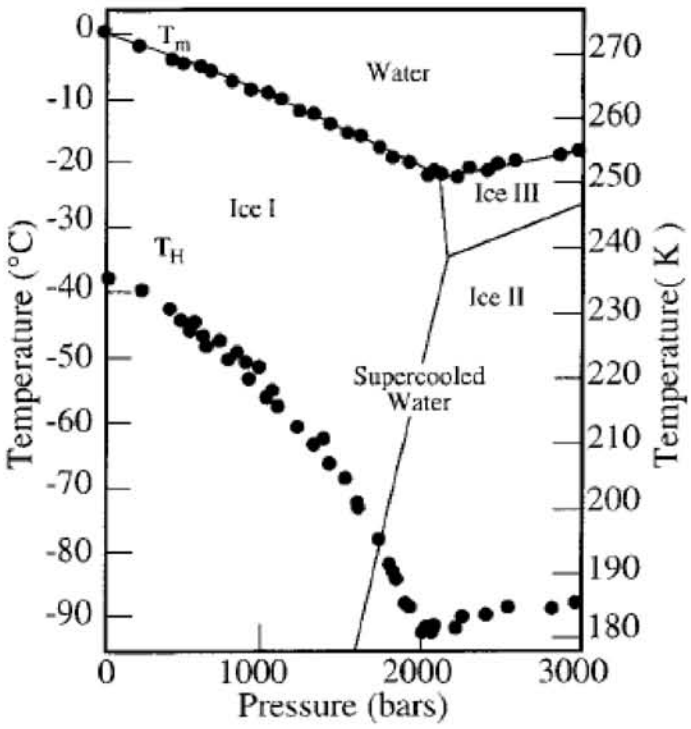

Figure 2.4. Homogenous nucleation temperature, T_H, as a function of pressure. T_M is the melting temperature. (from Ref. 1)

2.1.4. Polyamorphism in Water

When liquid water is cooled fast enough, the crystallization is avoided and it becomes amorphous solids.[8] Unlike most other liquids, water has at least two amorphous phases. This phenomenon is called polyamorphism.[8] The two phases are known as a low density amorphous ice (LDA) and a high density amorphous ice (HDA). LDA was originally produced by depositing water vapor onto a cold plate[33] or by cooling micrometer-sized droplets of liquid water extremely rapidly[34]. On the other hand, HDA was discovered by compressing ice Ih below 150 K.[35] Moreover, a polyamorphic transition between LDA and HDA is also possible. Since the change in properties of the amorphous ices is apparently discontinuous at the transition, it is considered to be a first-order phase transition.[8, 36, 37]

It has been reported that the glass transition temperature (T_g) of LDA is ~136 K.[8, 38] However, recent argument suggests that it should be around 165 K or higher.[17, 18, 39, 40]

Neutron diffraction studies showed that the structures of these amorphous ices are clearly different.[41] With integrating observed oxygen-oxygen (O-O) radial distribution functions between 2.3 and 3.3 Å, it was found that LDA has 3.9 nearest neighbors while HDA has higher value of 5.0.[41] This indicates that an additional water molecule is present in the first neighbor shell of HDA compared with that of LDA. As shown in **Fig. 2.5**, there are local order similarities between LDA and ice Ih, and HDA and liquid water, respectively.

When the LDA are heated, it crystallizes spontaneously to ice Ic at T_X of

about 150 K at atmospheric pressure.[1] Thus water in liquid state cannot be observed between T_H and T_X. This region is sometimes referred to as 'no man's land' in the T-P plane.[1-3, 8] **Figure 2.6** illustrates the 'no man's land' region at atmospheric pressure. It is expected that supercooled water and amorphous ices are inseparably connected. However its experimental observations are hampered by the 'no man's land' region.

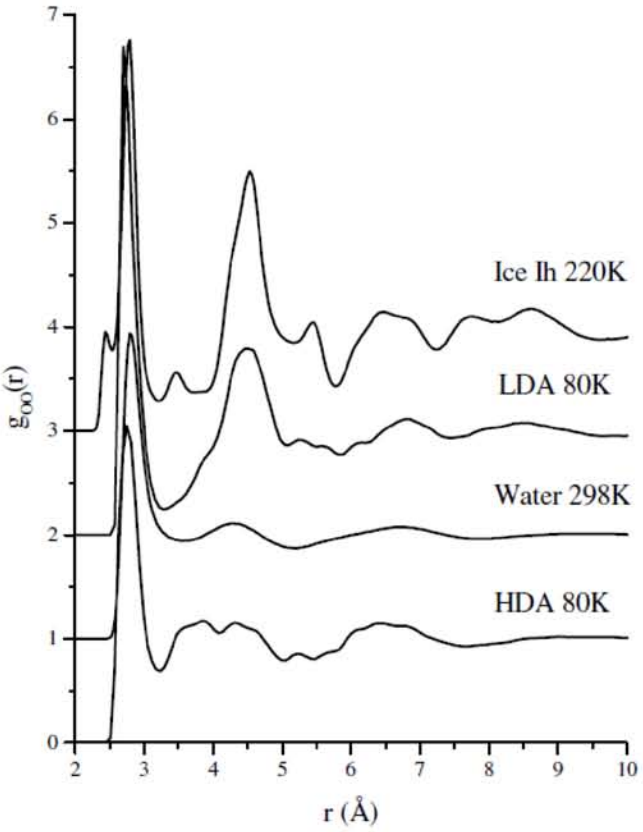

Figure 2.5. Oxygen-oxygen partial radial distribution function obtained by neutron diffraction experiments. (from Ref. 41)

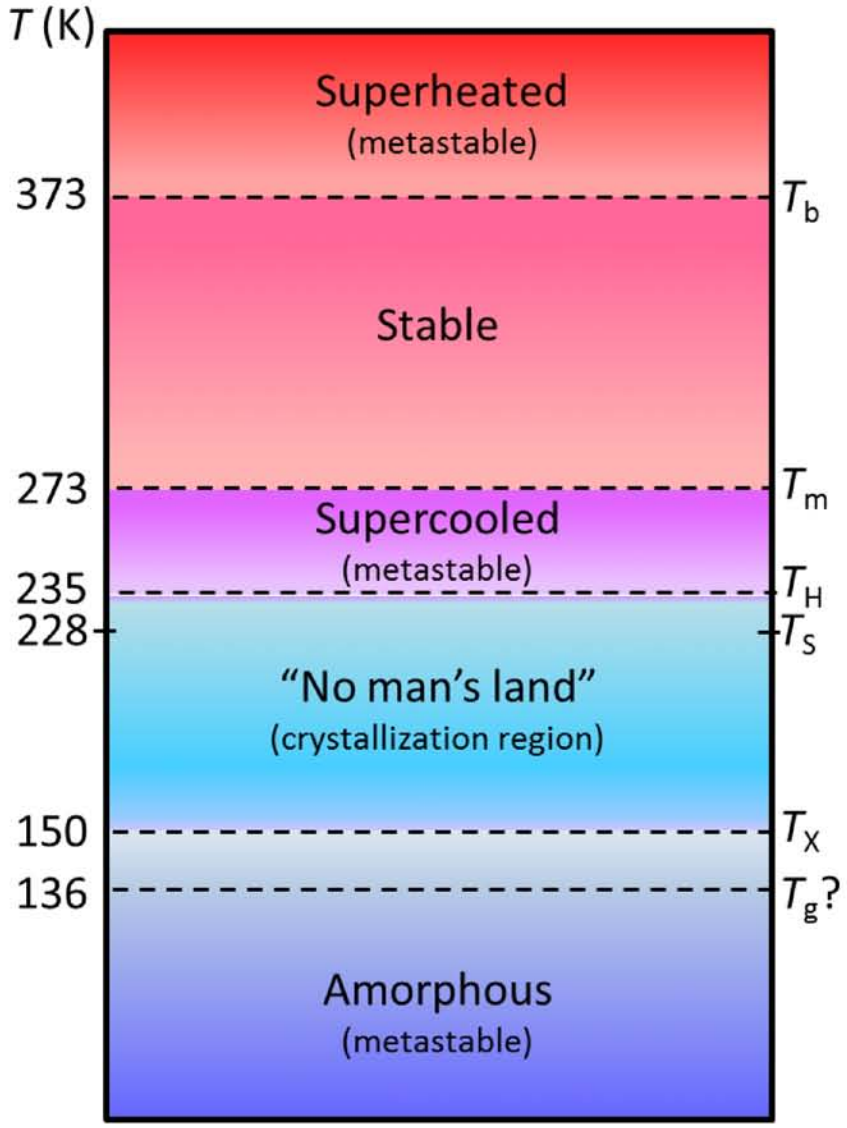

Figure 2.6. Temperature domains of stability and metastability for liquid and amorphous water at atmospheric pressure (adapted from ref. 1 and ref. 8). T_b denotes the boiling temperature, and T_m the melting temperature. T_S is obtained by applying a power-law fit to the measured thermodynamic response functions. T_H and T_X are a homogeneous nucleation temperature and a crystallization temperature, respectively.

2.1.5. Proposed Scenarios

Many hypotheses have been developed to solve the mysteries of water. Here four scenarios under active discussion are briefly described:

(I) The stability limit (SL) scenario

A T-P phase diagram of water illustrating the SL scenario is shown in **Fig. 2.7 (a)**. In the figure, liquid-gas (L-G) coexistence curve, also referred to as L-G binodal curve, and L-G spinodal curve are seen. Here, a coexistence curve denotes the condition at which two distinct phases, liquid and gas in this case, may coexist. At the same time, it is the boundary between a set of phases to be separated with thermodynamically favorable condition. On the other hand, a spinodal curve is the limit of stability for a set of phases. In the present case, it shows the boundary of absolute instability for the liquid phase against the gas phase.

In the SL scenario, it is hypothesized that the L-G spinodal curve at negative pressure retraces towards the positive pressure region when it intersects the locus of density maxima (also referred to as the temperature of maximum density, TMD).[1, 8, 10, 42] This is due to thermodynamic consistency: the slope of the spinodal curve in the T-P plane must change the sign when meeting a line along which the thermal expansion coefficient is zero.[1, 8, 10, 42] Because the spinodal is a locus of diverging density and entropy fluctuations, K_T and c_p increase and α decreases when they approach to the spinodal.[1-3]

Meanwhile, since a spinodal curve and a binodal curve can coincide only at a critical point, the intersection of the retracing spinodal with the

L-G coexistence (binodal) curve must be a critical point. However, the presence of such a critical point is not confirmed so far. This fact poses a serious challenge to the SL scenario.

(II) The liquid-liquid critical point (LLCP) scenario

The proposed phase diagram of water for LLCP scenario is illustrated in **Fig. 2.7 (b)**. It hypothesizes the existence of a first order transition line in supercooled region which separates two liquids with different structures, namely, high density liquid (HDL) and low density liquid (LDL).[1, 5, 6, 8, 10] HDL is a dense liquid with a highly disordered structure, while LDL has a lower density and locally tetrahedral order. In this scenario, the experimentally observed HDA and LDA are considered to be structurally arrested states of HDL and LDL, respectively.[1, 5, 6, 8, 10] According to these views, the transition between the two forms of liquid water would terminate at a liquid-liquid critical point, C' [**Fig. 2.7 (b)**]. Starting from C', the locus of maxima of the correlation length ξ , called the Widom line, emanates. Water above C' is a fluctuating mixture of LDL and HDL. This enhanced fluctuation influences the properties of liquid water, leading to the observed increase in the response functions (response of density or entropy to changes in temperature or pressure)[1, 5, 6, 8, 10] Until now, many computer simulations with various potentials for water confirmed the existence of a liquid-liquid transition terminating at C'.[44-46]

(III) The singularity-free (SF) scenario

The singularity-free (SF) scenario hypothesizes that the response

functions have a rapid rise, but there is no singularity. [1, 7, 8, 10] As discussed in Section 2.3., volume and entropy fluctuations in water become more pronounced as the temperature lowers, and they are anti-correlated below 277 K. In the SF scenario, it is assumed that this low-T anti-correlation causes the response functions to increase upon cooling. From this point of view, the transition between the two liquids is always continuous and the observed polyamorphic changes in water are essentially relaxation phenomena. [see **Fig. 2.7 (c)**].

At the same time, the increases in water's response function on supercooling can also be discussed based on a general thermodynamic theorem. Since the slope of the TMD, $(\partial P/\partial T)_{TMD}$, is negative in water, K_T must increase upon cooling, whether there is a singularity or not. The relevant thermodynamic relations are shown in ref 1.

Furthermore, both the LLCP and the SF scenarioes predict that the locus of density maxima changes slope in the negative pressure region in the P-T plane to avoid intersecting with the L-G spinodal curve [see **Fig. 2.7 (b)** and **(c)**].[7, 44, 47] This has been observed in simulations of liquid water.[1, 10, 44]

(IV) The critical-point free (CPF) scenario

It hypothesizes an order-disorder transition.[9, 10, 48] This is possibly a weakly first-order transition and separates two liquid phases (HDL and LDL). As shown in **Fig. 2.7(d)**, the spinodal of the transition between HDL and LDL extends to negative pressure region down to the L-G spinodal curve. The HDL-LDL spinodal is allowed to cross the L-G coexistence curve, in

contrast to the retraced L-G spinodal curve in the SL scenario. Thus, no critical point is present in this scenario.[9, 10]

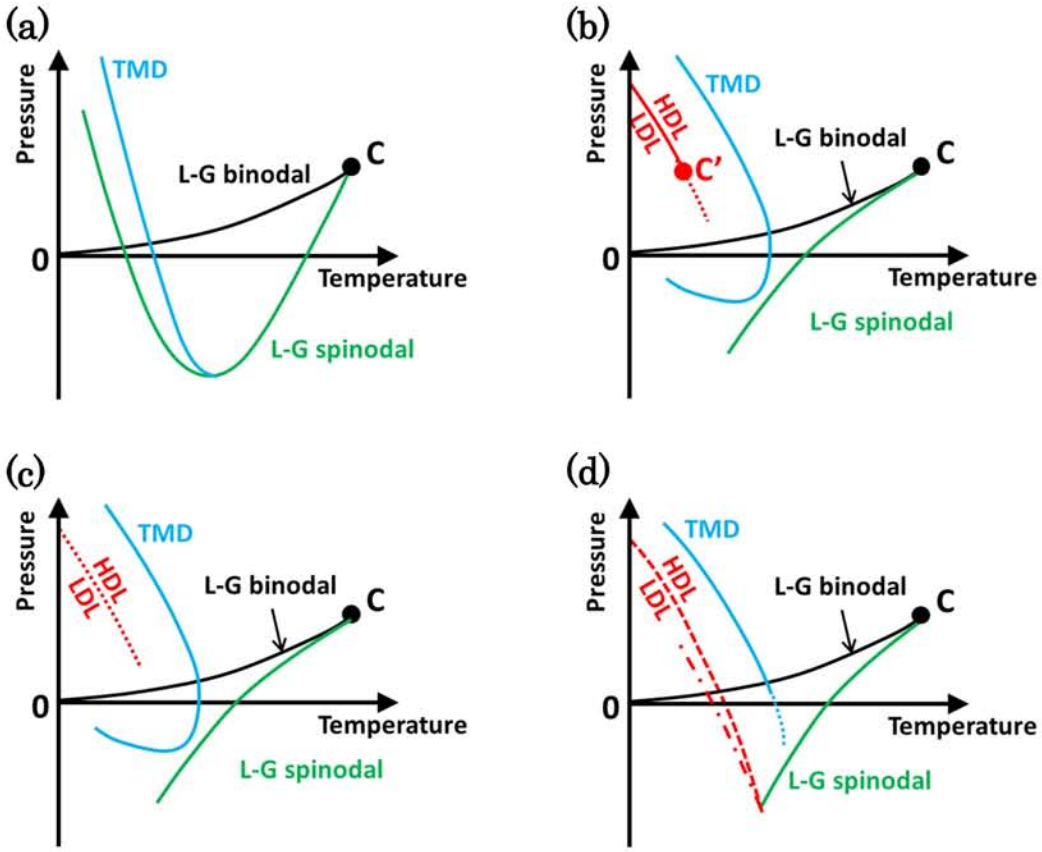

Figure 2.7. Different phase diagrams of water: (a) stability limit (SL), (b) liquid-liquid critical point (LLCP), (c) singularity free (SF), and (d) critical point free (CPF) scenarios. In (b) and (c), the dotted line is the Widom line. In (d), the dashed and dot-dashed lines are the HDL-LDL coexistence line and HDL-LDL spinodal, respectively. C is the 'normal' liquid-gas critical point, while C' in (b) is the hypothesized liquid-liquid critical point. (adapted from ref. 1 and ref. 10)

2.2. Water in Confined Geometries

Water in restricted spaces shows unusual properties that are not observed in the bulk.[25-31, 49-57] It is obvious that studies of confined water can contribute to not only the progressive studies of natural sciences[58-66] but also the development of new nano-devices under aqueous environments.[27, 28, 67-70]

Moreover, it is known that nano-confinement on water stabilizes the 'supercooled state' or liquid state even below the freezing temperature of bulk water.[11-17, 25-31, 52-57]

2.2.1. Confined Water in Nature

(I) Needle ice

One of the most familiar natural phenomena involving confined water should be needle ices (**Fig. 2.8**).[71] It occurs when the temperature of the soil is above 0 °C and the surface air temperature is below 0 °C. The ground water is brought to the surface by capillary action, where it freezes and contributes to the growth of needle-like ice column. Not all types of soil are suitable for the formation of needle ices. The soil must be sufficiently porous to allow capillary action. For instance, it is known that Kanto loam, which covers hills and plateaus in the Kanto region of Japan, consists of appropriate-sized soil grains for the needle ice formation. The needle ices form at the beginning of winter and lift or push away small soil particles above them.

Figure 2.8. Photograph of needle ices, taken in Kanagawa prefecture in Japan.

(II) Frost heave

Frost heave occurs under the proper conditions in the deep of winter.[64, 72] Frost heave is a lift of frozen solid layers by ice lenses [**Fig.2.9 (a)** and **(b)**]. An ice lens is a cluster of ice shaped like a lens due to a load of overlying soil. One or more growing ice lenses have enough power to lift a layer of soil, as much as 30 cm or more. The ice lenses grow even below 0 ℃, indicating that water in the soil is supercooled and there is a net flow of water to the ice lenses. It is considered that a thin layer of water exists between an ice lens and soil particles. The layer has an equilibrium thickness under given conditions. If the molecules from the supercooled water are added to the ice lens, the free energy of the system will be reduced. This available energy might do work to lift the soil layer and to pull the water up from the groundwater source. However, the mechanism remains to be completely elucidated. Ice lenses are formed not only in soil-water system but also in many porous media adsorbing liquid solution. Thus, the breakthrough is demanded by a variety of study fields such as biology, medical science, material engineering, food science, and space development.

Figure 2-9. Photograph of frost heave, taken in Mt. Takao in Japan. (a) A big ice lens underground. (b) Frost heave lifting the ground.

(III) Frost flower

With a similar process as the needle ice formation, 'frost flower' appears from a certain type of withered plants (**Fig.2.10**). In winter, the stem of the plant withers, while its roots survive underground. The living roots draw water from the soil to the stem. The drawn water comes out from cracks on the surface of the withered stem, and freezes upon contact with the air if the temperature is below 0 ℃. As more water is drawn through the cracks, it pushes the thin ice layers further from the stem, causing a thin 'petal' to form. An example of a plant which forms frost flowers is 'Shimo-bashira'. It is an endemic plant in Japan and found at the Kanto region and southward.

Figure 2.10. Photograph of a frost flower, taken in Mt. Takao in Japan.

2.2.2. Water in Porous Silica

Porous silica materials are made based on silicon dioxide, also known as silica. They have uniform pores with diameters more than 1 nm and huge surface area (normally ≥1000 m^2/g).[73, 74] One of the most common types of porous silica is MCM-41 or silica gel. MCM-41 consists of cylindrical-like uniform pores, arranged parallel in a two dimensional honeycomb-type lattice, while silica gel is composed of a three dimensional network of interconnected pores.

The phase behaviors of water confined in porous silica have been extensively studied for more than half a century, in order to elucidate the effects of confinement on water properties.[12-14, 16, 17, 52-56] For instance, pore diameter (D) dependence of the melting/freezing temperature $T_m(D)$ of the confined water has investigated using MCM-41 with a diameter more than ~2 nm.[52-55] It was found that the depression of the melting/freezing temperature, $\Delta T_m = 273 - T_m(D)$, can be represented by a modified Gibbs-Thomson (G-T) equation, $\Delta T_m = K/(D/2 - t)$, with K and t as parameters. t is regarded as thickness of the bound water on the pore wall and often estimated to be 0.3-0.4 nm. It has also been shown that the confined water crystallizes into ice Ic.[52, 53]

As for the properties of liquid water, it has been reported by calorimetric studies that isobaric specific heat (C_p) of water confined within MCM-41 and silica gel shows steep decrease accompanying a broad peak, and deviates significantly from that of the bulk liquid water at ~230 K.[17] Such the

anomaly in C_p has often been discussed related to the two liquid states and a liquid-liquid crossover (LLC) or fragile-strong crossover (FSC) predicted in the bulk water.[8] It was also observed that the glass transition of the confined water occurs between 115 K and 210 K, depending on the pore diameters.[17]

Furthermore, dynamic properties of the water confined in MCM-41 have been studied by quasi-elastic neutron scattering experiments (QENS).[13, 56] It has indicated the presence of a dynamic crossover (i.e. FSC) above T_g. This crossover converts water from a 'fragile' liquid above the transition to a 'strong' liquid below it, wherein fragile liquid shows non-Arrhenius T-dependence, while strong liquid shows Arrhenius T-dependence.[75, 76] The locus of LLC or FSC was often believed to be on the so-called Widom line. However, some of the details of these issues are rather speculative and have been questioned.[77-79]

2.2.3. Water in Carbon Nanotubes

Carbon nanotubes (CNTs) are cylindrical tubes consisting of a rolled-up graphene sheet.[21, 80-81] Their structures are specified by a pair of integers (n,m) referred to as the chiral indices. The integers n and m denote the number of primitive lattice vectors in graphene and assign how the graphene sheet is wrapped [see **Fig. 2.11(a)**]. CNTs are classified into two categories: single-walled carbon nanotubes (SWCNTs) and multi-walled carbon nanotubes (MWCNTs). A schematic illustration of an SWCNT is shown in **Fig. 2.11(b)**.

SWCNTs consist of a single sheet of graphene[21], while MWCNTs have

multiple rolled layers of graphene[80-81]. When fabricated, tens or hundreds of SWCNTs aggregate into bundles, forming a two dimensional hexagonal lattice, as shown in **Fig.2.11(c)**.

Although CNTs are made of hydrophobic graphene sheets, experimental studies, including X-ray scattering,[81, 25] neutron scattering,[83] nuclear magnetic resonance,[84-88] and optical measurements[89-90] have revealed that water can be confined in open-ended CNTs, as well as theoretical/computational calculations.[89, 91, 92] Direct observation of water filling has been carried out in MWCNTs using transmission electron microscopy (TEM).[93, 94] Other theoretical studies have been used to clarify water structures including hydrogen bonding inside SWCNTs.[95, 96] It was also reported that fluid transport rates through CNTs are exceptionally rapid,[94, 97-101] and rapid proton transport through a single file of oriented water was also suggested by computational simulations.[102] Since nano-scale hydrophobic channels are similar to biological channels, SWCNTs have the potential to be used for various biological applications.[59, 103] From a technological perspective, water-CNT systems could have novel applications such as nano-filtration,[67, 104-107] molecular nano-valves,[27, 108] molecular water pumps,[109] nano-scale power cells,[110-112] and even nano-scale ferroelectric devices.[28, 68] Thus, water-CNT is a system of great interest. However, phase behavior of water confined in CNTs is not well understood. Therefore, in this work, the global phase of water confined in SWCNTs has been systematically investigated.

Theoretical studies predict that water confined in SWCNTs with small

diameters undergoes a liquid-solid-like transition below room temperature and forms ordered tubular ice structures, the so-called ice nanotubes (ice NTs).[29-31] Detailed energetics of ice nanotubes have been previously discussed.[113, 114] The formation of helical ice-sheets was also predicted in the physiological condition.[115] In previous XRD studies, we experimentally proved the formation of ice NTs inside SWCNTs with diameters between 1.17 and 1.44 nm[26-28] and found that the melting/freezing temperature of ice NTs increased with decreasing SWCNT diameter, D.[26] This diameter dependence is opposite to that of water in larger diameter pores (> about 2 nm), where the melting/freezing temperature depression from that of bulk water is inversely proportional to the capillary diameter,[52-55, 116-120] following the modified G-T equation. Such anomalous behaviors of water-SWCNT systems have been reproduced by recent computational studies.[121, 122]

These reports on SWCNTs were made with smaller-diameter SWCNTs (D < ~1.4 nm), and very recently, studies with thicker SWCNTs have also been carried out. Computational studies have predicted the existence of more complex structures for nano-ice encapsulated inside thicker SWCNTs.[122, 123] For SWCNTs with diameters of about 1.4 nm, ice NTs encapsulating a one-dimensional (1D) water chain[83] were revealed by a combination of molecular dynamics (MD) calculations and neutron scattering experiments. In addition to the filled structures with a 1D water chain, other types of nano-ice morphologies, such as multilayer ice NTs and multilayer ice helixes, were also demonstrated by MD calculations using SWCNTs with diameters between 1.35 and 1.9 nm.[122, 123] Dynamic properties of water inside thick

CNTs have been studied by neutron scattering experiments.[15] Using double-walled carbon nanotubes (DWCNTs) having an inner CNT with a diameter of 1.6 nm, a fragile-strong transition (or crossover) was observed around 190 K. In addition, the response of dynamic relaxation time to applied pressure was measured using SWCNTs with a diameter of 1.6 nm.[124] It was suggested that free water molecules diffusing within the SWCNT matrix remarkably slow down with increasing pressure between 260 K and 220 K.

As seen above, experimental reports on water within thick CNTs are still few. Systematic studies with SWCNTs of various diameters are thus interesting to clarify the structure, dynamics and phase behavior linking to those in the bulk region.

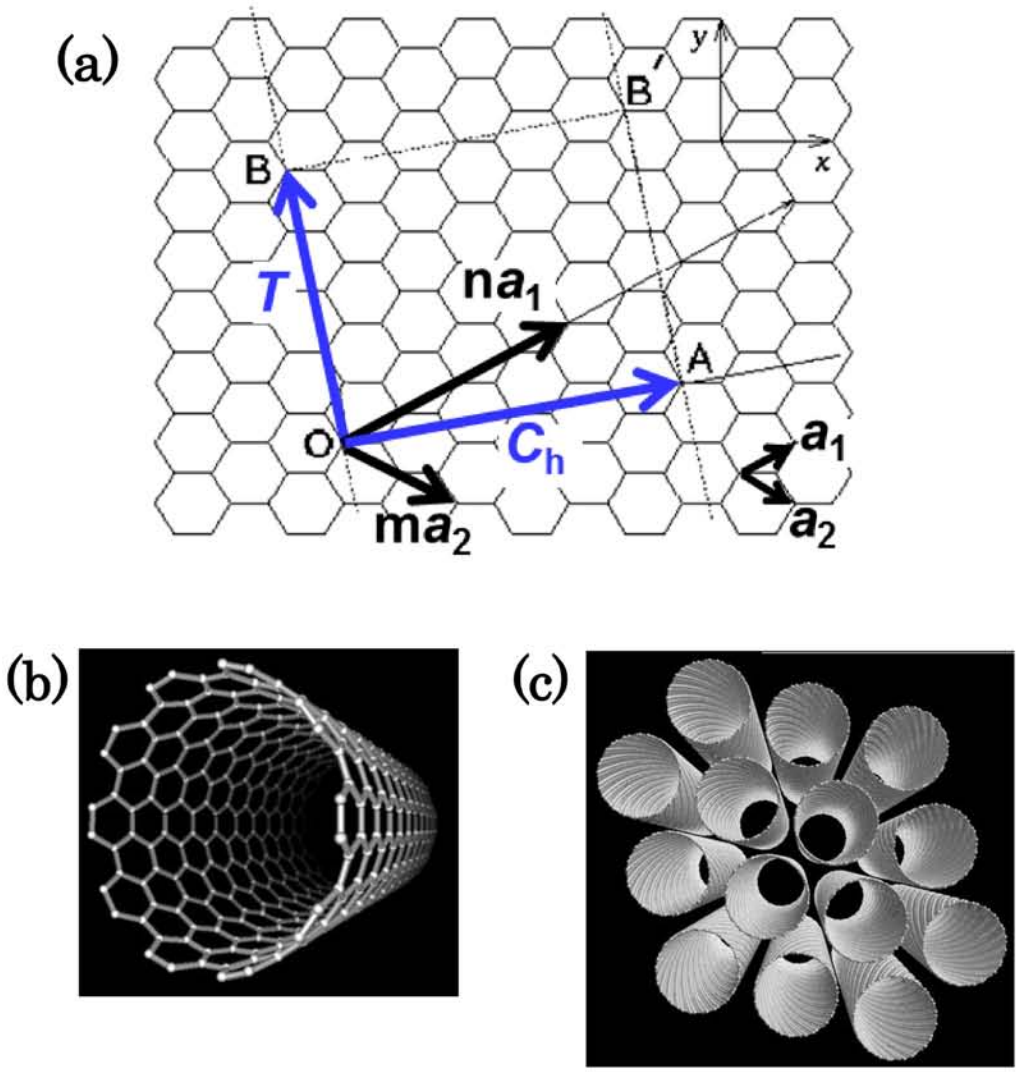

Figure 2.11. Schematic illustration of (a) a graphene sheet, (b) a single-walled carbon nanotube (SWCNT), and (c) a bundle structure of SWCNTs. In (a), a_1 and a_2 are the unit vectors for the hexagonal lattice of graphene. Chiral vector, C_h=na_1 + ma_2, describes how to roll up the graphene sheet to construct an SWCNT; cut the sheet along the line OB and AB', and then roll up it joining the side OB and AB'. The length of C_h is equivalent to the circumference of the SWCNT. T denotes the unit lattice vector along the tube axis direction.

Chapter 3

Experimental Methods

3.1. Sample Preparation

3.1.1. Single-walled Carbon Nanotubes (SWCNTs)

Six SWCNT samples were prepared for the XRD, NMR, and electrical resistance measurements. For an SWCNT sample with a mean diameter of 1.46 nm, raw soot was obtained by the arc discharge method and purified using density gradient ultracentrifugation purification techniques.[125] The other five SWCNT samples with larger diameters were synthesized by the enhanced direct-injection pyrolytic synthesis (e-DIPS) method.[126, 127] An example of the as-grown SWCNT mat synthesized by the e-DIPS method can be seen in **Fig. 3.1(c)**. Because the as-grown samples cannot allow introduction of water molecules inside the SWCNTs, they were heat-treated in air to open the SWCNT walls.[27] These samples were characterized by optical absorption and XRD measurements.

Figure 3.1(a) shows the observed XRD profiles of the dry samples sealed inside the XRD quartz capillaries after being degassed. We can see the well developed distinct Bragg peaks, indicating that the samples are highly pure and the SWCNTs are well bundled. As reported previously, the observed peaks were indexed according to the 2D hexagonal lattice of SWCNTs, as shown in **Fig. 3.1(b)**.[27, 82,25, 26, 128, 129] In **Fig. 3.1(a)** it is clearly seen that the Bragg peak position moves depending on the sample. This reflects the variation of the mean SWCNT diameter. With detailed analyses of the

profiles, as described later, it was found that the sample prepared by the arc discharge method had a mean diameter of 1.46 nm, as indicated above, with a distribution of about ±0.12 nm. The samples prepared by the e-DIPS method were found to have mean diameters of 1.68, 1.94, 2.00, 2.18, and 2.40 nm, with a distribution of about ±0.25 nm. (Here, the diameter distribution means that of the averaged diameter within a bundle.) The SWCNT diameter is defined as the diameter of a cylinder covering the carbon nuclei.

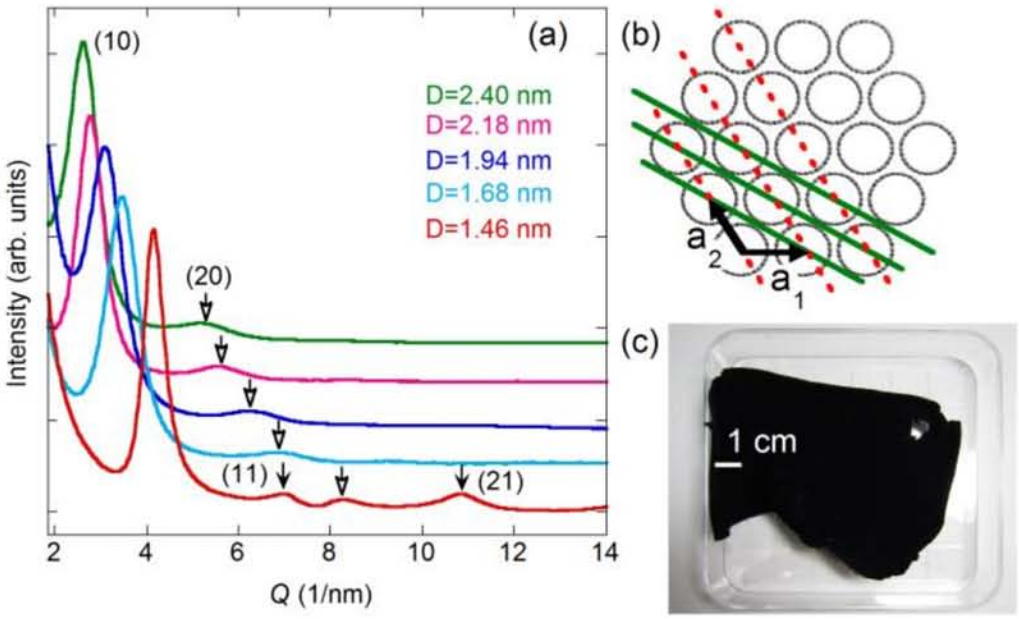

Fig. 3.1. (a) XRD profiles of dry SWCNT samples with mean diameters of 1.46, 1.68, 1.94, 2.18, and 2.40 nm from the bottom to the top, respectively. The profiles were artificially shifted vertically for convenience of viewing. The arrows indicate Bragg peaks indexed to (10), (11), (20), and (21). (b) Schematic illustration of a cross section of SWCNT bundle. The 2D hexagonal lattice of the bundle indexes the Bragg peaks well. The dashed lines in red defines the (10) plane, and the solid green lines define the (11) plane. (c) Photograph of an as-grown SWCNT mat obtained by the e-DIPS method.

3.1.2. Zeolite-templated Carbon (ZTC)

A synthesis procedure of the zeolite-templated carbon (ZTC) is described briefly as follows. First, carbon is introduced into the nanochannels of zeolite Y. Then the resulting zeolite/carbon composite is washed with an aqueous HF solution to remove the zeolite. Finally, ZTC is obtained as a residue. A proposed model for ZTC is buckybowl-like nanographenes assembled into a three-dimensional regular network.[24] **Fig. 3.2** illustrates a proposed model structure of a ZTC crystal and its ideal composite. The ideal composite is $C_{36}H_9$ with a small content of oxygen contaminant (~5 at%).[24] Remarkable characteristics of ZTC are its uniform nanopores with a diameter of ~1.2 nm and its high specific surface area of up to 4000 m^2/g.

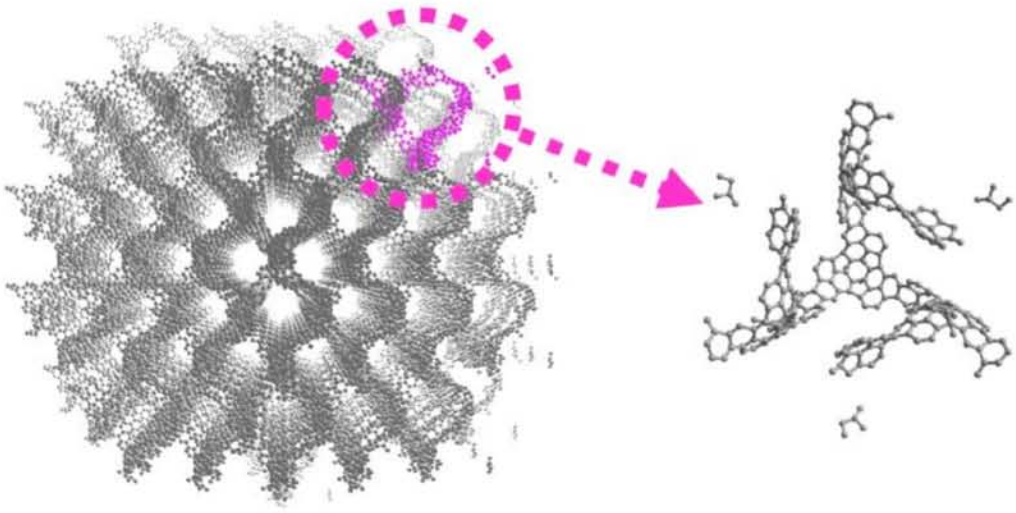

Fig. 3.2. Ideal structural model proposed for ZTC. Left: viewed from the [110] direction. Right: unit cell containing eight $C_{36}H_9$ units. Hydrogen atoms are omitted from the figure for simplification.

3.2. Powder X-ray Diffraction (XRD) Study

3.2.1. XRD Experiments

Powder XRD measurements were carried out using synchrotron radiation with a wavelength of 0.100 nm at the BL1B and BL8B stations in the Photon Factory (PF) facility, KEK, Japan. The diffracted X-rays were recorded as a two-dimensional (2D) image data with an imaging plate (IP). The 2D image data is integrated along the direction of scattering angle, 2θ, with a width of 100 pixels to obtain one-dimensional (1D) data. The resolution for the scattering angle of the diffracted X-rays was 0.03 degrees, and camera length of the IP is 191.28 mm. The amplitude of the X-ray scattering wave vector is defined by $Q = 4\pi\sin\theta/\lambda$.

The SWCNT samples were sealed in thin XRD quartz capillaries with a typical diameter of 0.5 mm or 0.7 mm, after being thoroughly degassed by heating above 770 K in a dynamic vacuum. For the wet samples, the heat treated SWCNT samples in air were sealed with saturated water (H_2O) vapor of ultrahigh purity at room temperature (RT).

On the other hand, the dry ZTC powder was sealed inside a XRD quartz capillary with a diameter of 0.7 mm after it was well pumped. In the wet sample, the ZTC sample was sealed with saturated water vapor at RT.

In these measurements, the sample temperature was controlled by a gas-blow type cryostat from Rigaku in a temperature (T)-range of 100-350 K, holding the other empty side of the XRD capillaries at RT. Therefore, the measurements with the wet samples below RT were performed under a saturated vapor condition at the measurement temperature.

3.2.2. XRD Simulations with a Homogeneous Charged Hollow Cylinder Model

Simulations of XRD patterns for SWCNT bundles were performed using a homogeneous charge-distribution model for the SWCNTs, in which the SWCNTs are modeled as hollow cylinders of uniform electron density, forming bundles of a close packed hexagonal lattice.[128, 129] Analyses of the XRD patterns are briefly described below.

The diffracted intensity $I(\vec{Q})$ for the scattering vector $\vec{Q}$ is given by the electron density $\rho_i(\vec{r})$ in the sample:

$$I(Q) \propto \sum_i \left| \int_{V_i} \rho_i(\vec{r}) \exp(i\vec{Q}\cdot\vec{r}) dV_i \right|^2 = \sum_i |F_i|^2 \left| \sum_{l_i} \exp(i\vec{Q}\cdot\vec{r}_{l,i}) \right|^2 \approx \sum_i |F_i|^2 \sum_{G(i)} \left(P_{G(i)} N_{G(i)} \right), \quad (3\text{-}1)$$

where the summation is done over all the i^{th} SWCNT bundles with volume V_i in the sample. The sum of l_i is taken over all the lattice points $\vec{r}_{l,i}$ in the i^{th} bundle and give the usual Laue condition in the case of a large crystal. The Laue function is approximated to a peak function $P_{G(i)}(Q)$ which has its maximum value at the reciprocal lattice points G. $N_{G(i)}$ is the number of equivalent diffractions. F_i is the form factor of an SWCNT and is written as:

$$F_i = \int \rho(\vec{r}') \exp(i\vec{Q}\cdot\vec{r}') dV , \quad (3\text{-}2)$$

where $\vec{r}'$ is a position vector from the axial symmetry axis of the SWCNT. In addition, the diameter distribution of the SWCNTs, assumed to be a Gaussian distribution, is included in the calculations. The background

diffraction intensity is assumed in the form of $\exp(-Q^2/b)$ with a parameter b.

When the SWCNTs encapsulate molecules, F_i is rewritten as:

$$F_i = \int \{\rho_{\text{tube}}(\vec{r}') + \rho(\vec{r}')\} \exp(i\vec{Q}\cdot\vec{r}')dV \,, \tag{3-3}$$

where $\rho_{\text{tube}}(\vec{r}')$ and $\rho(\vec{r}')$ are the electron densities averaged in the i th bundle for SWCNTs and the adsorbed molecules inside SWCNTs, respectively. In the present studies, the water density profile function $\rho(\vec{r}')$ inside the SWCNTs was calculated from the molecular coordinates obtained from the corresponding MD calculations.

3.2.3. XRD Simulations with SWCNT Models

In homogeneous charged cylinder model described in 3.2.2, because the atomic arrangements are smeared out, their information is lost. Besides, the model cannot be applied to the small bundles. Thus, using the Forcite tool in Materials Studio 6.0 (Accelrys Software, Inc.), the calculations of XRD patterns were also performed based on the Debye formula:

$$I(Q) = \sum\sum f_m f_n \frac{\sin(Qr_{mn})}{Qr_{mn}} \tag{3-4}$$

Here, Q is the amplitude of the scattering vector and is given by $Q = 4\pi\sin\theta/\lambda$ for a scattering angle 2θ and an X-ray wavelength of λ. $I(Q)$ is the diffraction intensity at Q, f_n is the scattering amplitude from the n-th atom, and r_{mn} is the distance between the n-th and m-th atoms. For the

simulations, a bundle of nine SWCNTs with diameters ranging from 2.0 to 2.8 nm was modeled, where the diameter distribution of the SWCNTs in the bundle was set referring to that obtained by the previous simulations. XRD patterns were calculated with varying water contents inside the SWCNTs. Here MD simulations of the systems were performed to obtain water structures at each temperature for the XRD calculations.

3.3. Nuclear Magnetic Resonance (NMR) Measurements

^{2}D (deuteron) and ^{1}H (proton) -NMR experiments on heavy and light water-SWCNT systems were conducted using a pulsed Fourier transform NMR technique, at a constant field of 4.012 T in the temperature range of 100 - 350 K. The resonance frequencies for the Larmor precession of ^{2}D and ^{1}H nuclei in the field of 4.012 T are 26.22 MHz and 170.8 MHz, respectively. For the NMR measurements, the entire sample tube containing SWCNTs or ZTC was controlled to be almost uniform temperature.

The NMR spectra were obtained by Fourier transformation of free induction decay (FID) following radio frequency (rf) pulses. A typical width of $\pi/2$ pulse is 8-10 μs in ^{2}D-NMR and 4-6 μs in ^{1}H-NMR for wet-SWCNTs, while 8-10 μs in ^{2}D-NMR and 2-6 μs in ^{1}H-NMR for wet-ZTC.

The spin-lattice relaxation time T_1 of the ^{2}D-NMR was measured using a saturation recovery method or inversion recovery method. Assuming quadrupole interaction and isotropic rotation of water molecules, the T_1 was analyzed using the formula[130]

$$\frac{1}{T_1} = \frac{3}{40}\left(\frac{e^2 qQ}{\hbar}\right)^2\left(1+\frac{\eta^2}{3}\right)\left[\frac{\tau_{rot}}{1+(\omega\ \tau_{rot})^2}+\frac{4\tau_{rot}}{1+4(\omega\ \tau_{rot})^2}\right], \qquad (3\text{-}5)$$

where the quadrupole coupling constant of e^2qQ/h = 195 kHz and its asymmetric parameter of η = 0.1 were used for the heavy water molecule.[131] The NMR frequency was $\omega/2\pi$ = 26.22 MHz.

3.4. Electrical Resistance Measurements

For electrical resistance measurements, the SWCNT mats were formed into thin films with dimensions of 3×9 mm^2 after heat-treatment in air to open the SWCNT walls. Resistance measurements were performed in a four-terminal geometry with gold electrodes on the SWCNT film. The resistance was measured in a *T*-range of 120-473 K with a gas-flow type cryostat (JEOL). The SWCNT films were well dried in vacuum at 473 K and then exposed to saturated water vapor at RT. In some cases, environmental gases at a pressure of 0.1 MPa were introduced with water vapor.

3.5. Optical Microscopic Observations

SWCNT samples were sealed into XRD quartz capillaries with saturated water vapor at RT for optical microscopic observations. The procedure for sample preparation and water vapor introduction is the same as that in the XRD experiments. The capillary is 0.7 mm in diameter and ~20 mm in length.

The sample was attached on heating/cooling stage (Linkam, 10086L) with silicone grease to improve heat-transfer resistance. The temperature of

the stage was controlled between RT and 150 K by cooled N_2 gas. The sample chamber was held with vacuum during the observation, avoiding frost growth on the surface of the sample tube. Cooling/heating rate of the sample was 10 K/min. Photographs were taken every 5 seconds.

3.6. Calorimetric Measurements

Differential scanning calorimetry (DSC) measurements were carried out using a DSC 650 from Shimadzu Ltd. in the T-range of 130-330 K as a function of water content. Typical sample volume was about 4 mg, which was sealed inside an aluminum cell with ultrapure water. The isobaric specific heat (C_p) was determined from analysis of the DSC signal, when the temperature was controlled in a step-wise manner, to diminish the effect of T-variation of the isothermal baseline.[132] The contribution from the confined water in ZTC was obtained by subtracting the data taken for dry ZTC.

3.7. Classical Molecular Dynamics (MD) Simulations

Classical molecular dynamics (MD) calculations for water-filled SWCNTs were carried out using 'Materials Explorer 5.0' (Fujitsu Ltd.).

Water molecules were described by the TIP3P model[133] for the simulations in Chapter3 and by the SPC/E model[134] in Chapter4 and 5. Both TIP3P and SPC/E models treat the water molecule as a rigid body and have three interaction sites, namely, one oxygen atom and two hydrogen atoms. They are different in molecular geometry and parameters for Lennard-Jones (L.J.) potential and Coulomb interaction potential (see **Table 1**), causing

significant differences in calculated bulk properties for liquid water. For instance, it has been reported that the self-diffusion coefficient and O-O radial distribution function of SPC/E model gives better agreement with the experimental values for bulk liquid water than the TIP3P model.[135, 136] As far as the simulations for nano-confined water inside SWCNTs are concerned, previous works using these water models successfully reproduced observed structures and phase behaviors in water-SWCNT systems.[28, 121]

3.7.1. Model Systems

(I) Water-SWCNT systems

To prevent unreasonable translational motion of macroscopic water clusters at low temperature, some artificial atoms with small interaction parameters with the water molecules were located inside the SWCNT. The SWCNT and artificial atoms were fixed in a simulation cell.

(II) Water-ZTC systems

The water molecules were described by the SPC/E water model. We performed two types of simulations, I and II. In simulation I, a ZTC crystal consisting of 8 unit cells (4.814 nm × 4.814 nm × 4.814 nm) was fixed at the center of a larger simulation cell (10 nm × 10 nm × 10 nm) to investigate the water adsorption process. In simulation II, the cell size was the same as that of the ZTC crystal (4.814 nm × 4.814 nm × 4.814 nm), and water molecules were always confined inside the ZTC.

Simulation II was performed for 3112 water molecules, corresponding to the density of the water cluster obtained in simulation I.

3.7.2. Calculation Condition

The interaction potential, V_{WW}, among the water molecules is the sum of the L.J. potential, $V_{L.J.}$, between the oxygen atoms and the Coulomb interaction potential, $V_{Coulomb}$, of the charges between water molecules:

$$V_{WW} = \sum_{i \neq j} 4\varepsilon_{OO} \left\{ \left(\frac{\sigma_{OO}}{r_{ij}} \right)^{12} - \left(\frac{\sigma_{OO}}{r_{ij}} \right)^{6} \right\} + \sum_{l \neq m} \frac{1}{4\pi\varepsilon_0} \frac{q_l q_m}{r_{lm}} \qquad (3\text{-}6)$$

Here, r_{ij} is the oxygen (O) - oxygen (O) distance, ε_{OO} and σ_{OO} are L.J. parameters for the O-O interaction, r_{lm} is the distance between the point charges q_l and q_m in a different water molecules, and ε_0 is the dielectric constant of vacuum. The interaction potentials of water molecules with carbon atoms in an SWCNT or ZTC and with the artificial atoms are also given by the L.J. potential. The L.J. parameters for the present study are listed in **Table 2**. Here ε_{OC} and σ_{OC} were estimated from the Lorentz-Berthelot rule, $\varepsilon_{OC} = \sqrt{\varepsilon_{OO} \cdot \varepsilon_{CC}}$ and $\sigma_{OC} = (\sigma_{OO} + \sigma_{CC})/2$, using $\varepsilon_{CC} = 28\,\mathrm{K}$ and $\sigma_{CC} = 0.34\,\mathrm{nm}$. The cut-off length for both the L.J. potential and the Coulomb interaction potential was set to 2.0 nm.

The equation of motion was integrated using the Gear algorithm with a time step of 1.0 fs. In the calculations, the number of molecules (N), volume of the simulation cell (V), and temperature (T) of the system were conserved (NVT ensemble). The system temperature was controlled by the velocity-scaling method from 500 K to 100 K.

	TIP3P	SPC/E
ℓ_{OH} (nm)	0.09572	0.1
θ_{HOH} (°)	104.52	109.47
q_O (C)	-0.834e	-0.8476e
q_H (C)	0.417e	0.4238e
$\varepsilon_{O\text{-}O}/k_B$ (K)	76.6	78.5
$\sigma_{O\text{-}O}$ (nm)	0.315061	0.317

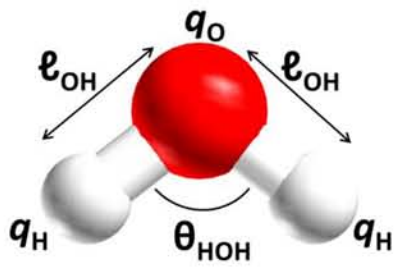

Table 1. Parameters of potential functions for TIP3P and SPC/E water models.[133, 134] The right figure shows the geometry of a water molecule. e and k_B denote the elementary charge and Boltzmann's constant, respectively. In ref. 134, the Lennard-Jones potential function for the SPC/E model is described as $V_{LJ} = -(A/r)^6+(B/r)^{12}$, where A=0.37122 $(kJ/mol)^{1/6}nm$ and B=0.3428 $(kJ/mol)^{1/12}nm$. In the present study, we converted this original function into the one shown in the right side first term of equation (3-6) for convenience in simulations.

	ε/k_B (K)	σ (nm)
TIP3P (O) - SWCNT (C)	46.3	0.327531
TIP3P (O) - artificial atom	5.3	0.245
SPC/E (O) - SWCNT(C)	46.9	0.329
SPC/E (O) - artificial atom	5.3	0.245

Table 2. Lenard-Jones potential parameters for the present study. Atomic species in the interaction are noted in brackets. k_B is Boltzmann's constant.

3.7.3. Analyses

The rotational correlation functions $C_\ell(t)=\langle P_\ell\{\cos\theta(t)\}P_\ell\{\cos\theta(0)\}\rangle$, where $P_\ell[\cos\theta(t)]$ denotes a Legendre polynomial of rank ℓ, were calculated for a water molecule from the MD results. Here, $C_2(t)$ can be obtained from NMR and light scattering[137], while $C_1(t)$ is obtained from dielectric spectroscopy. Therefore, the $C_2(t)$ was compared with the NMR results:

$$C_2(t)=\frac{1}{2}\left\langle 3\cos^2\theta(t)-1\right\rangle=\frac{1}{2}\left\langle 3\{\vec{u}_i(t)\cdot\vec{u}_i(0)\}^2-1\right\rangle, \tag{3-7}$$

where $\vec{u}_i(t)$ is a unit vector pointing toward a molecular axis, and $\theta(t)$ is an angle between $\vec{u}_i(t)$ and $\vec{u}_i(0)$. When the rotational correlation function decays non-exponentially with time, it is often described by the Kohlrausch expression;

$$C_\ell(t)\propto\exp\left[-(t/\tau_\ell)^{\beta_\ell}\right],\quad \beta_\ell\le 1. \tag{3-8}$$

In the present case, it was well reproduced using this expression with the fractional exponent, $\beta_\ell=0.5-0.6$. The self-diffusion coefficient D was also obtained by calculating the mean square displacement from the MD results. For these analyses, the system temperature in the MD simulation was controlled in a stepwise manner between 500 K and 100 K. The systems were kept in simulations at each temperature for more than 1 ns to achieve their equilibrium state.

Chapter 4
Global Phase Diagram of Water Confined inside SWCNTs

4.1. Results and Discussion
: Wet-dry Transition in SWCNTs with Diameter $D > 1.6$ nm

4.1.1. XRD of Water-SWCNTs

Figures 4.1(a)-(d) show typical XRD profiles of water-SWCNTs with diameters of 1.68, 1.94, 2.18, and 2.40 nm, respectively. In all of these profiles, the Bragg peaks indexed to (10) were clearly observed at Q = 2.5 - 3.5 nm^{-1}. As shown in **Fig. 4.1(b)**, the profile at 340 K coincided with that of the empty SWCNTs. This suggests that the SWCNTs do not adsorb water at higher temperatures. When the temperature was lowered to 300 K, the (10) peak intensity greatly diminished. It has been known that the (10) peak intensity is particularly sensitive to adsorption at the inner cavity of SWCNTs and the interstitial sites of the SWCNT bundle.[25-27, 82, 129] Here, the analyses, discussed later, indicate that the SWCNTs dominantly adsorbed water inside. When the temperature was lowered below a certain temperature T_{wd}, the XRD profiles substantially changed [**Figs. 4.1(a)-(d)**];

the (10) peak intensity from the SWCNT samples with $D > 1.6$ nm partially recovered below T_{wd}. (Here, T_{wd} is defined for the heating process, as will be shown in **Fig. 4.2**.) In these measurements, the average ramp speed of the T variation was fixed at about 1 K/min. As shown in the inset in **Fig. 4.1(a)**, the dry SWCNT sample exhibited little change in the XRD profile over the entire T range. Hence, the observed anomalous increases should be caused with water.

Figure 4.2 summarizes the T dependence of the (10) peak intensity from the SWCNT samples in water vapor. It is found that the "anomaly" in temperature dependence of the (10) peak intensity, mentioned above, systematically changes with increasing SWCNT diameter; T_{wd} and the (10) intensity much below T_{wd} increased according to the SWCNT diameter for the thicker SWCNT samples. On the other hand, the (10) intensity of the 1.35 nm SWCNT sample, as reported previously, was almost constant over the entire T range examined. An increase in the (10) intensity simply suggests a decrease in water content. A detailed discussion is given in later sections.

Further XRD measurements were performed to examine the effect of heat-treatment of the SWCNT samples on the observed low temperature anomaly. As mentioned in 3.1.1., the heat-treatment is usually performed to open the SWCNTs' walls. This enables the adsorption of water inside the SWCNTs. Five as-grown 1.68 nm SWCNT samples were heated in air for different times until their weights were reduced by 5, 10, 20, 50, and 80%, respectively. The T dependence of the (10) Bragg peak intensity for these

SWCNT samples in water vapor is shown in **Fig. 4.3(a)**. The (10) intensity from the samples with weight loss of 5 and 10% was substantially larger than those from the other well-heated samples. It is presumed that the SWCNTs in these two samples were not opened sufficiently. On the other hand, when the sample weight was reduced by more than 20%, the (10) intensity decreased substantially at around 300 K and exhibited the anomalous increases below T_{wd}. These behaviors did not depend on the heat-treatment time once the walls of the SWCNTs were opened enough to allow the introduction of water molecules. Similar experiments were conducted on the 2.40 nm SWCNT samples as well. In this case, the samples were heated for two different time periods at 600°C in air, 13 min and 38 min. The results are shown in **Fig. 4.3(b)**, along with those for an as-grown sample. Even for the as-grown sample, water was suggested to be encapsulated inside the SWCNTs at 300 K, probably due to the presence of opened defects, and there may be a trace of a slight increase in the (10) intensity below 240 K. The results suggest that the anomaly hardly depended on the degree of heat treatment in these samples.

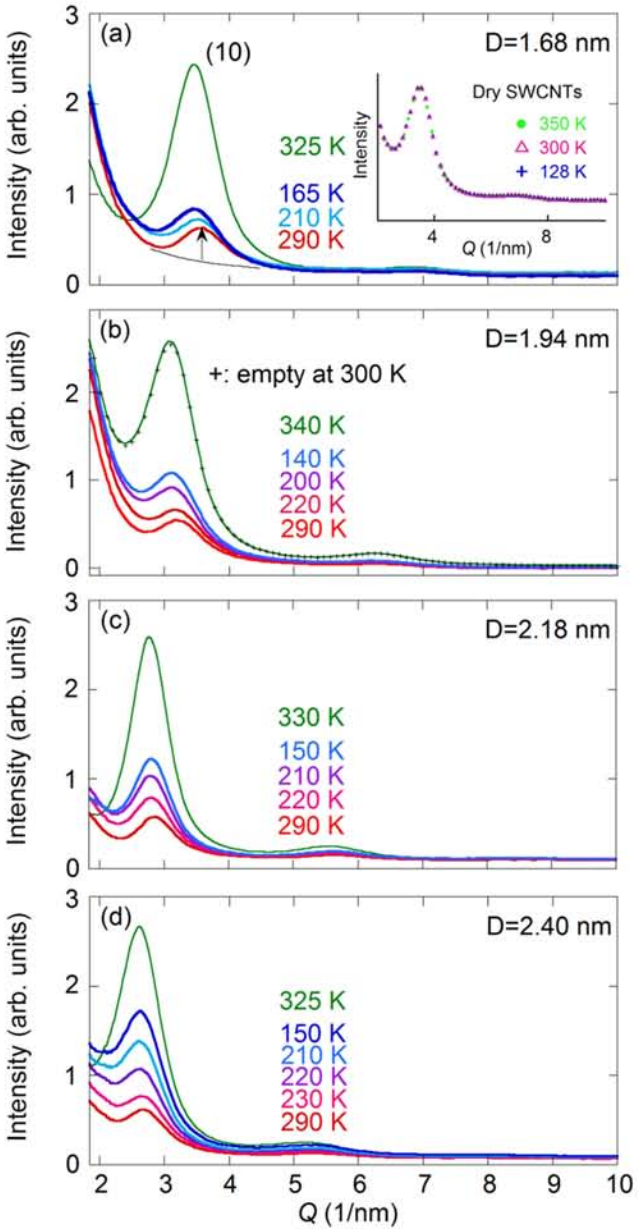

Fig. 4.1. XRD patterns of the water-SWCNT samples with different mean SWCNT diameters *D*. (a) $D = 1.68$ nm, (b) $D = 1.94$ nm, (c) $D = 2.18$ nm, and (d) $D = 2.40$ nm. The arrow defines the peak intensity. **+** indicates the data for the dry 1.94 nm SWCNT sample before water adsorption. The inset in (a) shows the XRD patterns of the dry-SWCNT sample with $D = 1.68$ nm.

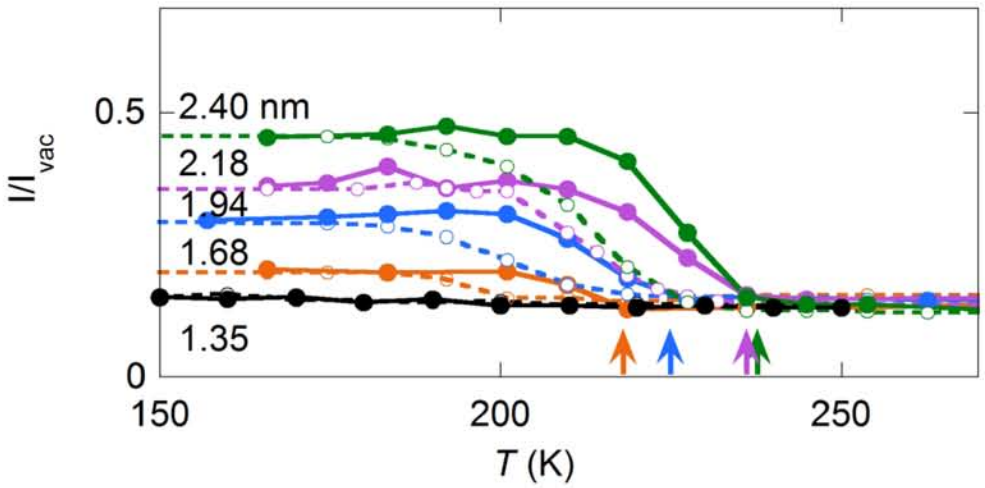

Fig. 4.2. *T* dependence of the (10) Bragg peak intensity in 2.40, 2.18, 1.94, 1.68, and 1.35 nm SWCNT samples filled with water at 300 K. The intensity was normalized by those of the empty SWCNT samples. The data for the 1.35 nm SWCNT sample were multiplied by 0.6 for comparison. Open circles with dashed lines and filled circles with solid lines indicate the cooling and heating process, respectively.

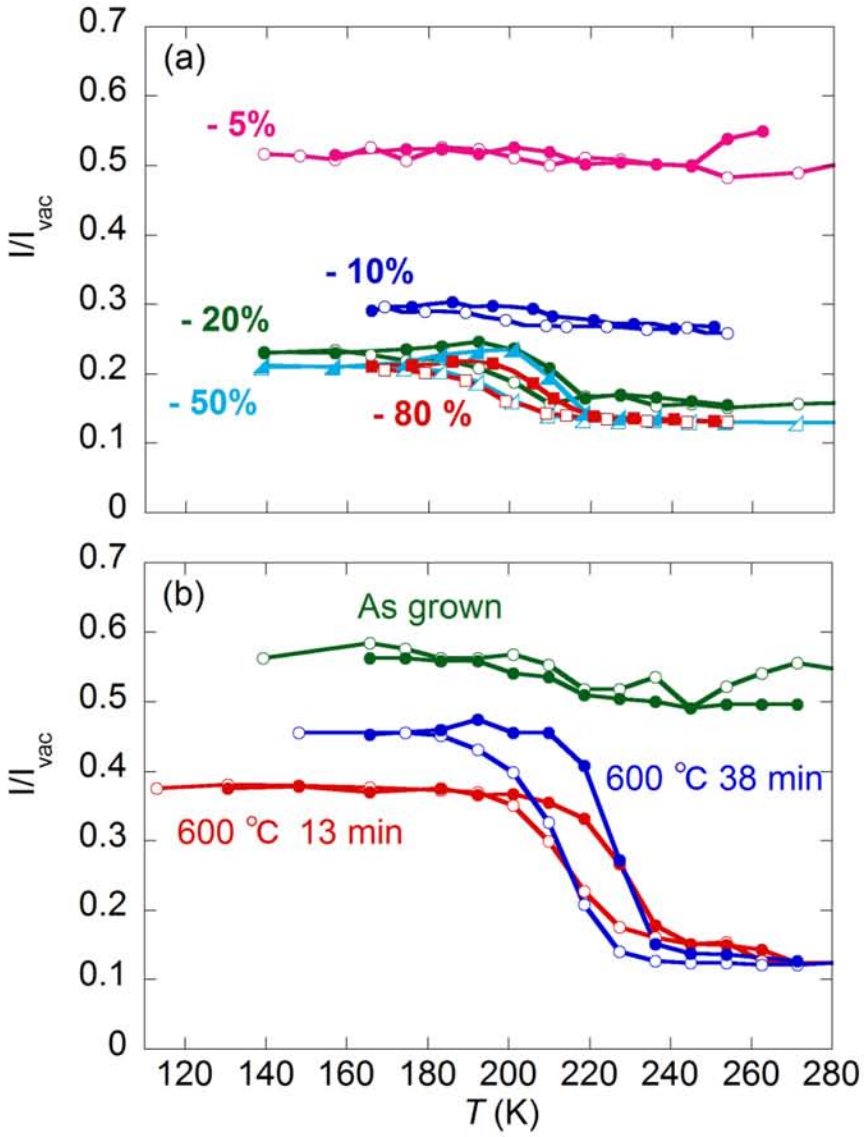

Fig. 4.3. (a) T dependence of the (10) Bragg peak intensity in 1.68 nm water-SWCNT samples with different weight loss by heating. (b) T dependence of (10) Bragg peak intensity in 2.40 nm water-SWCNT samples with different heat-treatment times. Open and filled symbols indicate the cooling and heating process, respectively. The intensity was normalized by those of the empty SWCNT samples.

4.1.2. NMR in Water-SWCNTs

We performed ^{2}D-NMR experiments on D_2O-SWCNT systems to obtain information on the dynamical nature of water inside the SWCNTs. The NMR spectra and T dependence of the signal intensity are shown in **Fig. 4.4**. Narrow NMR lines were observed above about 240 K in all the samples examined. This implies that the water molecules exhibit fast molecular motion in the NMR time scale. This phenomenon is known as the motional narrowing effect on the NMR spectrum.[130, 138] The motional narrowing condition is given by $(2\pi f)\tau << 1$, where τ is the correlation time of the relevant motion and f is the NMR spectral width in the static limit. In the present case, f must be about 200 kHz due to the electrical quadrupole interaction with the electric field gradient at the nuclear site in a D_2O molecule.[85] (Note that the ^{2}D nuclear spin has an electrical quadrupole moment because of spin I=1.) This interaction is almost dominated by the intra-molecular nature of the D_2O molecule and the line broadening is caused by anisotropy of the electric field gradient combined with the distribution in the orientation of the water molecules, hence τ should be the rotational correlation time for the water molecules. The narrowed spectra imply the presence of rotational motion faster than the time scale of 10^{-5} sec at least above 240 K in all the samples. However, the spectra were not extremely narrow but exhibited small double peaked structures with a separation of about 2 kHz. Similar spectra have been reported in a 1.35 nm SWCNT sample with water.[85] While the origin of the double peaked structures is not fully understood, this is probably due to a slight deviation

from the isotropic molecular rotation of water molecules in SWCNTs; water molecules may have a weak preferential orientation inside SWCNTs.

With lowering of the temperature below 240 K, the NMR intensity drastically decreased. This is clearly demonstrated in **Fig. 4.5** where the NMR intensity multiplied by T is plotted as a function of T. (Note that the nuclear magnetization, which is observed through NMR measurement, is proportional to $1/T$ within the usual high temperature approximation.) In **Fig. 4.5**, we find that the intensity begins to decrease substantially below a certain temperature T_{NMR}, which is close to T_{wd}, while the intensity is nearly constant above T_{NMR}. This is caused by the broadening of the NMR spectra beyond the observation window of the NMR system used in the present experiments, suggesting the slowing down in rotational motion of water molecules at lower temperatures. The loss in the NMR signal due to freezing of molecular motion is clearly demonstrated in the bulk D_2O water in **Fig. 4.4**; the spectra completely disappeared with freezing of water below 275 K.

More insight into the water dynamics in SWCNTs was obtained from ^{1}H-NMR of the H_2O molecules adsorbed in the 1.94 nm SWCNT sample. **Figure 4.6** shows the obtained spectra and their line-widths as a function of temperature. It was found that the spectra observed above T_{NMR} are much sharper than those in the static limit (FWHM of about 50 kHz). This is similar to the ^{2}D-NMR spectra, but in the present case, motional narrowing is caused by both rotational and translation motions of water molecules because ^{1}H with spin I=1/2 is a non-quadrupole nucleus and the spectral width is determined by both the intra and intermolecular ^{1}H-^{1}H dipolar

interactions. Therefore, contrary to the case of ^{2}D-NMR, additional information on the translational motion of water molecules can be obtained. The observed spectra above T_{NMR} are much sharper than expected from the inter-dipolar interaction, of about 20 kHz. Therefore, the narrowed spectra indicate that the translational motion is faster than the NMR time scale of 10^{-5} sec above T_{NMR}. Combined with the results of XRD and ^{2}D-NMR, the above observations strongly suggest that water in the SWCNTs is in a liquid state above $T_{NMR} \approx T_{wd}$.

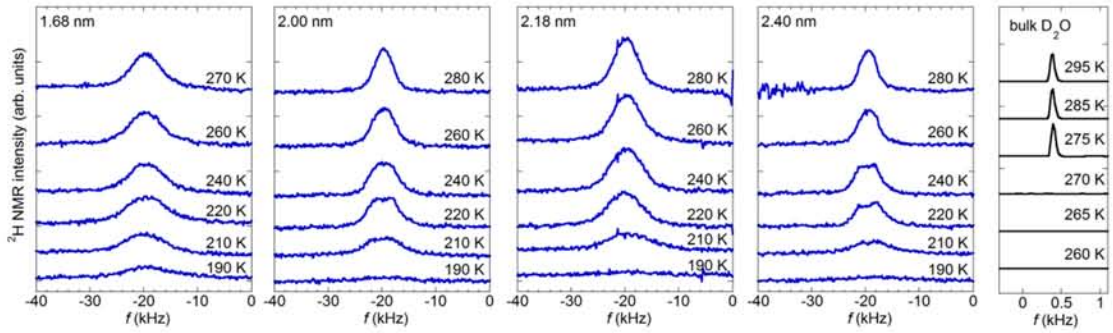

Fig. 4.4. Examples of ^{2}D-NMR spectra in water-SWCNT samples with mean SWCNT diameters of 1.68, 2.00, 2.18, and 2.40 nm from left to right. The spectra were shifted vertically for convenience of viewing. For the NMR observation, the pulse Fourier transform technique at a frequency of 26.24 MHz using a π/2-pulse sequence was used. For comparison, the spectra of bulk water were also obtained at a frequency of 26.22 MHz. The origin for the NMR shift is arbitrary.

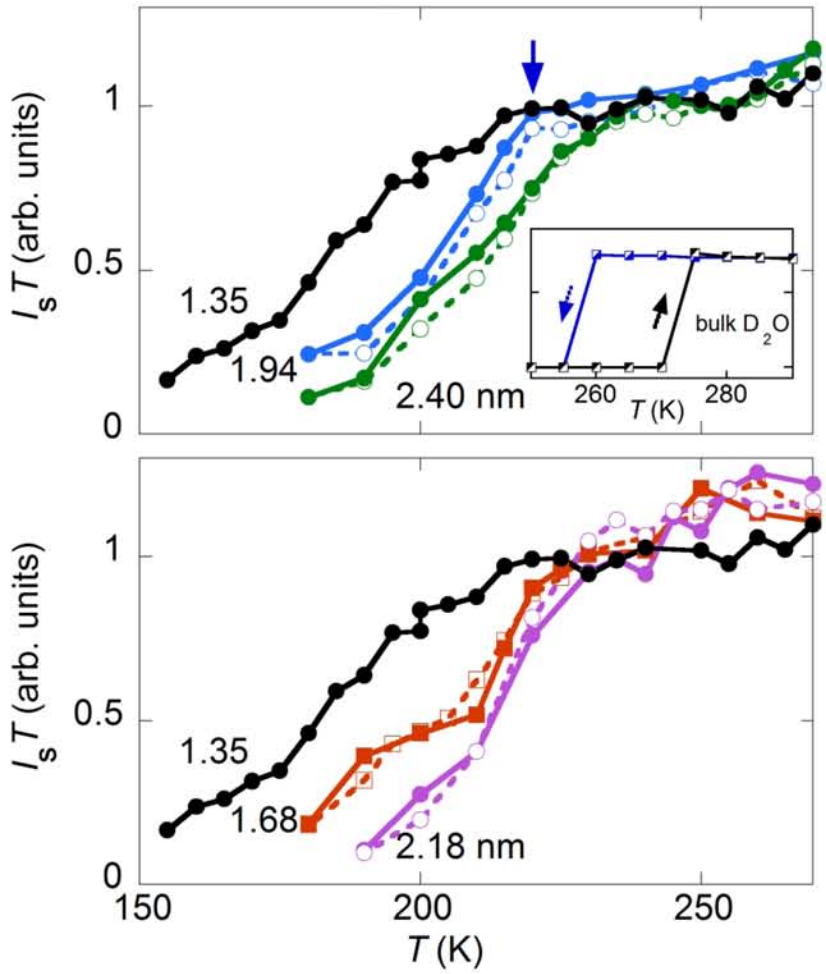

Fig. 4.5. ^{2}D-NMR intensity in water-SWCNT samples with mean SWCNT diameters of 1.94 and 2.40 nm (upper), and 1.68 and 2.18 nm (lower). The intensity for the 1.35 nm SWCNT sample is also shown for comparison. The arrow indicates T_{NMR} for the 1.94 nm SWCNT sample. The inset shows the T-dependence for the bulk D_2O.

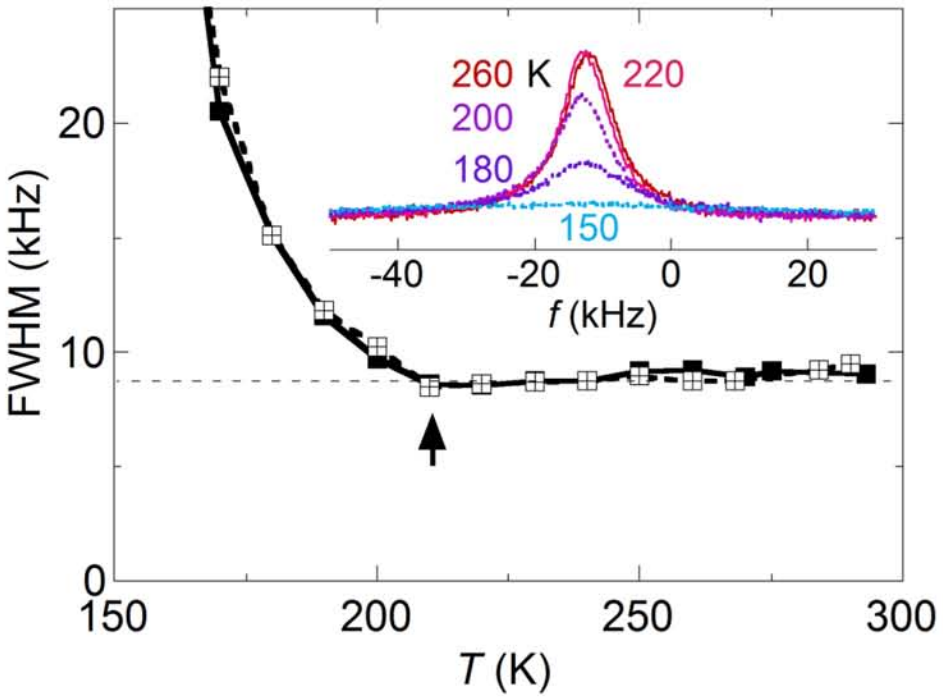

Fig. 4.6. ^{1}H-NMR of the 1.94 nm SWCNT sample filled with water at 300 K, showing the T-dependence of the full width at half maximum (FWHM) of the NMR spectra. Inset: NMR spectra at several temperatures; T = 260, 220, 200, 180, and 150 K. The NMR intensity is multiplied by T. NMR was observed by the pulse Fourier transform technique at an NMR frequency of 170.82 MHz using a π/2-pulse sequence. The arrow indicates T_{NMR} for the 1.94 nm SWCNT sample.

4.1.3. Electrical Resistance of Water-SWCNT Films

It is known that the electrical resistance of a heat-treated SWCNT film drastically decreases when the film is exposed to water vapor.[27, 82, 139, 140] Although the mechanism for this is not fully understood yet, one possible explanation is carrier doping in the semiconducting SWCNTs upon water adsorption. It has been reported that each individual semiconducting SWCNT, or a mixture of metallic and semiconducting SWCNTs, shows global *p*-type semiconducting behavior, and the adsorption of water acting as an electron donor changes the conductivity of the SWCNTs from *p*-type to *n*-type.[140, 141] A recent study by means of Fourier transform infrared (FTIR) absorption measurements has suggested that water molecules adsorbed on SWCNTs inject carriers to the first subband of the semiconducting SWCNTs.[142] Another explanation is related to mechanical and/or electrical modification of inter-tubule or inter-bundle contacts with water. When the contact resistance among SWCNTs in a bundle and/or among SWCNT bundles governs the bulk resistivity, water can easily affect the bulk resistivity by modifying the nature of the contact, such as the bundle-bundle distance, and potential barriers for electron hopping at the contacts. It is worth noting that electron hopping among conducting domains or localized states has been reported to play an important role in the electrical conduction mechanism of metal or semiconducting-enriched SWCNT films.[143] In any case, resistivity is a good measure to detect water adsorption-desorption properties in the water-SWCNT system. Actually, the emptying phenomenon of water or the "exchange transition" in a

water-SWCNT system with a mean SWCNT diameter of 1.35 nm was sensitively detected by resistivity measurements in a gas environment.[27] Therefore, we performed similar resistance measurements for the 1.68 nm and 2.00 nm SWCNT films in the present study.

Figure 4.7(a) shows the results for the 1.68 nm SWCNT film in water vapor as a function of temperature, along with that of the dry film before water exposure. We find that the resistance substantially decreased in water vapor, and even became metallic ($dR/dT > 0$) at higher temperatures. This is similar to the results previously reported for the 1.35 nm film in water vapor. Besides, in the present case, an anomaly in the T dependence appeared upon further decrease in T: The resistance abruptly increased below a well-defined temperature T_R with large hysteresis. Essentially the same behavior was observed in the 2.00 nm SWCNT film as shown in **Fig. 4.7(b)**. These are quite different from the behavior observed in the 1.35 nm SWCNT film, which showed a gradual change with little hysteresis, as shown in **Fig. 4.7(b)**. The observed T_R is very close to T_{NMR} and T_{wd}, suggesting the same origin for these anomalous behaviors.

The resistivity anomaly in the present experiments is similar to that observed in a water-SWCNTs system with a mean SWCNT diameter of 1.35 nm in a gas environment.[27] In that case, the anomaly was explained by "exchange transition", in which water inside the SWCNT is replaced by the environmental gas molecules on cooling. The exchange transition should be a result of the competition between water molecules and environmental gases being more stable inside SWCNTs. We performed similar experiments on the

present thicker SWCNT samples. The results of XRD and resistivity measurements are shown in **Figs. 4.8(a)** and **(b)** for oxygen and methane gases with 0.1 MPa pressure. The measurements were performed on water-SWCNT samples with D = 2.00 nm and 1.94 nm. Although the mean diameter is slightly different, both are essentially the same because the diameter distribution for both is much larger than the difference.

Figure 4.8(a) shows the effect of environmental gases on the resistance. While the oxygen hardly changed T_R, the methane led to a substantial increase in T_R. At almost the same temperature, we found that the (10) intensity in the XRD patterns also grew. These behaviors are the same as those in the "exchange transition".[27] The increase in the resistance below T_R implies desorption of water from the SWCNTs. Also, the increase in the (10) intensity indicates a decrease in electron density inside the SWCNTs. Since methane (or oxygen) molecules are more thinly packed in the SWCNTs compared to water molecules within the temperature range presently examined, the invasion of these gases into the SWCNTs lowers the averaged electron density inside the SWCNTs. An important observation is of behavior similar to the exchange transition even without the presence of environment gas molecules (nominally below 10^{-1} Torr), which implies that water is ejected from the inside of the SWCNTs in the absence of environment gas molecules, as discussed in detail later.

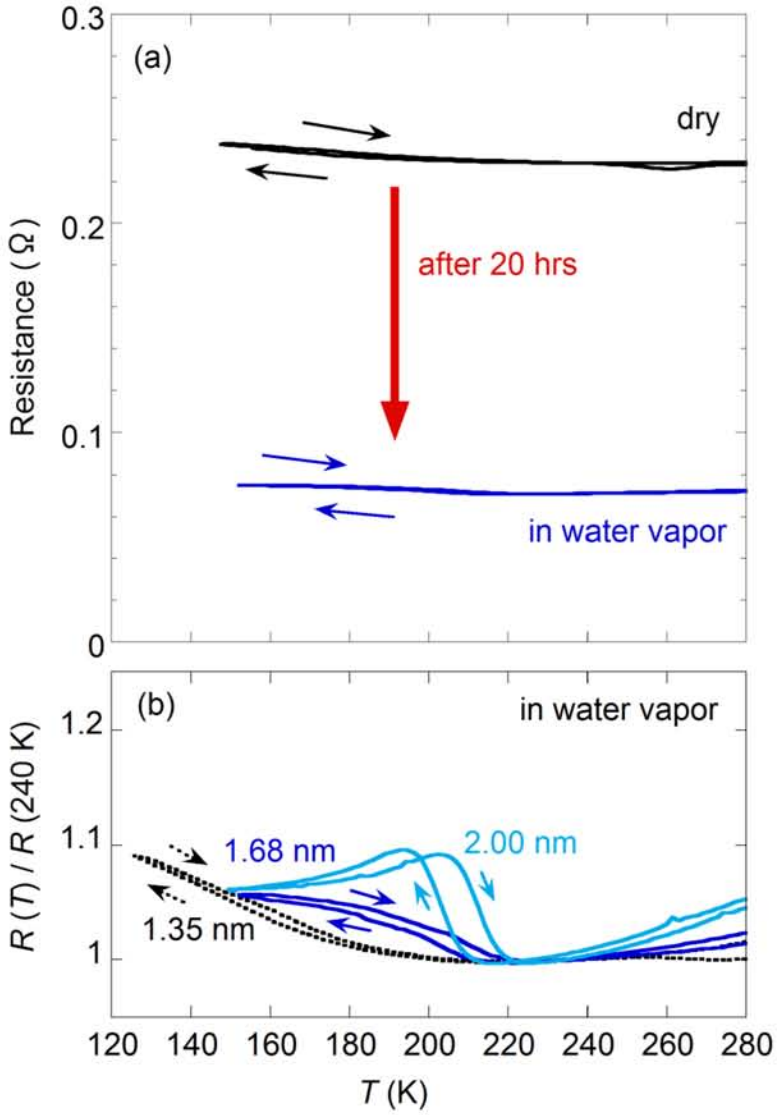

Fig. 4.7. (a) T dependence of the electrical resistance of the wet and dry SWCNT samples with a mean diameter D = 1.68 nm. (b) T dependence of normalized electrical resistance of wet SWCNT samples with diameters of 1.35, 1.68, and 2.00 nm. The 1.35 nm SWCNT sample was examined previously.[27] The resistance was normalized at 240 K.

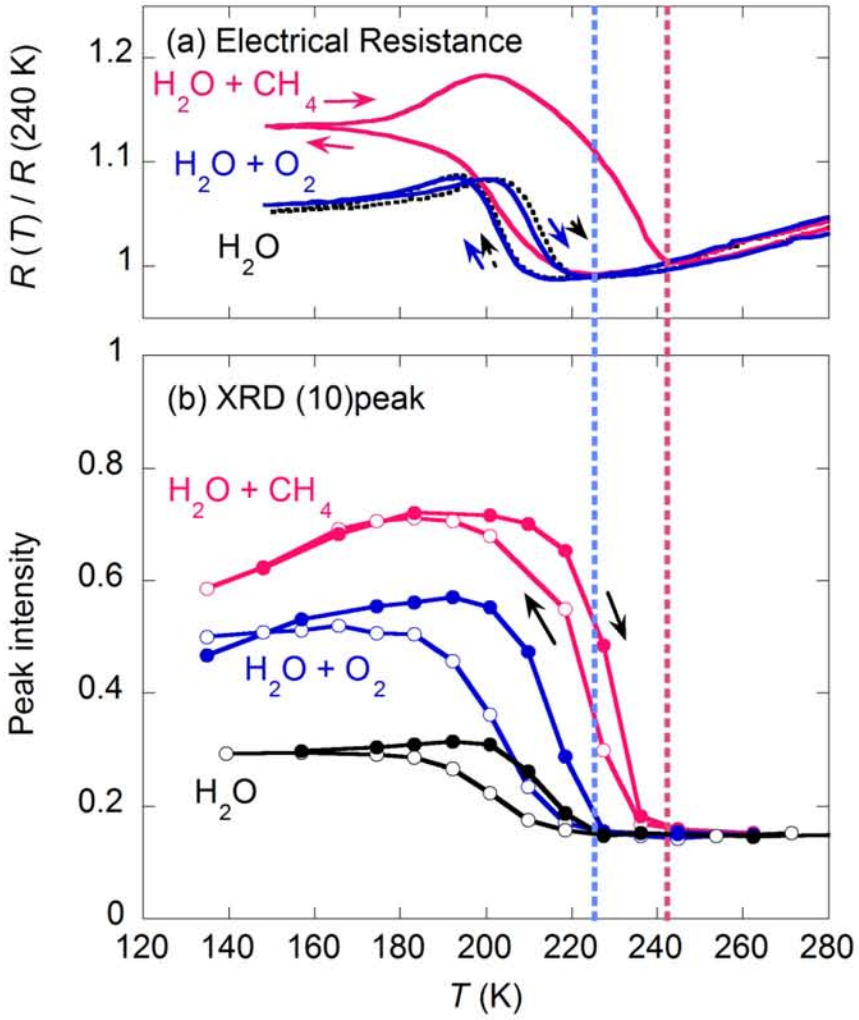

Fig. 4.8. Effect of oxygen and methane gases on electrical resistance and XRD intensity. The result without gas is also shown. (a) T dependence of the normalized electrical resistance of the wet SWCNT sample with $D = 2.00$ nm. The resistance was normalized at 240 K. (b) T dependence of the (10) XRD peak intensity in the 1.94 nm SWCNT sample filled with water.

4.1.4. Wet-dry Transition in SWCNTs with D> 1.6 nm

To clarify origin of the increase in the XRD (10) peak intensity below T_{wd}, we performed detailed simulations of the XRD profiles. There are three possible factors that could cause an increase in the (10) intensity in water-SWCNTs at low temperature: 1) A change in the water distribution within the SWCNTs below T_{wd}, 2) water adsorption within interstitial channel (IC) sites surrounded by three neighboring SWCNTs below T_{wd}; the diameter of IC site is estimated to be $d \approx 0.155(D+\sigma)$ with a van der Waals gap distance σ between SWCNTs, and 3) reduction in water content inside the SWCNTs as a result of a wet-dry (WD) type transition at T_{wd}.

These possibilities were examined in detail for the 2.40 nm SWCNT sample by simulating the XRD patterns with a homogeneous charged hollow cylinder model. The simulated and observed XRD patterns are shown in **Figs. 4.9(a), (b) and (c)**. The XRD patterns in **(a)** were calculated for three different water density profiles ρ (r) , #1-3. Profile #1 was obtained from MD calculations at 300 K, wherein water molecules were encapsulated in a fixed (20, 15) SWCNT with a diameter of 2.381 nm. The mean water density per unit length of the SWCNT was about 11 water molecules per 0.1 nm (molecules/nm). Profiles #2 and #3 are representative of multi-shell (layer) structures of ice, as reported in the MD calculations at low temperatures or high pressures. These are for the same water content of 11 water molecules per 0.1 nm, but with a slight difference in the water distribution; the inner shells of profile #3 are broader than those in profile #2. We found from the comparison that the observed pattern at 300 K is well reproduced by #1,

although there were no substantial differences between #1, #2 and #3. In contrast, the low temperature pattern at 160 K could not be reproduced by any reasonable water distribution including #1 and the multi-shell structures #2 and #3. Therefore, we assumed additional water adsorption at the IC site, wherein the water content was examined up to 0.6 molecules per 0.1 nm. The results are shown in **Fig. 4.9(b)**. Even for this case, although the (10) intensity increased, the increased intensities were too small to reproduce the observed anomaly. Finally, it was found that the water density inside SWCNTs must be reduced by ~50% to reproduce the observed profile at low temperatures. This implies *the emptying of water with decreasing temperature*.

In the present XRD simulations, the density of the confined water is averaged along the tube axis of the SWCNTs. However, the (10) peak intensity slightly varies depending on the distribution of water molecules along the tube axis and the distribution among the SWCNTs in a bundle. Thus, this effect as well as an effect of the finite bundle size was included in XRD simulations using Debye formula. In the simulation, a bundle consisting of three (22,13), two (21,18), two (16,16), one (30,10), and one (15,15) SWCNT, whose diameters ranging from 2.0 to 2.8 nm, was used. The length of the SWCNTs was set to about 4.6 nm. To obtain the atomic coordinates of water molecules inside the SWCNTs, MD simulations of the system were performed taking the water content as a parameter. In the case of partial water filling, it was found that water molecules form clusters inside SWCNTs.

Comparing the calculated patterns in **Fig. 4.10(a)** with the observed ones shown in **Fig. 4.10(b)**, it is found that the simulations successfully reproduce the observed patterns. The water content inside the SWCNTs was 12 molecules/nm at 290 K and 6.2±1.6 molecules/nm at 150 K averaged over a bundle of SWCNTs. The error is mainly due to the uncertainty in the location of the water clusters among SWCNTs. These estimated water contents are almost consistent with those calculated by the homogeneous charged hollow cylinder model.

As shown in **Fig. 4.11**, we also examined the effect of slow and rapid cooling for the 2.40 nm SWCNT sample using detailed XRD experiments.[144] It was found that the (10) intensity, i.e. the water contents, strongly depends on the temperature variation sequence. Here, the heating/cooling rates shown in the figure are the average rates of temperature variation throughout the whole sequence of each measurement, except for the data marked with an asterisk, which was measured at a constant cooling rate of 1.0 K/min without breaking. When the measurements were performed under a cooling rate of 0.16 K/min, the (10) peak intensity recovered up to 72% at around 200 K . This is compared to 45% for 1.0 K/min and 1.4 K/min. Such behaviour is likely caused by the slow kinetics of the emptying process. On the other hand, when the sample was quenched from 300 K to 110 K within about 30 s, the increase in the (10) intensity was very small. Then, upon heating, the intensity started to increase around 160 K. This behavior implies that the quenched water at 110 K is frozen inside the SWCNTs and then becomes mobile on heating above 160 K, leading to emptying.

On the basis of the above observations, we propose that T_{wd} is a kind of wet-dry transition (WDT) temperature. The resistivity anomaly is consistent with the present interpretation, because of the similarity to those in the "exchange transition" of water and environmental gas. The NMR observations indicate that the dynamic motion of water molecules slows down below T_{NMR}, which is close to T_{wd}. This may suggest that the WDT and the change in dynamic properties of water inside the SWCNTs take place simultaneously. We also note that T_{wd} (and T_{NMR}) lowers with decreasing the SWCNT diameters. Since it is a similar D dependence to the melting/freezing temperature T_m of the bulk water in a capillary[52-55], we performed a temporal analysis using a modified Gibbs-Thomson equation $273 - T_{wd}(D) = C/(D - D_0)$ with constants C and D_0. In the present case, C and D_0 are estimated to be about $78\ \mathrm{K \cdot nm}$ and $0.3\ \mathrm{nm}$, respectively. Here $D - D_0$ is assumed to be the bore diameter of the SWCNTs, and $D_0 \approx 0.3$ nm is almost equivalent to the thickness of a carbon atom. (Note that the SWCNT diameter is defined with respect to the position of the carbon nucleus.)

In the small-diameter region, on the other hand, water exhibits a liquid-solid-like transition and forms ice NTs. The liquid-solid-like transition temperature decreases with increasing SWCNT diameter, which has been reproduced by MD simulations.[121, 122] On cooling, characteristic Bragg peaks appeared around $Q \sim 22\ \mathrm{nm^{-1}}$ (and $44\ \mathrm{nm^{-1}}$) in the XRD patterns which were assigned to one-dimensional ice, or ice NTs, as discussed in **3.2.2.**.[25-28] However, the 2.40 nm SWCNT sample did not show any such peaks, as discussed later, and even over the entire Q range examined [see **Fig. 4.1(d)**

for $Q < 10$ nm^{-1}]. The lack of such peaks of ordered water was common in the thicker SWCNT samples with $D > 1.6$ nm within the present experimental limitations. Thus, there was no XRD evidence for the presence of any ordered ice structures for $D > 1.6$ nm.

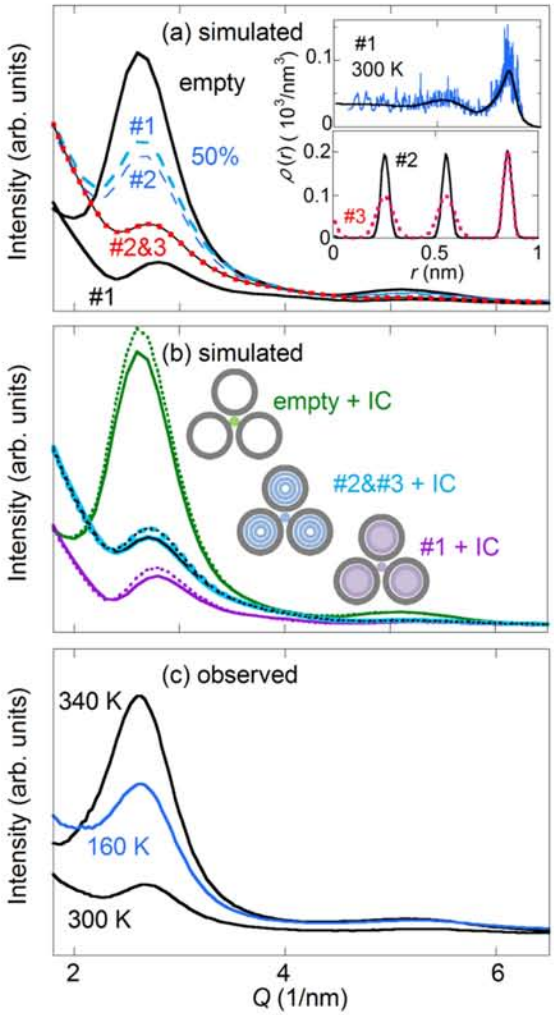

Fig. 4.9. (a) Simulated XRD patterns of empty SWCNTs and water-filled SWCNTs with water distributions #1, #2, and #3 shown in the inset. Dashed lines represent data for a water content 50% of that of full water adsorption. The mean SWCNT diameter is 2.381 nm. (b) Simulated XRD patterns of empty and water-SWCNTs whose IC sites were filled with water. The solid lines represent the profiles for which 0.3 water molecules were contained in IC sites 0.1 nm in length, while the dashed lines are for 0.6 water molecules. The water density within the SWCNTs is the same as that in (a). (c) Observed XRD patterns of the water-SWCNT sample with a mean diameter of 2.40 nm. Temperature varied at a rate of 1.4 K/min.

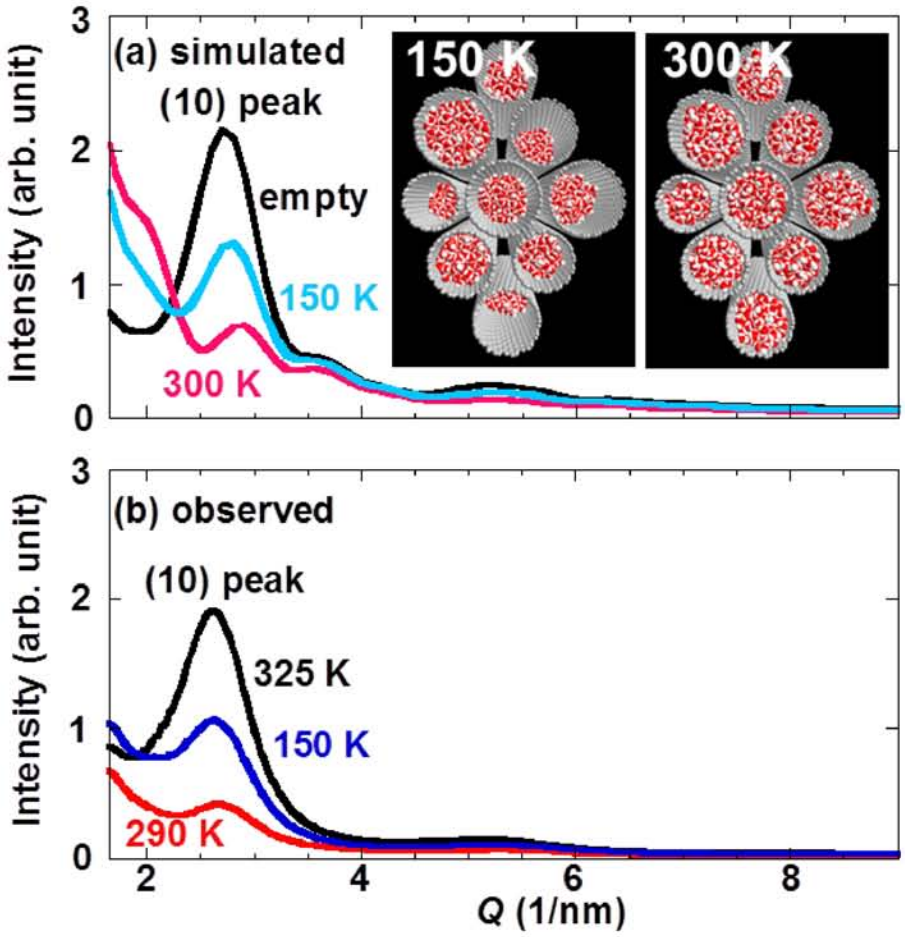

Figure 4.10. XRD patterns of the water-SWCNT sample in the low Q range. **a,** Simulated XRD patterns for bundles with water contents of 0, 50, and 100% of the maximum possible at 300 K. The bundle consists of three (22,13), two (21,18), two (16,16), one (30,10), and one (15,15) SWCNT 4.6 nm in length. The water forms clusters placed randomly inside the SWCNTs as shown in the inset. **a,** Typical examples of observed XRD patterns for the SWCNT sample with D=2.40 nm. Temperature varied at a rate of 1.4 K/min.

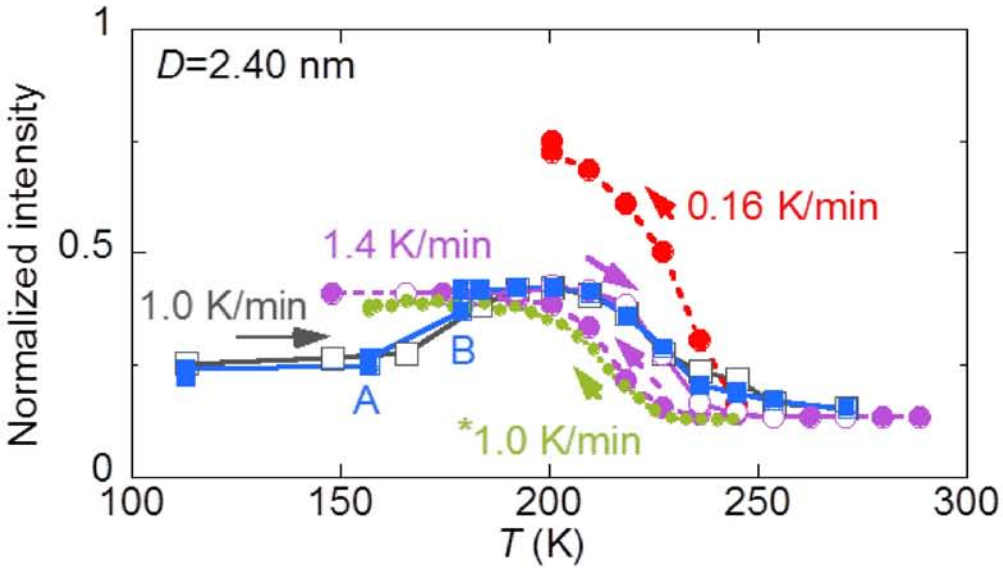

Fig. 4.11. Cooling rate dependence of the XRD (10) peak intensity in the 2.40 nm SWCNT sample filled with water at 300 K. The cooling/heating rates are given in the figures. The intensity was normalized by that of the empty SWCNT sample. Closed and open circles are data taken with decreasing and increasing T, respectively. Squares denote data taken while increasing temperature after quenching to 110 K from 300 K within about 30 s. At A and B for closed squares, temperature was held for 70 and 120 min, respectively.

4.1.5. Optical Microscopy Observation of Wet-dry Transition

To obtain more direct evidence for WDT, we also tried in-situ observations of a water-SWCNT sample through optical microscopy. As a result, the appearance and disappearance of water droplets on the surface of SWCNTs around T_{WDT} ~220 K were clearly observed. This took place reversibly with increasing and decreasing temperature. Examples of the photographs taken of an SWCNT sample sealed with water are shown in **Fig. 4.12**. The ejected water crystallizes into ice Ih as discussed later in Chapter 5.

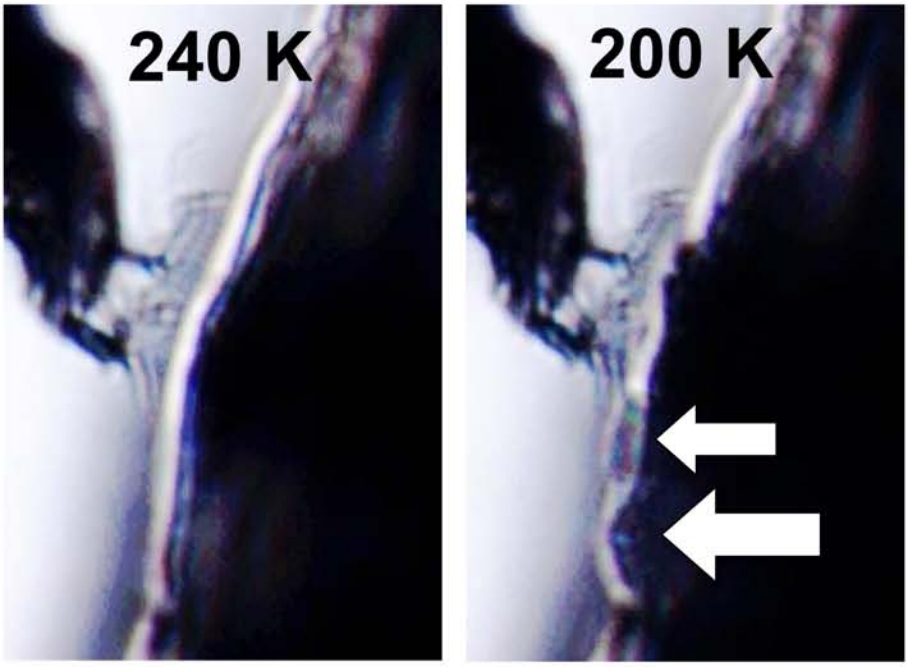

Fig. 4.12. Optical microscope images above and below 220 K.
The left image was taken at 240 K, while the right at 200 K. Below 220 K, water is ejected as indicated by the arrows.

4.2. Results and Discussion

: Effect of Open Ends of SWCNTs on Water Structures

4.2.1. MD Calculations for Water-SWCNT Systems

The global T-D phase diagram obtained so far, as discussed above, is summarized in **Fig. 4.13.** An anomalous line T_{wd} was found above $D > D_c$ ~1.4 - 1.5 nm in the present study. T_{wd} was proposed to be a WD type transition temperature. We now shift our attention to the intermediate diameter range D_c. In this D range, previous MD calculations have predicted the formation of multi-layer structures of ice inside SWCNTs. [122, 123] A one-dimensional water chain inside a nanotube-shell structure was also found in computer simulations,[83, 91] which was experimentally assigned to ultra-soft dynamical water observed in neutron quasi-elastic scattering experiments of a 1.4±0.1 nm SWCNT sample.[83] These calculations did not fully clarify the effect of SWCNT edge on the water structure. Therefore, the present MD calculations focused on finite length SWCNTs to examine the effects of open ends of the SWCNTs on water structures. To investigate the effect of open ends of SWCNTs, the so-called "edge effect", on the water structure and adsorption properties inside the SWCNTs, we studied finite length SWCNTs using MD.

A 1.429 nm SWCNT with an index (12, 9) with a finite length of 5.2 nm was modeled for the MD calculations and set in a simulation cell with a parallelogram base with sides $a = b = 6$ nm, base angles of $\theta = 60^\circ$ and length c of 10 nm so that the SWCNT axis was parallel to the long axis c.

The cell was filled up with water molecules whose number varied in the range of 100 - 230 molecules. The water molecules were described by the TIP3P water model. [133] A three dimensional (3D) periodic boundary condition was applied to the simulation cell. However, for a small number of water molecules in a 1.429 nm SWCNT with a length of 7.8 nm, the periodic boundary condition was not applied in order to save the simulation time, because in this case the filling of water inside the SWCNT was not complete and the water did not escape from inside the SWCNT at least at low temperatures. In order to ensure a fixed number of water molecules inside an SWCNT even at high temperatures, flat walls made of artificial atoms were located 0.3 nm from both ends of the SWCNT. The dimensions of the simulation cell were $a = b = 2\,\text{nm}$, $\theta = 60^\circ$, and $c = 10\,\text{nm}$. To investigate the size effect of the SWCNT bore, one of the L. J. parameters, σ_{OC}, was slightly varied around its default value of $\sigma_{OC} = 0.327531\,\text{nm}$. The system temperature was decreased from 340 K to 100 K at a rate of 12.5 K/ns.

The results of the simulations are shown in **Fig. 4.14.** Interestingly, the structure of nano-ice formed at low temperatures was affected not only by the SWCNT bore diameter but also by the number of water molecules in the present systems. The hollow ice NTs were formed with a small amount of water. Interestingly, ice NTs containing a one-dimensional (1D) water chain[83, 91] appeared for a large amount of water [**Fig. 4.14(b)**, #4, #6, and #8]. That is, once the hollow ice NT reached the SWCNT ends with increasing water content, additional water started to fill the inside of the ice NT, forming a 1D

water chain. This is definitely an effect of the finite length of the SWCNT (an *edge effect*). The water molecules are forced to enter the SWCNT as much as possible at the SWCNT open edges. A similar observation was obtained by Striolo *et al.* using grand canonical Monte Carlo simulations,[91] wherein, the empty tubule structure was obtained during desorption of water from a (10, 10) SWCNT with a filled water structure at 248 K. The results are very similar to the present ones calculated for the NVT ensemble. Furthermore, an interesting case is seen in the systems at the border of 6 and 7-membered ice NTs [**Fig. 4.14(b)**, #3 and #4]. While the 6-membered ice NT forms at a low water content, further increase in the water content transforms the "6-membered" ice NT to a "7-membered" ice NT encapsulating a 1D water chain.

For bore diameters smaller than about 1.02 nm [**Fig. 4.14(b)**, #1 and #2], empty 6-membered ice NTs were formed, irrespective of the number of water molecules. On the other hand, for bore diameters larger than about 1.10 nm [**Fig. 4.14(b)**, #9], filled water clusters formed even for small water content, which then grew with increasing water content. The nano-ice structures predicted at low temperatures are summarized in **Fig. 4.14(a)** as a function of the bore diameter, $a = D - \sigma_{OC}$. The results for the intermediate diameter (about 1.02 - 1.10 nm) show that water molecules are stuck on the inner wall of the SWCNT at first, and then fill the hollow space with an increase in their number. This behavior differs from that in the bulk, where water forms a cluster when confined in a narrow capillary.

Figure 4.15 shows the potential energy per water molecules for the two

different bore diameters, (a) $\sigma_{OC} = 0.387531\,\mathrm{nm}$ and (b) $\sigma_{OC} = 0.327531\,\mathrm{nm}$, as a function of temperature. The potential is the sum of the contributions from the water-water intermolecular interaction and the water-SWCNT interaction. It was calculated for two different water contents of N= 175 and 115, dense and sparse cases, respectively. We found that the potentials steeply decreased around 260 K for (a) and 210 K for (b) on cooling. By checking the snapshot structures, these were assigned to "transition temperatures" to the solid-like ordered states, as shown in the figures, from the liquid-like disordered states. Interestingly, the transition behavior of the filled structures ("7+1D" and "8+1D") and the hollow ("7+hollow" and "8+hollow") structures are very similar, while the filled structures formed at slightly higher temperatures by about 10 K. In addition, the hollow ice NTs were found to be more energetically stable than those containing a 1D water chain. Similar computational results have been reported by Shiomi *et al.* They mentioned that 8-membered ice NTs are sensitive to the simulation conditions, such as cooling speed and the temperature control method used, and they showed that the difference in the stability was mainly attributed to the water-SWCNT interaction potential.[121]

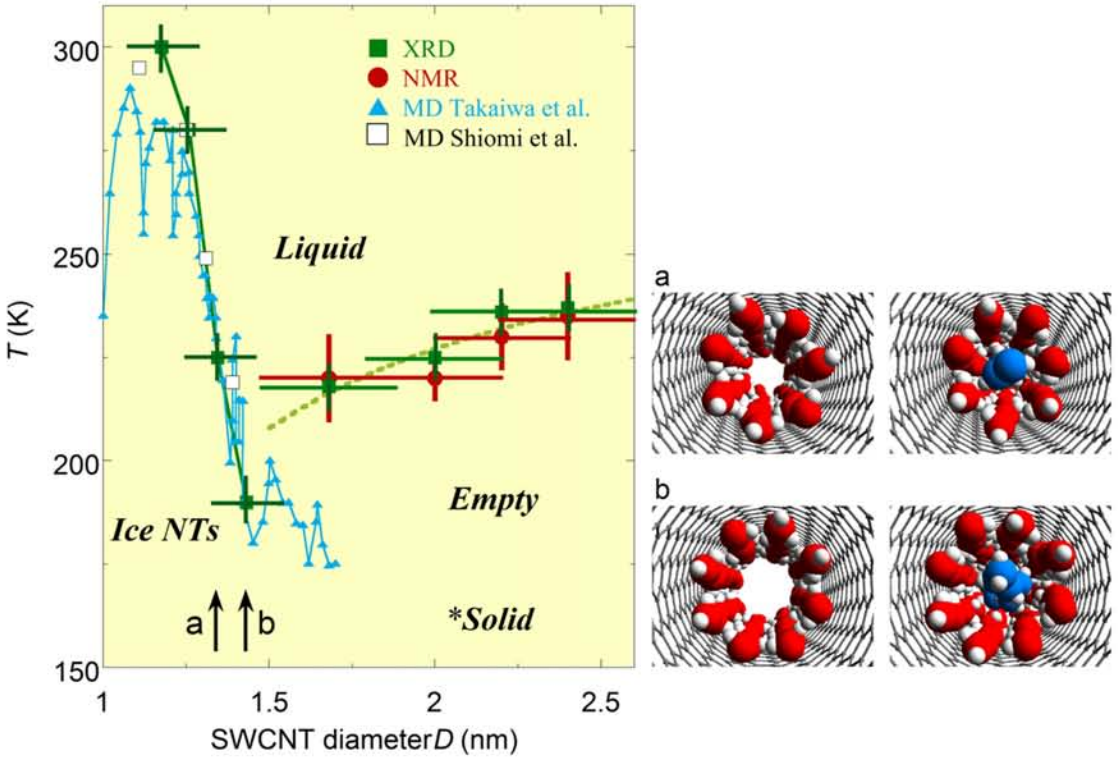

Fig. 4.13. Global temperature-diameter (T-D) phase diagram of water inside SWCNTs. Open squares and filled triangles data were obtained from MD simulations by Shiomi *et al.*[121] and Takaiwa *et al.*[122], respectively. Filled squares and circles represent experimental observations. The dotted line is an extrapolated melting point from bulk water with D_0 =0.3 nm (see text).[52-55, 146] Right: hollow and filled ice NTs calculated for SWCNTs at "a" and "b" with diameters of around 1.4 nm in the left figure. The hollow and filled ice NTs appear depending on the water content. At $D \approx 1.5$ nm, double- and triple-shell structures have been proposed to form.[122, 123]
*: quenched phase from the high T.

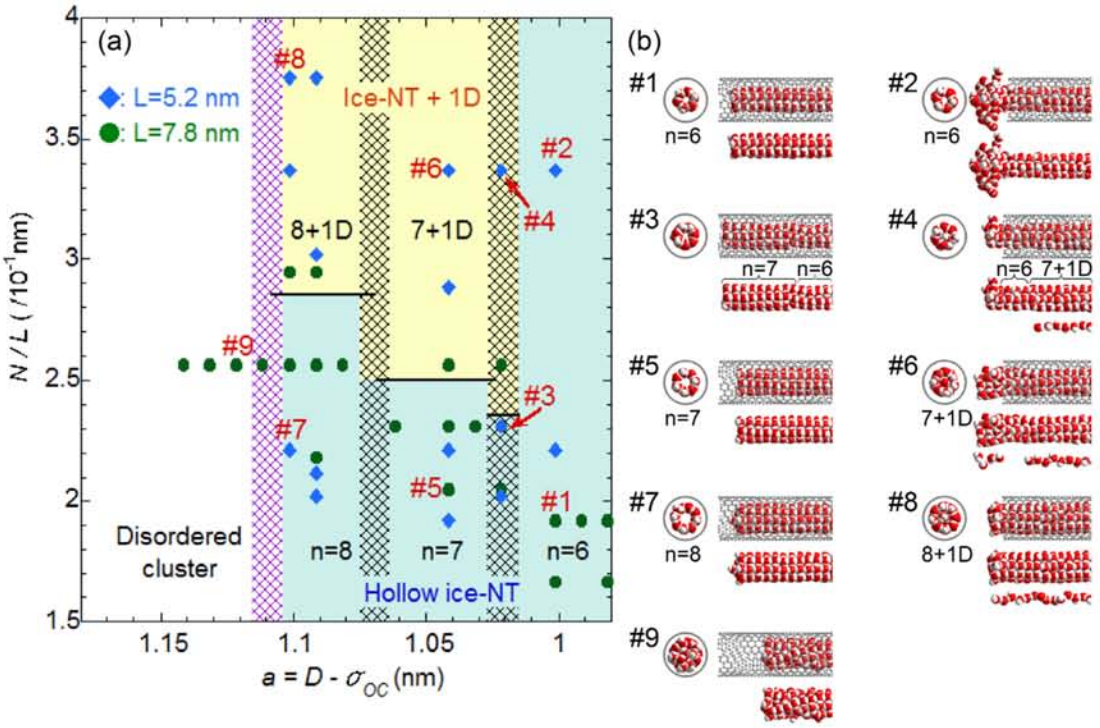

Fig. 4.14. (a) Low temperature phase diagram of ice NTs as a function of the SWCNT bore diameter, $a = D - \sigma_{OC}$, and the number of water molecules, N, in the system; D=1.429 nm. The shaded regions indicate the boundary between the n-membered to the (n+1)-membered ice NTs. (b) Snapshot structures of water inside the SWCNTs with a small number of water molecules (see #1, #3, #5, and #7), and with a large number of water molecules (see #2, #4, #6, and #8). A snapshot with a large bore diameter over 1.10 nm is also shown (#9). For the side views of the SWCNT, only the left-hand side is depicted.

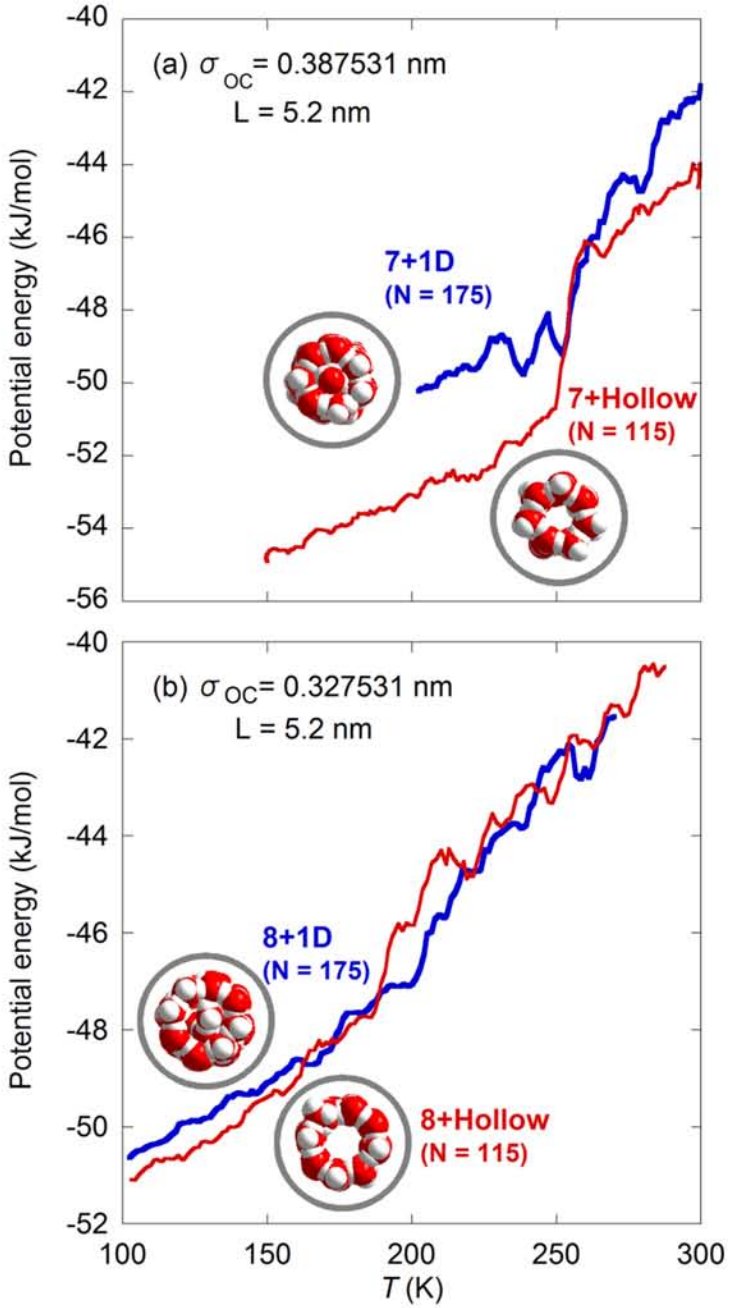

Fig. 4.15. *T* dependence of the potential energy per water molecules for the hollow and filled ice NTs. (a) σ_{OC} = 0.387531 nm, and (b) σ_{OC} = 0.327531 nm. The ice structures formed at lower temperatures are shown in the figures.

4.2.2. XRD Measurements of the Water-SWCNTs in the Intermediate Diameter Range

Based on the results of the MD calculations described above, we can discuss XRD profiles of the water-SWCNTs in the intermediate diameter range. **Figure 4.16(a)** shows experimentally observed XRD profiles of a water-filled SWCNT sample with D = 1.46 nm, and **Fig. 4.16(b)** shows the difference between the XRD patterns taken at high and low temperatures. As reported previously in thin SWCNTs with mean diameters <1.44 nm,[25-27] two Bragg peaks, A and B, appeared around Q ~ 22 nm^{-1} on cooling. These peaks indicate the presence of a 1D ordered structure with a periodicity of about 0.28 nm, which can be assigned to ice NTs. **Figure 4.16(b)** also shows the pattern for the 2.40 nm SWCNT sample for comparison. We found that the 2.40 nm SWCNT sample did not show such peaks, lacking any evidence for 1D ordered structures of ice. The peaks for the 1.35 nm SWCNT sample have been analyzed in detail.[25-27] **Figures 4.17(a) and 4.17(b)** show the temperature dependence of the intensities of peak A and B. With D = 1.35 nm, peak A was larger than peak B at low temperatures, while with D = 1.46 nm, peak B was larger than peak A. In addition, peak B appeared at a lower temperature than peak A. According to detailed analyses performed earlier, these facts indicate that peak B originates from ice NTs with larger diameters, such as 8-membered ice NTs. On the other hand, peak A may be a result of the formation of 6 and 7-membered ice NTs.

We next turn our attention to other Bragg peaks in **Fig. 4.16(a)**, at Q ~ 7.0 nm^{-1} and ~ 8.3 nm^{-1}, which can be indexed to (11) and (20) in the 2D

hexagonal lattice in the SWCNT bundle, respectively. For the 1.35 nm SWCNT sample examined previously, the (11) peak intensity increased while the (20) peak decreased below the temperature at which peak A appeared. This was interpreted as a change from the rather homogeneous water distribution in liquid-like states to tubule-like structures due to the formation of ice NTs inside the SWCNTs.[25, 26, 30] In contrast, in the 1.46 nm SWCNT sample, it was found in the present experiment that the (11) and (20) peaks hardly changed over the entire temperature range examined even below the onset temperatures of peaks A and B. This implies that the ice formed in the 1.46 nm SWCNT sample may be qualitatively different from the tubule structure and may be a filled structure, as suggested by the MD calculations.

To obtain more information on the ice structure inside the 1.46 nm SWCNTs, we calculated the XRD profiles for the two kinds of ice structures obtained by the MD calculations in the previous section, hollow ice NT and the ice NT containing a 1D water chain. First, the water density profile functions $\rho(\vec{r})$ inside the SWCNTs were calculated from the molecular coordinates of water within the region indicated by arrows in **Fig. 4.18(a)** and **(b)**. The XRD patterns were then calculated and compared with those obtained experimentally. Here, we assumed that the water content inside SWCNT was invariant over the entire temperature range. The calculated XRD patterns thus obtained are shown in **Figs. 4.18(a) and (b)**. We found that for the hollow ice NTs within the 1.46 nm SWCNTs, the (11) and even the (10) peak intensity became larger and the (20) peak became smaller

compared to those at 300 K [**Figure 4.18(b)**]. This does not suit the temperature dependence in the observed XRD patterns. On the other hand, in the case of the ice NTs containing a 1D water chain, there was only slight change in the (11) and (20) intensity between 300 K and 100 K [**Figure 4.18(a)**]. This filled model successfully reproduces the observed XRD patterns, assuming that the mean water density per unit length of the SWCNT is 2.8 water molecules per 0.1 nm. While this water content is slightly smaller than that obtained by the MD calculations at around 300 K (3.047 water molecules per 0.1 nm), this probably resulted from the presence of some unopened SWCNTs, which cannot allow water to be introduced within them. Therefore, the present observations strongly suggest that filled structures including an ice NT plus a 1D water chain structure exist within the 1.46 nm SWCNT.

Further examination of the ordered 1D Bragg peak appearing at Q ~22 nm^{-1} was carried out and compared with the experiments. We calculated the X-ray interference functions, I_{OO}, between the oxygen–oxygen (O–O) atoms in water at several temperatures.[28, 91] The calculations were performed using a built-in-tool in the MD software package. Here, I_{ij} between the i and j atoms is defined as:

$$I_{ij}(Q) = \frac{w_i f_i w_j f_j}{\left|\sum_k w_k f_k\right|^2} \times \frac{N}{V} \int_0^{r_m} [g_{ij}(r) - 1] \frac{\sin(Qr)}{Qr} 4\pi r^2 dr , \qquad (4\text{-}1)$$

where N is the total number of atoms, V is the system volume, w_i (= N_i/N) is the partial number of atom i, f_i is the atomic scattering factor for atom i,

and $g_{ij}(r)$ is the distribution function between i and j atoms. The X-ray interference functions are related to the X-ray diffraction patterns as:

$$I(Q) \propto \sum_{ij} I_{ij}(Q). \quad (4\text{-}2)$$

The calculated I_{OO} are shown in **Fig. 4.19**. Here, a Bragg peak appeared at Q~22 nm^{-1} on cooling below the transition temperature, 210 K for "8+hollow" and 220 K for "8+1D", which was determined from the T-dependence of the potential energy [see **Fig. 4.15(b)**]. The peaks were assigned to the periodic structure of the 1D array of polygonal ice rings in the ice NTs, whose periodicity is about 0.28 nm. Although the widths of the simulated peaks were larger and the peak positions shifted toward a high-Q direction compared to the experimental peaks, they may result from the small crystalline size used in the simulation, as discussed in previous work.[28] Importantly, the present simulations predicted the presence of the Bragg peak at Q ~22 nm^{-1} even in the filled ice NT structure, implying that the observed 1D Bragg peak is consistent with the filled structure.

Finally, we briefly compare our results with a previous study[83] dealing with the phase behavior of filled ice NTs. Kolesnikov *et al.* examined the formation of an ice-shell plus 1D water chain structure inside SWCNTs with D = 1.4±0.1 nm by inelastic neutron scattering experiments and MD simulations. They discussed the melting behavior using the temperature dependence of mean-square displacement of hydrogen, and reported no evidence for solid-liquid-like transition below 300 K. By contrast, the present study indicated that the ordering of the filled ice NT takes place below 220 K.

According to the present MD calculations for a=1.10 nm, this ordering occurred simultaneously at almost the same temperature for both the shell and inner water molecules below 300 K. While the results seem to be consistent with the present experimental results, more detailed studies would be needed for this issue because of possible sensibility of the transition temperature to the SWCNT diameter.

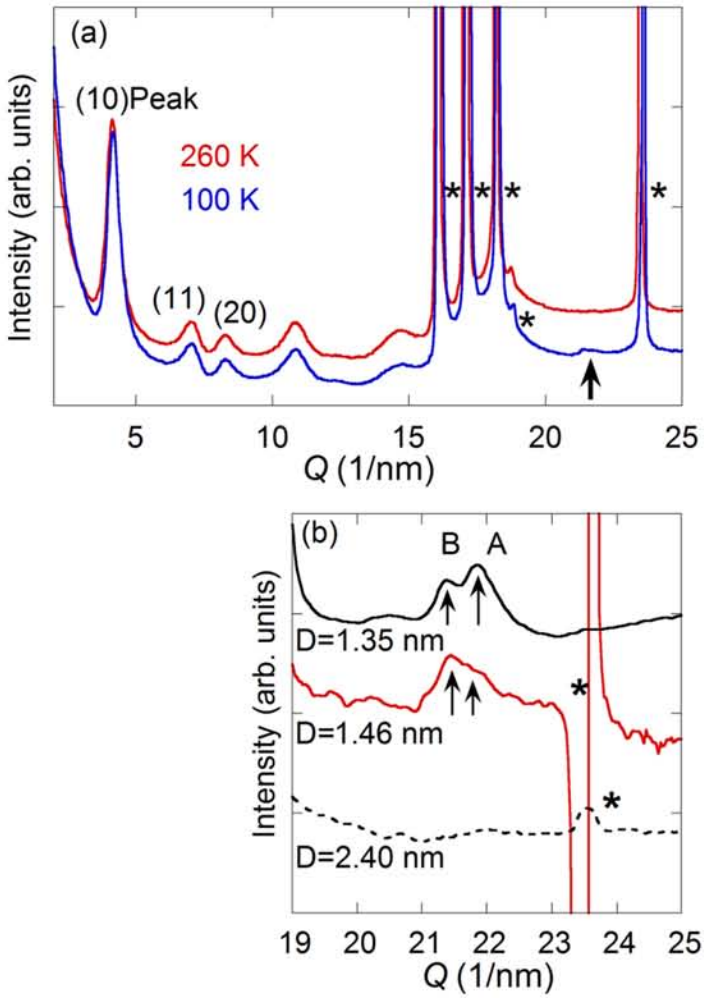

Fig. 4.16. (a) XRD patterns of the 1.46 nm SWCNT sample with saturated water vapor at 300 K. The arrow shows the appearance of a Bragg peak around $Q = 22$ nm^{-1} which appeared upon cooling. (b) Difference between the XRD patterns taken at high temperature (>240 K) and low temperature (about 100 K) around $Q = 22$ nm^{-1}. The XRD measurements for the 1.35 nm SWCNT sample have been previously reported. The 1D XRD peaks appeared in the 1.35 and 1.46 nm SWCNT samples at 100 K, while no new Bragg peaks appeared in the 2.40 nm SWCNT sample. The asterisks (*) denote Bragg peaks of bulk ice inside and outside of the XRD glass capillary.

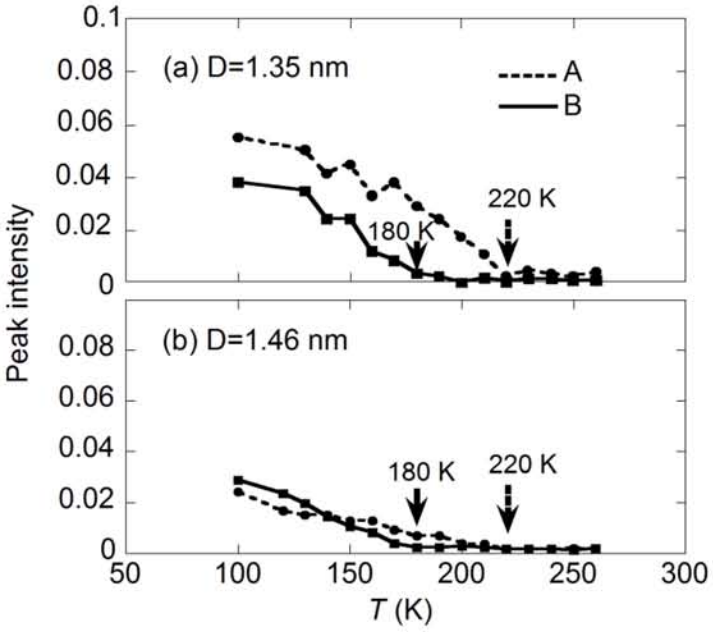

Fig. 4.17. T dependence of intensity of the 1D peaks which appear around Q = 22 nm^{-1}; (a) and (b) for the 1.35 and 1.46 nm SWCNT samples, respectively. The intensity was normalized by the (10) peak intensity.

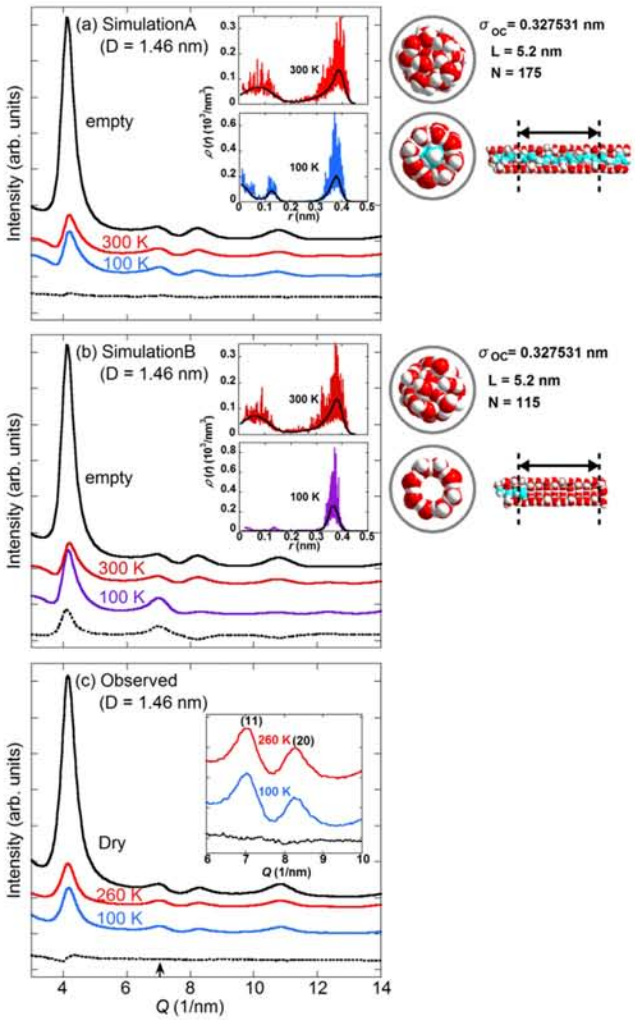

Fig. 4.18. Simulated and observed XRD patterns for the SWCNTs. The dashed lines show differences between the profiles taken at high and low temperatures. (a) and (b) Simulated XRD patterns of empty and water-filled SWCNTs with the water distributions shown in the insets. The snapshots on the right show the water structures corresponding to the distributions. Water molecules in the outer wall are in red-white, while those forming the 1D chain are in blue-white. (c) Observed XRD patterns of the dry and water-filled SWCNT samples with D = 1.46 nm. The inset in (c) shows expanded views of the (11) and (20) peaks at $Q \sim 8$ nm^{-1}.

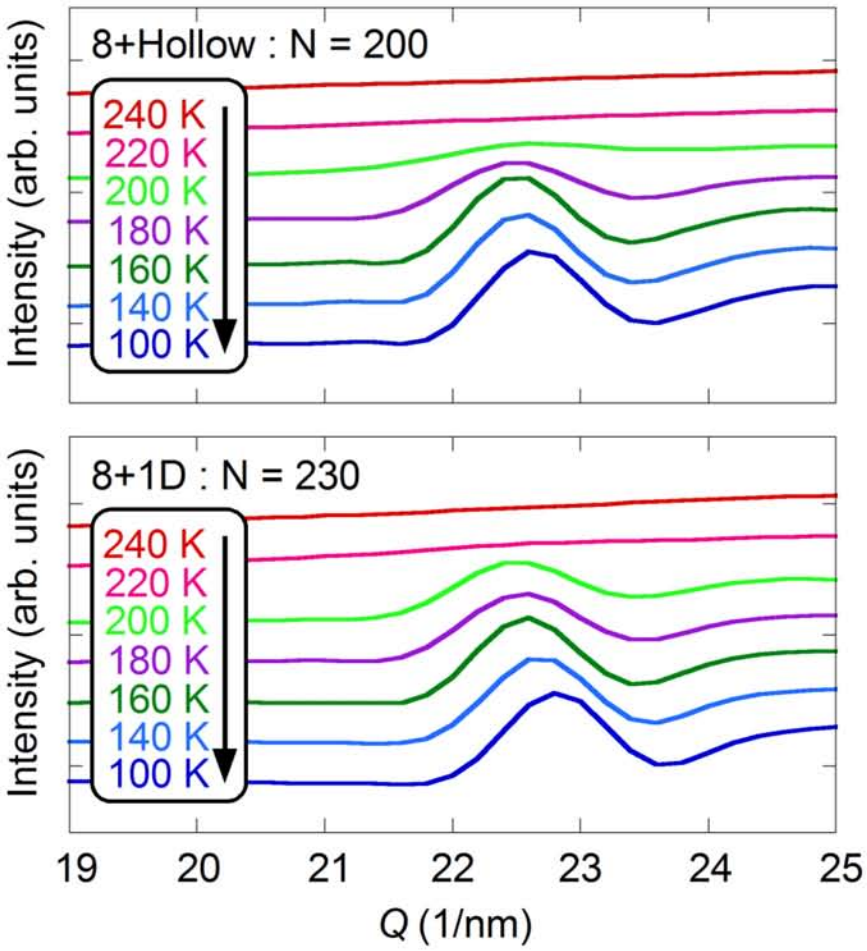

Fig. 4.19. T dependence of the Bragg peaks assigned to the 1D structure of nano-ice from the MD calculations for σ_{OC} = 0.327531 nm and L = 7.8 nm. Upper: the hollow ice NTs "8+hollow" formed below 210 K with N = 200. Lower: the filled ice NTs "8+1D" formed below 220 K with N = 230.

4.3. Summary

Combining previous reports,[25, 26, 145] the global T-D phase diagram of water confined inside SWCNTs was summarized in the SWCNT diameter range D from 1.17 to 2.40 nm, as shown in **Fig. 4.13**. In thinner SWCNTs ($1.17 < D < \sim 1.3$ nm), water inside SWCNTs undergoes a liquid-solid like transition, whose temperature has the opposite tendency to that of bulk water. The low temperature solid states have hollow ice nanotube (ice NT) structures. For the larger diameter SWCNTs ($\sim 1.6 < D < 2.40$ nm), on the other hand, water cannot be retained inside the SWCNTs. They exhibit a WD type transition, and the water is ejected from the inside of the SWCNTs. Its transition temperature lowers with decreasing the pore diameter D. In the intermediate diameter range (D ~1.4 nm), the filling with water substantially affects the low temperature structures; it was found that while hollow ice NTs form at a lower water content, further increase in the water content leads to filled structures, such as ice NTs containing a 1D water chain. Such dependence on the water content is caused by an edge effect of SWCNTs on the water structure. The mechanism for the WDT is discussed in the next chapter.

Chapter 5
Liquid-liquid Transition of Water Confined in SWCNTs

5.1. Results and Discussion

5.1.1. XRD of Water-SWCNTs

As discussed in chapter 4, the confined water inside thick SWCNTs (D > 1.6 nm) exhibits a WDT at low temperatures. In this chapter, we analyze the observed XRD patterns for the thick SWCNT samples in detail to clarify the structure of the confined water at low temperature as well as its phase transitional behaviour.

For the observed XRD data shown in Chapter 4, we examined their diffraction patterns in higher Q-range. Hereafter, results for the 2.40 nm sample are presented if not otherwise specified. The left panel of **Fig. 5.1(a)** was taken upon decreasing temperature at a constant rate of 1 K/min, corresponding to the data with small circles in **Fig. 4.11**. On the other hand, the left panel of **Fig. 5.1(b)** was taken upon increasing temperature after quenching to 110 K, the corresponding data to closed squares in **Fig. 4.11**.

In these figures, we can see broad diffraction in which peaks occur around Q~18 and 30 nm^{-1}.This is likely due to water diffuse diffraction (WDD)[147, 148], indicating that water inside the SWCNTs is in a liquid or glassy state over the whole temperature range. In the case of SWCNTs with

D <1.45 nm, one-dimensional Bragg peaks, reflecting the presence of one-dimensionally ordered ice, appeared around Q~22 nm^{-1} at lower temperatures, as shown in **Fig. 4.16** in Chapter 4. In the present experiments, however, there is no evidence for such an ordered structure. Although sharp Bragg peaks were also observed on the diffraction patterns in **Figs. 5.1(a)** and **(b)** below T_{WDT} ~220 K, they are attributed to bulk ice Ih formed outside the SWCNTs during wet to dry phenomenon, as discussed later.

As already mentioned in **Fig. 4.11** in Chapter 4, increasing temperature after quench results in the (10) intensity increasing from around 160 K and then decreasing at around 210 K. These behaviours correspond to the ejection and re-adsorption of water, respectively. Because the confined water at low temperature is non-crystalline as shown above, the recovery of the kinetics around 160 K can be attributed to a transition from a glass-like state to a liquid like state, i.e. a glass transition.

Next, the empty SWCNT patterns measured at 325 K were subtracted from those of the observed patterns because the observed ones are sums of the contributions from the carbon-carbon correlation, the SWCNTs-water correlation, and the water-water correlation. The results are shown in the right panels of **Figs. 5.1(a)** and **(b)**. WDD patterns for the bulk water reported in a previous literature[147] are also shown as dashed lines in **Fig. 5.1(b)**. It is apparent that the patterns at higher temperatures, e.g. at 271 K, are very similar to that of bulk water with a locally high density liquid (HDL) structure. However, at lower temperatures, e.g. 113 K, they become closer to

that of low density amorphous (LDA) ice. The results strongly suggest a transformation between HDL- and LDA-like water with temperature.

The information regarding the detailed temperature dependence of the WDD peak position around Q=18 nm^{-1} is summarized in upper panels of **Figs. 5.2(a)** and **(b)**. We found that the WDD peak positions exhibit a steep change at around 220 K, suggesting a 'liquid-liquid transition' (LLT) between HDL- and LDL-like states. Here, the low temperature state was presumed to be LDL rather than LDA because the confined water is mobile above 160 K.

The inset in the right panel in **Fig. 5.1(a)** shows the comparison of the WDD profiles taken at 244 K and 154 K. It can be found that there is an isosbestic point at Q=~18.4 nm^{-1}. Actually, the presence of such a point is expected for a first order phase transition. In the present case, the WDD profiles in the temperature range between 244 K and 154 K can be reconstructed by a linear combination of the profiles at 244 K and 154 K; the HDL-like component at 244 K decreases while the LDL-like component at 154 K increases with lowering temperature between 244 K and 154 K. This would be a strong evidence for an LLT of first order.

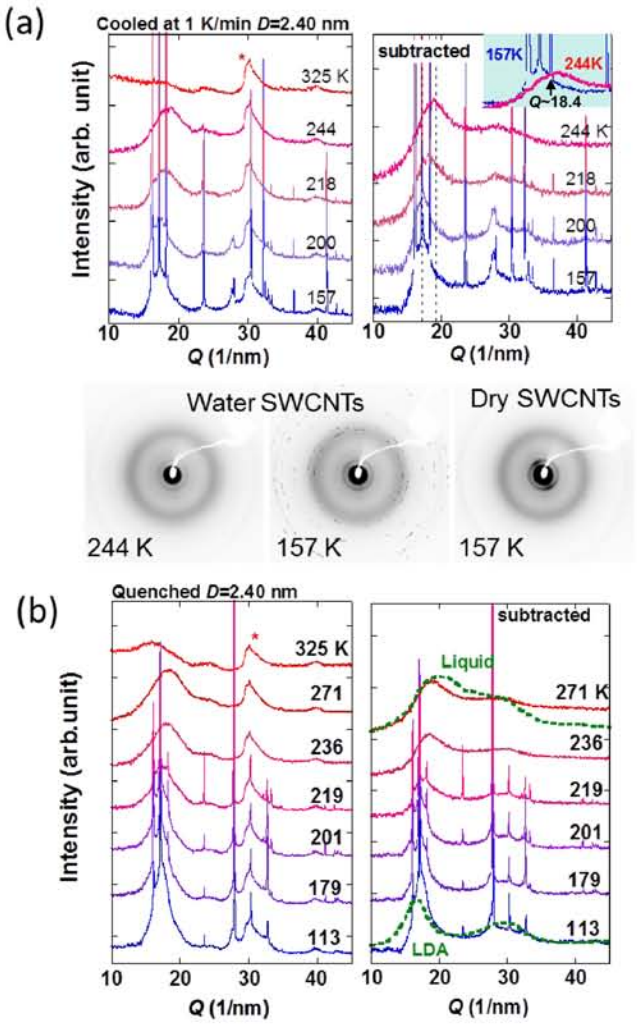

Figure 5.1. Observed XRD patterns of the water-SWCNT sample in the high Q range. (a) Examples of XRD patterns observed while decreasing temperature at a rate of 1 K/min. Inset: an expanded view around Q~18 nm^{-1}. Right figures show the patterns obtained by subtraction of the pattern at 325 K. X-ray diffraction two-dimensional images are also shown for the water-SWCNT system, and for the dry SWCNT sample. Temperature sequence is the same in both measurements. White parts are shadows of a stopper for the direct incident X-ray beam. (b) Examples of XRD patterns measured with increasing temperature after quenching to 110 K from room temperature. In the right panel, the patterns of bulk water at room temperature and low density amorphous (LDA) water in ref. 147 are shown for comparison. The patterns are shifted vertically for clarity. Diffraction peaks with asterisks are due to the honeycomb structure of the SWCNTs.

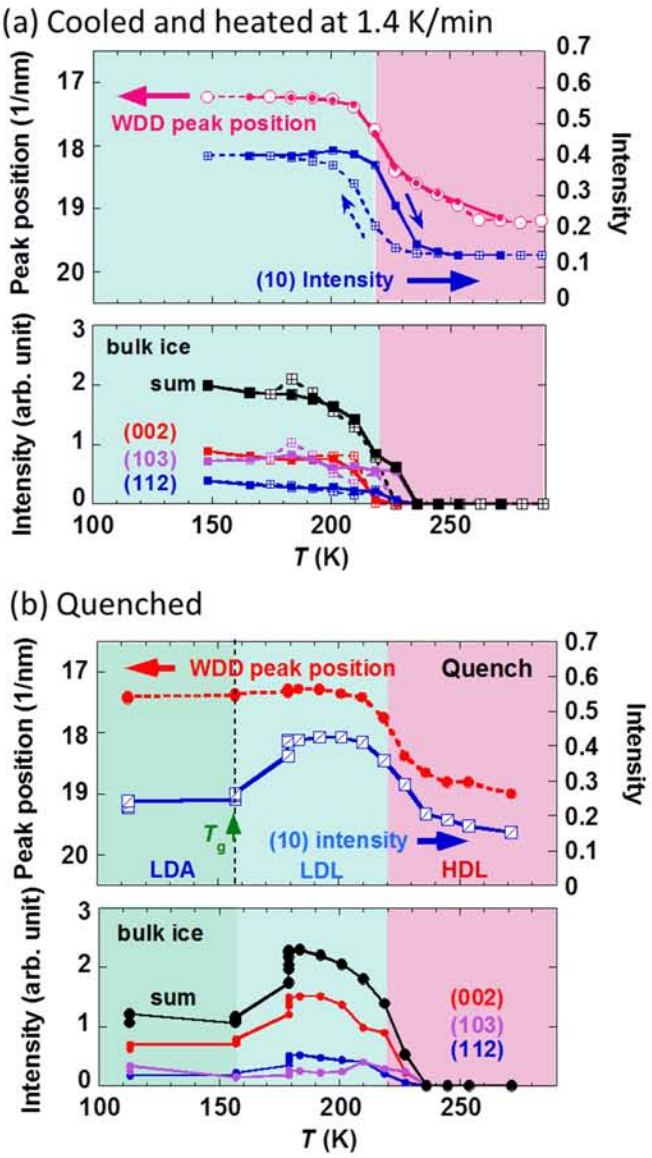

Figure 5.2. Temperature dependence of the (10) intensity, WDD peak position, and peak intensity of the bulk ice Ih. (a) Measured with decreasing and increasing temperature at a rate of 1.4 K/min as shown by dashed and solid lines, respectively. (b) Measured after quenching to 110 K from room temperature. At 157 K and 179 K, the temperature was held for 70 min and 120 min, respectively. In the lower panels of (a) and (b), the intensity of the (002), (103) and (112) peaks of the bulk ice Ih and their sums are plotted. Lines are for clarity.

5.1.2. MD Calculations for Water-SWCNT Systems

Further analysis on the atomic level was obtained through MD simulations for SWCNTs with diameters between 2.03 and 4.07 nm. An example of snapshot structures for the confined water inside the SWCNT of diameter 2.03 nm is shown in **Fig. 5.3**. It indicates that the confined water does not crystallize at low temperature. Using atomic coordinates of the water molecules obtained by the MD simulations, fraction of water molecules with four coordination was calculated. Here, the four-coordinated water molecules were defined as those having four oxygen-oxygen coordination within 0.33 nm. The results are in **Fig. 5.4(a)**. It shows the continuous development of hydrogen-bond networks with decreasing temperature. At the same time, the rotational correlation time τ of water molecules calculated by the MD results exhibits non-Arrhenius temperature dependence as shown in **Fig. 5.4(b)**. This behaviour in τ reflects the development of hydrogen-bond networks. These simulation results should be strongly correlated to the gradual variation in the WDD peak position above 230 K observed in the XRD experiments.

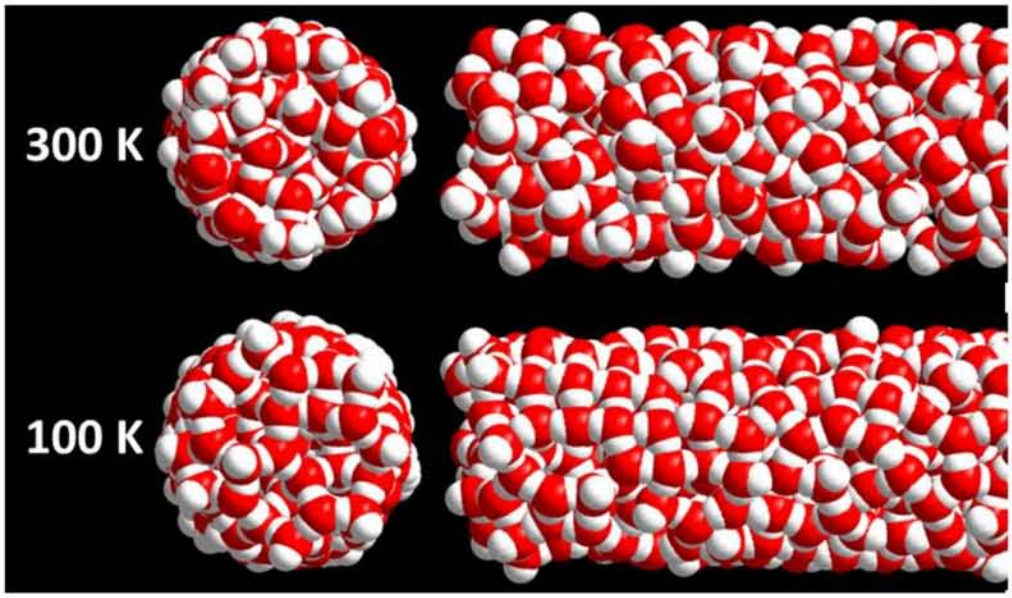

Figure 5.3. Snapshot structures of water confined in an SWCNT of diameter 2.03 nm at 300 K and 100 K. The SWCNT is not shown for clarity. Left: top views. Right: side views.

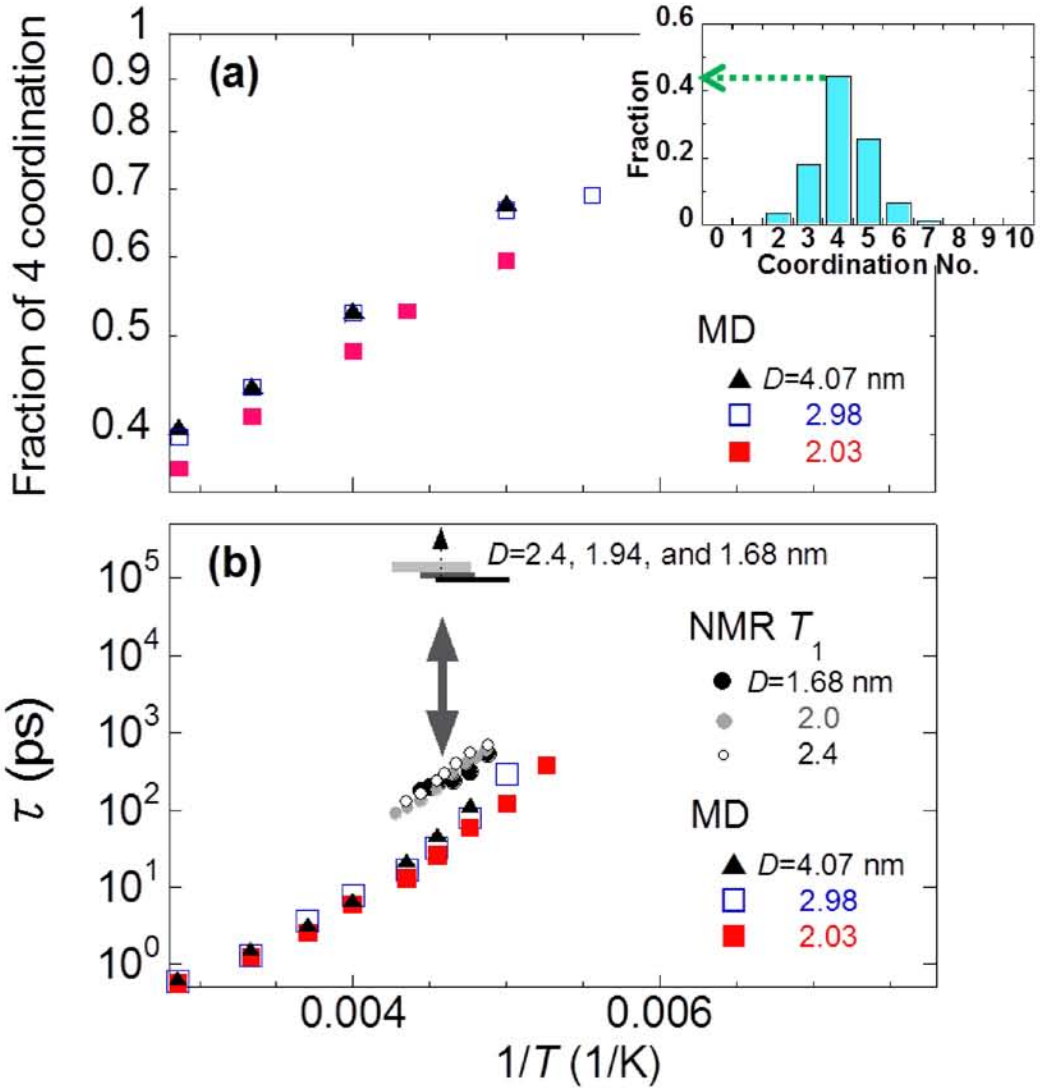

Figure 5.4. Fraction of four-coordinated water molecules, and rotational correlation time τ for the confined water. D is the SWCNT diameter. (a) was obtained from the MD simulations. The inset in (a) is an example of the distribution of the coordination number. In the inset figure, an arrow denotes the fraction of four-coordinated water molecules. In (b), triangles and squares are τ obtained from MD calculations using the SPC/E water model (ref. 134). The horizontal lines were estimated from a motional narrowing condition of ^{2}D-NMR using the NMR data in **Fig. 4.5** in Chapter 4. Circles were obtained from ^{2}D-NMR spin-lattice relaxation time T_1. Coexistence of the fast and slow dynamics suggests that the LLT is of the first order.

5.1.3. NMR Measurements for Water-SWCNT Systems

We also obtained τ from an NMR line broadening taking place in the range of 190-235 K and spin-lattice relaxation time T_1, as shown by horizontal lines and circles in **Fig. 5.4(b)**, respectively. The horizontal lines were estimated from a motional narrowing condition of ^{2}D-NMR using the NMR data in **Fig. 4.5** in Chapter 4. Thus the horizontal lines in **Fig. 5.4(b)** specify the regions where the NMR-signal intensity starts reducing and reduces to half due to slowing down of molecular rotations. Above 230 K, τ obtained by the NMR data and the MD calculations shows similar temperature dependence, but clearly deviates at around 190-235 K, indicating the occurrence of a transition. It should be noted that the observed sudden change cannot be fully ascribed to freezing of the ejected water from the inside of SWCNTs. This notion is based on the XRD observation in which the substantial amount of water (more than 50% of that at room temperature) remains inside SWCNTs even below the WDT (see Section 4.1.4. in Chapter 4). Thus the transition, which is assigned to an LLT, must take place in the confined water. Furthermore, the observed jump of τ and the coexistence of slow and fast dynamics (overlapping regions between the horizontal lines and circles in **Fig. 5.4(b)**) strongly suggest that the LLT is of the first order.

5.1.4. Additional Evidence for the Wet-dry Transition

We now shift our attention back to **Figs. 5.1(a)** and **(b)**. In both cases, sharp Bragg peaks attributable to bulk ice Ih[149] were observed below T_{WDT} ~220 K. The intensity of the (002), (103) and (112) peaks of the ice Ih and their sums are plotted in the lower panels of **Figs. 5.2(a)** and **(b)**. The (10) peak intensity of the sample, re-plotted from **Fig. 4.11**, is also shown in upper panels in **Figs. 5.2(a)** and **(b)**. From the figures, it is found that the Ih peak intensity rapidly changes almost concomitantly with the (10) intensity. Therefore, the observed ice Ih can be considered to be the water ejected from the inside of the SWCNTs through the WD process. For comparison we carried out an experiment on a dry SWCNT sample using the same instrumental set up and temperature sequence as those for the wet sample. Lowers in **Fig. 5.1(a)** show the two-dimensional X-ray diffraction images obtained. As seen in the images, the diffraction of ice Ih, indicated by spots in the image, appears only in the wet sample below T_{WDT}.

5.1.5. The Liquid-liquid Transition as a Driving Force for the Wet-dry Transition

Comparing the temperature dependence of the WDD peak position with that of the (10) peak intensity as shown in **Figs. 5.2(a)** and **(b)**, another important aspect is revealed; the changes occur in the same temperature domain, suggesting that the LLT and the WDT take place concomitantly with each other. This can be understood by considering the LLT as the driving force for the WDT. Actually, an experimental report on a binary

liquid mixture in which one liquid has an LLT[150] proposed that the miscibility of the liquid mixture changes at the LLT, inducing demixing (or mixing) of the liquids. Thus, we can similarly expect that the affinity of water to SWCNTs is much lower in the LDL like state than in the HDL like state, resulting in the drying of the LDL to avoid the energetically-unfavourable condition. The origin of the low affinity in the LDL like state is likely related to its developed hydrogen-bond network structures.

5.1.6. Connection to the Liquid-liquid Critical Point Scenario in Bulk Water

XRD experiments were also carried out on different diameter (D) SWCNTs. **Figure 5.5** indicates the liquid-liquid transition temperature T_{LLT} as a function of $1/(D\text{-}D_0)$. Here, D_0 is set to be 0.95 nm where four-coordinated water is difficult to exist due to the strong confinement. Assuming that the effect of nano-confinement on water structure is equivalent to the application of pressure as in solute addition[19], **Fig. 5.5** would describe a phase variation of water in a temperature-pressure plane. Since we obtained the evidence that the LLT of the confined water is of the first order, the results would be compatible with the liquid-liquid critical point (LLCP) scenario rather than the singularity-free (SF) scenario for bulk water (see Section 2.1.5. in Chapter 2). In **Fig. 5.5**, we find that T_{LLT} decreases with increasing "pressure" and a critical point proposed by Mishima (~223 K and ~50 MPa)[21] can be on an extrapolation line to zero-pressure.

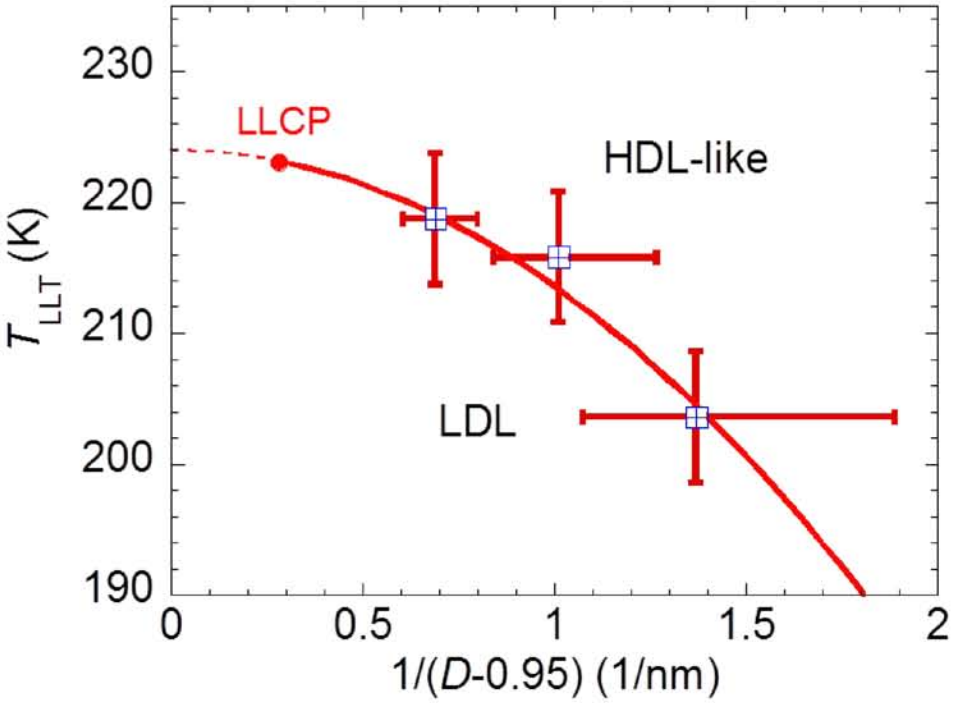

Figure 5.5. Liquid-liquid transition temperature T_{LLT} of the confined water as a function of SWCNT diameter D. T_{LLT} is defined as the midpoint of the steep change in temperature dependence of the WDD peak position. Error bars in the horizontal axis indicate the distribution width of D in each sample. Solid and dashed lines are given by a formula $T_{LLT}= T_0\text{-}A/(D\text{-}D_0)^2$ with T_0=224 K, and A=10.4 K for a guide to the eye, which is obtained by a least-square fit using a fixed D_0=0.95 nm. A critical temperature of ~223 K shown by "LLCP" was proposed by Mishima (ref. 21).

5.2. Summary

Taken together, our findings and the related phenomena reported so far argue strongly for the first order LLT between HDL and LDL taking place inside SWCNTs. The results would lead to validity of the LLCP scenario for bulk water. Besides, the present findings are likely to have an important influence on water crystal growth in naturally occurring biological[151, 152] and mineralogical materials[65, 66] with nano-porous structures.

Chapter 6
Amorphous Water in Three-dimensional Confinement of ZTC

6.1. Results and Discussion

6.1.1. XRD of Water-ZTC Systems

Fig. 6.1(a) shows the observed powder XRD patterns in wet and dry ZTC samples at 289 K. Two sharp Bragg peaks around Q = 4.56 and 7.43 nm^{-1} were assigned to the (111) and (220) peaks in a cubic lattice with a periodicity of the parent zeolite Y.[24] The lattice constant was estimated to be 2.38 nm for the dry sample at RT. Its thermal expansion coefficient was 4.7±0.2 ppm/K in a T-range of 113 K and 300 K, which is slightly smaller than 7.5±2.5 ppm/K for the intertubule lattice constant with a van der Waals gap in SWCNT bundles and much larger than for the SWCNT diameter composed of strong sp^2 covalent bonds.[153] This suggests a rather softness of the ZTC lattice.

The (111) peak intensity drastically decreased upon exposure to saturated water vapor at RT as shown in **Fig. 6.1(a)**. A comparison with calculated XRD patterns based on MD simulations indicated that the decrease in the (111) peak was derived from water adsorption in the ZTC pores [inset in **Fig. 6.1(a)**]. Upon heating above 325 K, the peak intensity recovered due to water desorption. This water desorption-adsorption

behavior was reversible with hysteresis within 10 K. The amount of water adsorbed in the ZTC, estimated from a comparison of simulated and observed XRD patterns, was roughly 140 weight percent with respect to the dry ZTC (i. e. 140 wt%). This is consistent with values determined from other methods; 127 wt% at 298 K and 187 wt% at 288 K from the adsorption isotherm, 120 wt% from DSC, 140 wt% from weight uptake, and 150 wt% from NMR. These values are unusually large compared to those for other nano-porous carbons; 15-58 wt% in bundles of opened SWCNTs with diameters between 1.2 and 2.4 nm,[25-27] and 70 wt% in activated carbon fibers (ACFs) with micro-pores.[154] If we use the reported pore volume of 1.71 cm^3/g, [24] the local water density inside the ZTC pore is estimated to be 0.74-1.10 g/cm^3, comparable to that of bulk water under ambient conditions. This is equivalent to the water uptake of 0.52-0.74 g/cm^3 for a unit volume of the ZTC crystal. (Here, the ideal density of 0.435 g/cm^3 for the ZTC crystal was used.) The sponge-like structure of the ZTC crystal should be responsible for such large water adsorption amount. Although SWCNTs filled with water can be emptied with lowering temperature,[27] in the present case, the ZTC held water at least down to 113 K, as evidenced by the T-dependence of the (111) peak intensity in the XRD patterns.

Figure 6.1(b) shows the T-dependence of the XRD patterns for the wet sample. Sharp Bragg peaks above Q~15 nm^{-1} appeared below 273 K are due to the bulk crystalline ice, which forms outside the quartz capillary with ZTC powder, as well as excess water inside the capillary. Apart from these extrinsic peaks, broad diffraction peaks were observed around Q ~19 and 30

nm^{-1}. Since these were not present in the dry ZTC [see the top pattern in **Fig. 6.1(b)**], they can be ascribed to water diffuse diffraction (WDD).[148] With decreasing T, the WDD peaks shifted slightly to the lower Q side and became almost constant below 160 K, as shown in the inset in **Fig. 6.1(b)**. In addition no evidence for the presence of any crystalline ice inside ZTC was obtained down to 113 K, unlike water inside SWCNTs.[25, 26] These features are reminiscent of the T^1-dependence of volume in a glass former[75] wherein the thermal expansion coefficient changes steeply at a glass transition temperature T_g. Therefore, it is suggested that the glass transition of the confined water in ZTC, if exist, is around 150-170 K. A detailed discussion is given in Section **6.1.5**.

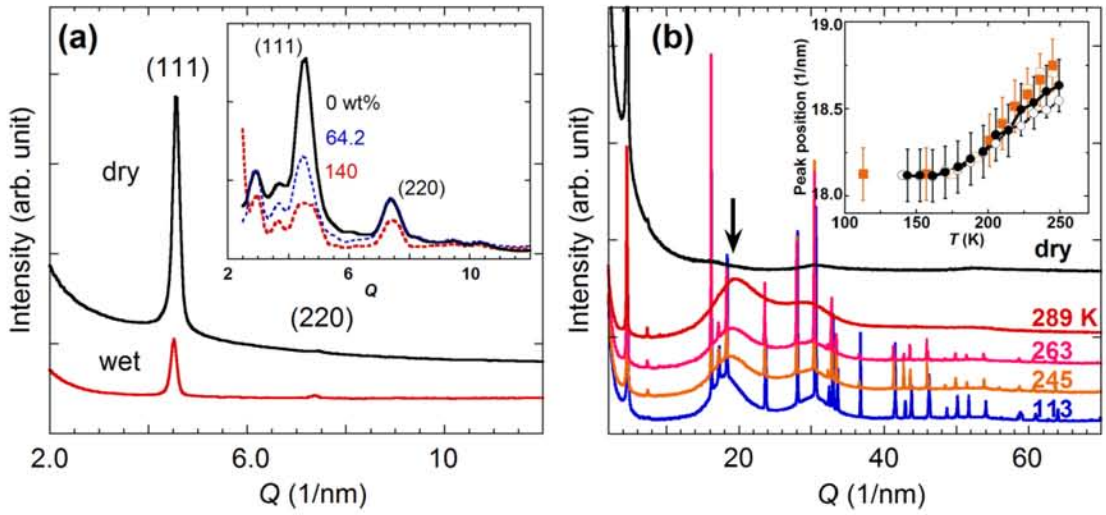

Fig. 6.1. Observed and calculated XRD patterns in dry and wet ZTC samples. (a) The observed XRD patterns of the dry and wet ZTC samples in a low Q range at 289 K. The inset shows calculated patterns for water contents of 0, 64 and 140 wt% as indicated. To reproduce the observed XRD patterns, an orientational randomness of the ZTC unit cell was introduced. The XRD patterns were calculated from the atomic coordinates using an XRD simulation tool in Materials studio ver. 4.1 (Accelrys Co.). (b) Observed XRD patterns of the wet sample at several temperatures in a wider Q range. The top pattern is for the dry ZTC sample for comparison. Sharp Bragg peaks above Q~15 nm^{-1} below 273 K are due to bulk crystalline ice. Inset: T-dependence of the WDD peak position indicated by an arrow. The open (closed) symbols were taken for decreasing (increasing) T. Two samples (denoted by circles and squares) were measured.

6.1.2. Isobaric Specific Heat C_p of the Confined Water

DSC scans were performed on the ZTC powder sealed with light water in a DSC cell. The results indicated that the exothermic (endothermic) peaks due to freezing (melting) of the bulk water completely disappeared below a water content of about 120 wt%, as expected. This implies that the confined water in ZTC has different properties than the bulk water. In addition, small exothermic (endothermic) peaks, whose intensity corresponded to a few % of the total amount of confined water (depending on the water content and sample history), were also observed around 220 K with decreasing T and around 260 K with increasing T, respectively. This might be due to freezing (melting) of water in the vicinity of the ZTC crystal surface.

Figure 6.2(a) shows C_p of the confined water and the dry ZTC at ambient pressure. The reliability in the C_p determination was checked by the measurements for two reference samples, bulk water and graphite powder (purity >99.99 %). C_p of the dry ZTC was slightly larger than that of graphite. This may be due to contribution from hydrogen atoms attached to the ZTC frame and the softness of ZTC lattice as suggested by the thermal expansion data.

Importantly, as shown in **Fig. 6.2(a)**, the C_p of the confined water decreased steeply below T_W~230 K from a nearly constant value of ~4.2 J/gK above T_W with lowering temperature. This anomaly is probably related with a FSC (or LLC), as details are discussed in Section 6.1.6..

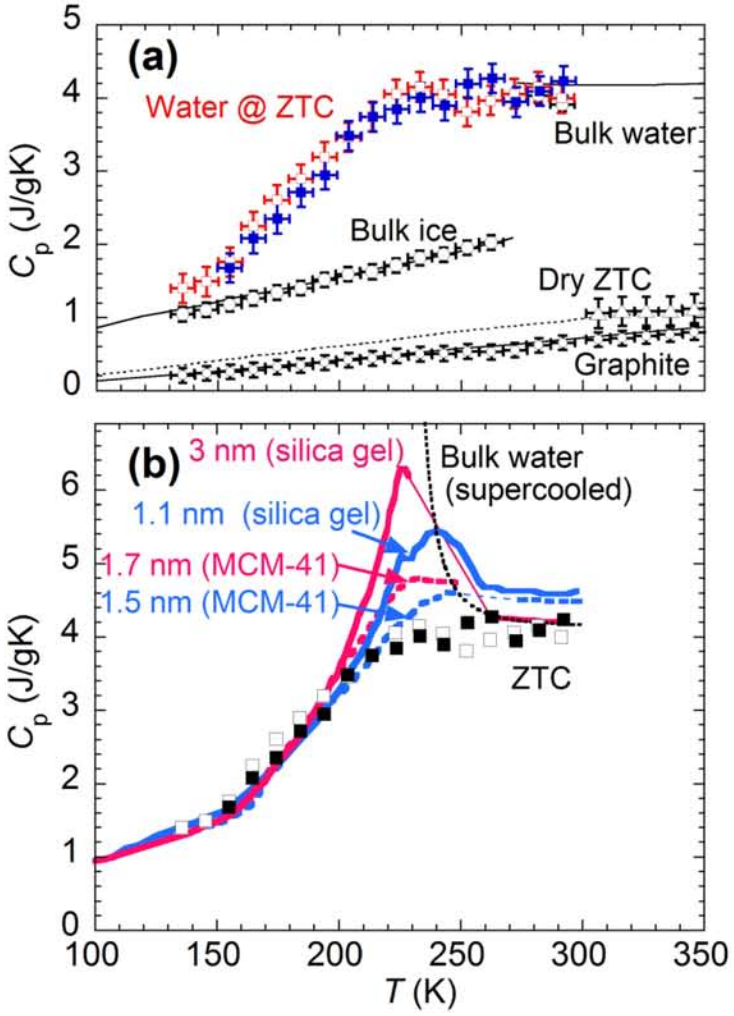

Fig. 6.2. T-dependence of the isobaric specific heat C_p. (a) Specific heat of confined water in ZTC, bulk water, dry ZTC, and graphite at 0.1 MPa. The DSC up (down) scan measurements shown by open (closed) symbols were performed in a stepwise manner, in which the samples were heated (cooled down) by 10 K at 5 K/min, and then held for 3 min to measure the baseline. Solid lines are those in literatures for the bulk water and graphite.[155, 156] The dashed line for dry ZTC is the data reported for graphite, scaled by 0.76 with respect to T as a reference. (b) Specific heat of confined water reported for silica gel by Maruyama *et al.*[12] and Oguni *et al.*[16], and MCM-41 by Oguni *et al.*[17] along with those in ZTC. The solid lines are for silica-gel and dashed lines for MCM-41. The pore diameters are given in the figure. Thin lines are interpolated for clarity. C_p of supercooled bulk water is also shown by dotted line.[157] The ZTC data in (b) is the same as in (a) except for the error bars.

6.1.3. Dynamics of the Confined Water from NMR

We now discuss the molecular dynamics investigated by NMR of deuteron and proton nucleus, ^{2}D and ^{1}H, in heavy and light water confined in ZTC. Examples of NMR spectra for ^{2}D and ^{1}H nuclei are shown in **Figs. 6.3(a)** and **(b)**, respectively. The observed spectra above 200 K were roughly determined by the field inhomogeneity of the applied magnetic field of 2-4 ppm over the sample volume, and much sharper than $f_0 \approx 200$ kHz for ^{2}D and 40 kHz for ^{1}H in the static limit. These are direct evidence for fast rotational and translational motion of water molecules in ZTC crystals. (This effect is known as motional narrowing of the NMR line width.[130]) From the narrowed ^{2}D-NMR spectra, the rotational correlation time τ_{rot} was estimated to be on the order of 1×10^4 ps at 200 K, using a narrowing condition; $\Delta f \approx f_0 \cdot (2\pi f_0 \tau)$, where $\Delta f \approx 1$ kHz is the width observed experimentally at 200 K.

In contrast to ^{2}D-NMR in which the intra-molecular quadrupolar interaction dominates the spectral width, in the case of light water, both the inter- and intra-molecular dipolar interactions among ^{1}H nuclei comparably contribute to the ^{1}H-NMR broadening (about 10 kHz from the inter-molecular interactions). Therefore, the narrowed ^{1}H-NMR spectra are a clear evidence for the fast translational motion of water molecules above 200 K, as well as rotational motion. This is consistent with the value for the self-diffusion coefficient of water obtained from MD simulations of $D \approx 3.4\times10^{-6}$ nm^2/ps at 200 K. The intensity of the narrowed NMR signal as

a function of T (see the inset in **Fig. 6.3**) indicates a mobile water content of 150±20 wt% above 220 K.

The inset in **Fig. 6.4** shows the T-dependence of the ^{2}D-NMR spin-lattice relaxation time T_1. The observed strong T-dependence with a minimum around 205 K is typical of the Bloembergen-Purcell-Pound (BPP) relaxation mechanism,[130] in which T_1 is related to the rotational correlation time τ_{rot} in the present case. The T_1 in the entire T-region measured could be fitted with a Vogel-Fulcher-Tammann (VFT) form which is often used for a fragile liquid; $\tau_{\mathrm{rot}} = \tau_0 \exp\left[A/(T - T_0)\right]$, where τ_0, A, and T_0 are constants.[75] The best result is given by a solid line in the inset in **Fig. 6.4**. The obtained parameters are; $\tau_0 = 1.03 \times 10^{-14}$ s, $A = 1236$ K, and $T_0 = 109$ K. On the other hand, if we use the Arrhenius fit expected for a strong liquid, $\tau_{\mathrm{rot}} = \tau_0 \exp(A/T)$, the best fit was obtained for $\tau_0 = 4.65 \times 10^{-20}$ s and $A = 5179$ K (the dotted line in the inset in **Fig. 6.4**). In this case, however, it slightly deviates above 240 K. More importantly, the obtained τ_0, which is τ at infinite temperature, is unphysical because the value is much shorter than the typical time scale of molecular vibrations of 10^{-14} s.

The rotational correlation time was also obtained from the MD simulations. The results are included in **Fig. 6.4**, in addition to the T-dependence of the self-diffusion coefficient D. Although the values are about a third of those from the NMR experiments, the T-dependence was well described by the VFT form with the same $T_0 = 109$ K above 200 K.

The rotational correlation time for bulk water, obtained from the T_1 of ^{2}D-NMR, is also shown in **Fig. 6.4**.[158] Here we find clear difference between the T-dependences of the bulk water and the present confined system. At higher temperatures, interestingly, τ is longer in the present confined water than in the bulk water, similar to the cases in porous glass.[159] Besides, the T-dependence is much weaker in the confined water than in the bulk water,[158, 159] which exhibits a singularity behavior described by a formula such as a power law $\tau \propto (T - T_0)^{\gamma}$ with $T_0 \sim 230\,\mathrm{K}$ and $\gamma \sim -2$. The differences would arise from the nanoconfinement effect: although the cooperative behaviors develop with lowering T in both the systems, the size of the cooperative region in the confined water could be limited by the system size or its development is hampered by the three dimensional ZTC wall in the present case.

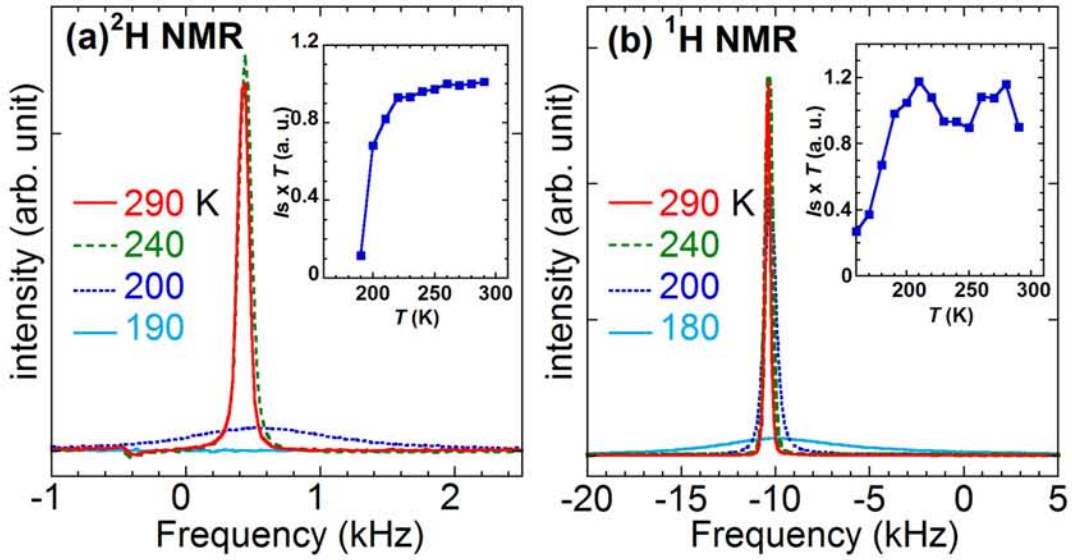

Fig. 6.3. T_1-dependence of NMR spectra for the confined water. (a) ^{2}D-NMR of heavy water. (b) ^{1}H-NMR of light water. The water content is 16 mg for both, corresponding to 96 wt%. Insets show T_1-dependences of the integrated NMR intensity multiplied by T.

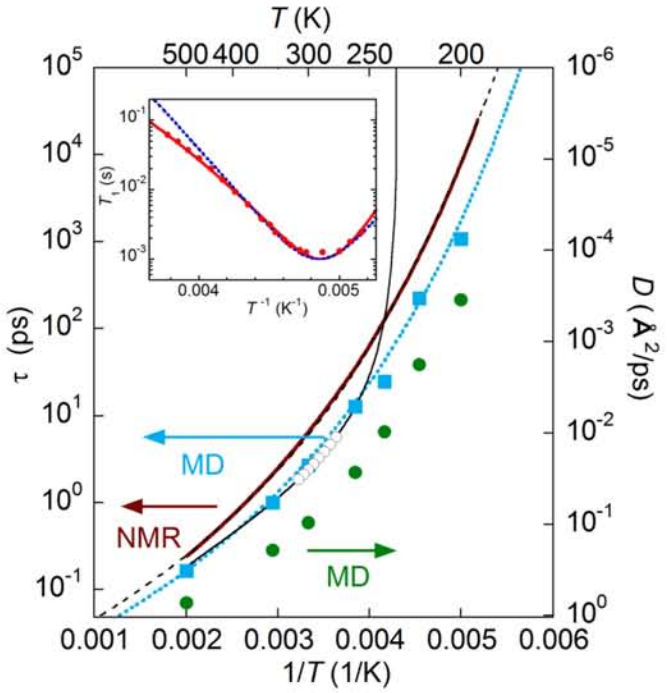

Fig. 6.4. Arrhenius plots of the rotational correlation time, τ_{rot}, of water in ZTC. The thick solid line is obtained by fitting the ^{2}D-NMR spin-lattice relaxation time T_1 assuming a VFT form, while the thin dashed line was obtained from a two component fit of VFT and Arrhenius forms (see text). Squares are τ_{rot} obtained from MD simulations for 3112 water molecules in ZTC, along with a VFT fit shown by the dotted line. Closed circles are self-diffusion coefficients obtained from the MD simulations. Open circles are literature data for bulk water obtained by the ^{2}D-NMR T_1.[158] The thin solid line is a power-low $\tau \propto (T - T_0)^{\gamma}$ fitted to the experimental data (see text) with $T_0 = 232$ K and $\gamma = -1.88$. The inset in the upper-left shows the T-dependence of ^{2}D-T_1. T_1 is well reproduced by using a VFT formula for the T-dependence of τ (shown by a solid line) rather than an Arrhenius type (shown by a dotted line).

6.1.4. MD Simulations for the Confined Water

To obtain the microscopic structure and dynamics, we performed the MD simulations. The results for simulation I with 600 water molecules (equivalent to 38.2 wt%) are shown in **Fig 6.5**. The water molecules were described by the SPC/E water model.[134] The system temperature was held at 300 K for 2 ns and then lowered to 10 K at a cooling rate of 100 K/ns. First, it was shown that all of the water molecules were adsorbed inside the ZTC within the first 2 ns at 300 K, and retained inside the ZTC crystal stably down to 10 K. The snapshot structures of water clusters thus formed inside the ZTC at 300 K and 10 K, as shown in **Fig. 6.5**, indicate that hydrogen-bond networks develop in the water cluster with decreasing *T*. Similar results were obtained for TIP3P model[133] for water.

However, the structure of the water cluster is quite different from those of crystalline ice even at the lowest *T*. This is clearly demonstrated by analyzing the coordination number and bond angle for the oxygen (O) atoms in water. **Figure 6.6(a)** shows the results for the case of 1600 water molecules (equivalent to 102 wt%) in simulation I. Here, the water molecules within the O-O distance of 0.33 nm were taken into account. Essentially, the same distributions were obtained for the system of 3112 water molecules (equivalent to 198.3 wt%) in simulation II. At 300 K, interestingly, the distribution function of the O-O-O bond angle was very close to that for bulk liquid water at RT [shown by a solid line in **Fig. 6.6(a)**]. This result suggests a similarity in the structures of the confined water and the bulk water around RT. Note that the specific heat of the confined water inside ZTC,

4.2±0.2 J/gK, is equal to that of bulk water within experimental accuracy above 220 K.

At lower temperatures, the average coordination number was 4.12, slightly smaller than the value of 4.18 at RT. However, the distribution of the O-O-O angle became remarkably narrower. This narrowing implies growth of hydrogen bonds with more appropriate O-O-O angles. As a result, water molecules form an amorphous-like structure, roughly characterized by a strongly distorted hydrogen-bond network (as shown in **Fig. 6.5**). This is known as the continuous random network (CRN) model for an amorphous solid.[161] Furthermore, it can be found, from a comparison with the distributions for LDL and HDL [lower in **Fig. 6.6(a)**], that the low-T structures are closer to that of LDL rather than HDL.

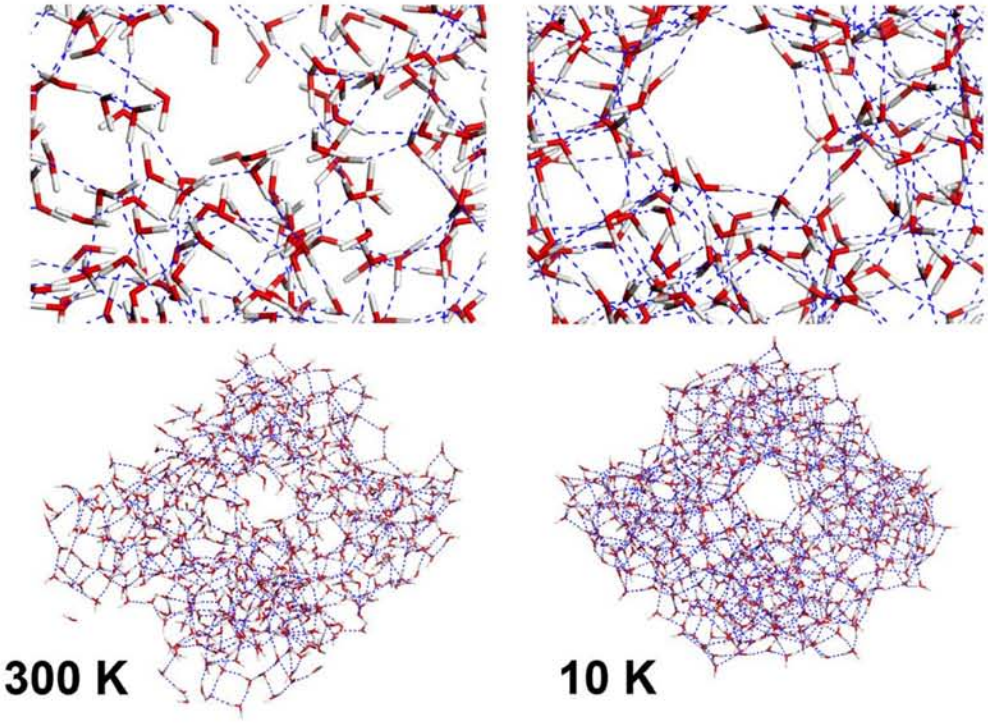

Fig. 6.5. Snapshot structures of the confined water obtained from the MD simulation I with 600 water molecules. Lower: structures of water clusters inside the ZTC crystal at 300 K and 10 K. Upper: expanded views. The ZTC is not displayed for clarity. Dashed lines represent hydrogen bonds in which the OH distance does not exceed 0.20 nm and the OHO angle is between 90 and 180 degrees.

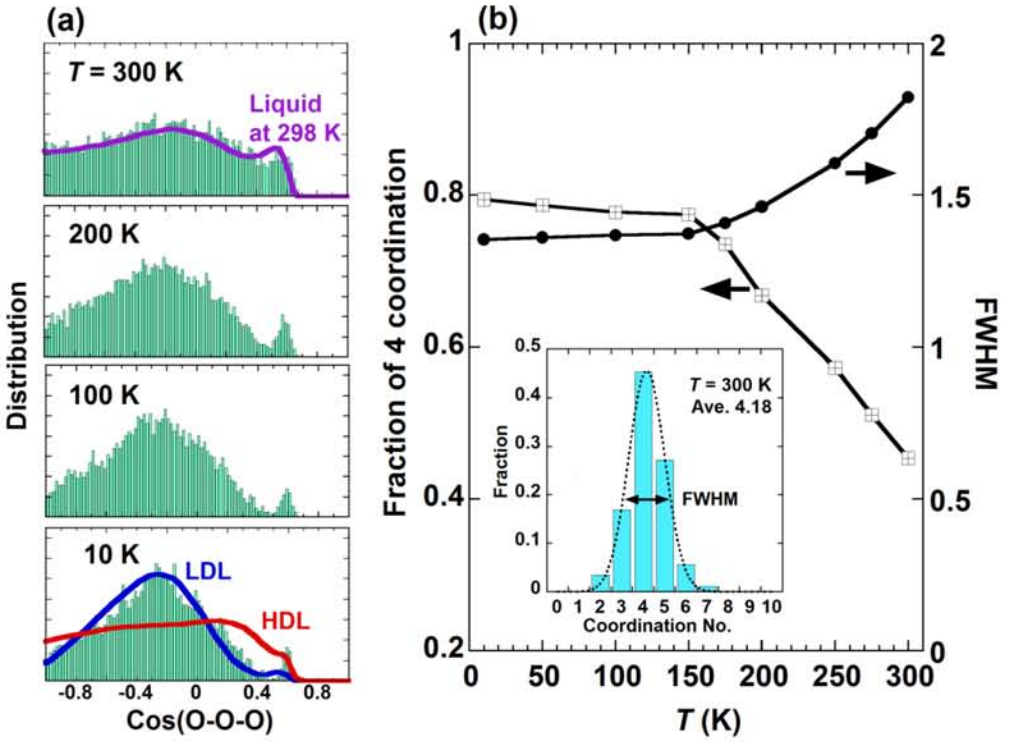

Fig. 6.6. Distribution of OOO bond angle (a) and distribution of coordination number (b) for the confined water in ZTC calculated from the results of MD simulations with 1600 water molecules. In (a), the thick solid lines represent the distribution obtained from computer simulations for bulk water at 298 K reported by Finney,[32] and bulk LDL and HDL reported by Soper.[160] The inset in (b) is an example of the distribution of the coordination number at 300 K that defines the distribution width as the full width at half maximum (FWHM).

6.1.5. Glass Transition of Water inside ZTC

We discuss here the possible glass transition of the present confined water based on the experimental and computational results because the liquid state freezes into a CRN amorphous solid at low temperatures. The T-dependence of the WDD peak position in **Fig. 6.1** suggests a similar behavior to the glass transition around 150-170 K within the experimental time scale and accuracy, as already mentioned. Correspondingly, the MD simulations, shown in **Fig. 6.6(b)**, indicate that the number of hydrogen bond ceases its T-dependence below around 150 K, in consistent with the XRD experiments. More specifically, a generally accepted criterion for the glass transition temperature T_g can be applied to the present case; at T_g the dynamic timescale, such as τ_{rot}, reaches around 100 s (although depending on the observation time scale). Then we obtained T_g=143 K and 139 K in the present system from the extrapolations of τ_{rot} to 100 s in the NMR and the MD data above 200 K available from the present study, respectively. Therefore, all the data suggest that the T_g of the confined water in ZTC should be around 150 K.

Furthermore, a glass transition of confined water is often accompanied by a "very feeble jump" in C_p, although molecular glass formers usually exhibit a substantial jump.[9, 76] Because the present measurement did not have enough sensibility to detect such a small C_p jump, here the observed C_p was compared with those of nano-confined waters in silica gel[12, 16] and MCM-41[17] as shown in **Fig. 6.2(b)**. It is found that the T-dependences of C_p

are very similar to each other except the peak structures around 230 K. In some of these confined waters[17], the T_g was actually identified as around 150 K by observing a clear relaxation behavior for typical glass transition which was accompanied by a small jump in C_p by about 0.2 J/gK. If we expect a similar jump with the comparable magnitude in these confined systems at T_g, the present ZTC system should be reasonably presumed to have a T_g of 140-150 K, in consistent with the results of the XRD, NMR, and MD simulations mentioned above.

6.1.6. Effect of Nano-confinement on Liquid-liquid Crossover or Fragile-strong Crossover

As already mentioned, the T-dependence of C_p resembles each other for the confined waters in silica gel, MCM-41, and the present ZTC system [**Figs. 6.2(a) and (b)**]. However, the peak around 230 K, which would be the sharpest in bulk water[48, 157] as shown by a dotted line in **Fig. 6.2(b)**, seems to decrease as the pore diameter decreases for each set of data in silica gel and MCM-41. In the case of ZTC, although the peak was almost smeared out, the anomalous drop was still clearly observed below 230 K. The peak in C_p is sometimes taken as the locus of the Widom line or evidence for LLC, wherein a dynamic crossover such as FSC should be observed.[3, 9, 48, 76] Then, if the peak height decreases depending on the distance from "the second critical point" in the positive T-P region, the present nanoconfinement might be considered to work as a negative pressure by modifying (and expanding) the hydrogen bond network,[162] as well as the cut-off on correlation length for

fluctuation. In this point of view, a high pressure study is important, and now in progress.

However, as discussed for the NMR data, the T-dependence of τ_{rot} was well described by the VFT form, which indicates the confined water is a fragile liquid down to 200 K. This seems to contradict the above discussion. Why was the dynamic crossover not observed in the NMR data? Thus, we performed another (but also tentative) analysis, wherein the confined water is composed of two dynamically mixed components having different rotational correlation times; $\tau_{\mathrm{H,rot}} = \tau_0 \exp[A/(T-T_0)]$, and $\tau_{\mathrm{L,rot}} = \tau_0 \exp[B/T]$, where τ_0, A, T_0 and B are constants. The τ_{rot} observed in NMR is assumed to be given by $1/\tau_{\mathrm{rot}} = f/\tau_{\mathrm{H,rot}} + (1-f)/\tau_{\mathrm{L,rot}}$, where f is unity at infinite T and zero at 0 K and describes the fraction of the component with $\tau_{\mathrm{H,rot}}$. It was found that the VFT form obtained above is well described by this model, indicating that the NMR results are not incompatible with the presence of LLC or FSC around 230 K. Although it was difficult to uniquely determine the parameters from the present data, the following set well approximated the obtained VFT parameters as indicated by the thin dashed line in **Fig. 6.4**; $\tau_0 = 1.2\times10^{-14}$ sec, $A = 1170$ K, $T_0 = 105$ K, $B = 5500$ K and $f = (1/\pi)\tan^{-1}[0.02(T-230)] + 0.5$. Here, f describes the crossover of the dominant phase around 230 K. Note that we obtain again a T_{g}~150 K from $\tau_{\mathrm{L,rot}} = 100$ s.

However, alternative explanations for the apparent absence of FSC or LLC in the NMR data might be possible. For example, while quasi-elastic neutron scattering experiments have observed FSC-like behavior,[13] some experiments, including NMR, dielectric spectroscopy and neutron spin-echo experiments, have observed no evidence for the FSC or LLC.[20, 77, 78, 163] This should be due to differences in spatial scale or/and dynamics (such as α and ß relaxations) to be observed, depending on the experimental techniques. In this point of view, the present study should be re-examined in the future.

6.2. Summary

It was found that the ZTC crystal with a sponge-like structure adsorbs an unusually large amount of water; water uptake per unit volume of the ZTC crystal amounts to 0.5-0.7 g/cm^3. This confined water is liquid like and highly mobile down to 200 K. Above 230 K, the isobaric specific heat C_p is nearly equal to 4.2 J/gK for the bulk water at RT. Upon lowering the temperature from 230 K, C_p steeply decreases and reaches the value for bulk ice around 150 K. The rotational correlation time τ_{rot} of the water molecules shows the apparent non-Arrhenius T-dependence (VFT form) with a singularity temperature of 109 K. By extrapolating the observed τ_{rot} to 100 s at lower temperatures, a glass transition temperature was estimated to be 143 K, in agreement with about 150 K expected from the XRD, and C_p measurements, and the MD simulation results. Although no clear evidence for dynamic crossover was observed, it was suggested that the confined water freezes into the low density liquid-like structures (or LDL and LDA water) from high

density liquid (HDL) like water at higher temperatures. Besides, the ZTC-water system, owing to its novel physical properties, may have potential applications such as high performance filtration membranes and heat exchange media which work even at low temperatures.

Chapter 7

Conclusion

In this thesis, we experimentally elucidated the detailed low temperature structures including two liquid states and the relating dynamic properties of the confined water inside the carbon nanomaterials.

Employing XRD experiments, NMR measurements, and MD simulations, we established a global T- D phase diagram of water confined in SWCNTs. It was found that the confined water in thick SWCNTs with D ranging from 1.6 to 2.4 nm exhibits a wet-dry transition (WDT), wherein the water is partially ejected from the inside of SWCNTs. For D ~1.4 nm, on the other hand, the filling with water substantially affects the low temperature structures; it was found that while hollow ice NTs form at a lower water content, further increase in the water content leads to filled structures, such as ice NTs containing a 1D water chain. Such dependence on the water content is caused by an edge effect of SWCNTs on the water structure.

As for the confined water in SWCNTs of D > 1.6 nm, the mechanism for the WDT and the structure of the confined water at low temperature were examined in detail. It was indicated by the XRD experiments that the confined water is in liquid (or glassy) state down to 110 K. The structure at 110 K is quite similar to LDA in the bulk, while at 289 K to bulk liquid water which has locally HDL-like structure. The conversion between these two states occurs at 200-220 K, depending on SWCNT diameters. Since the glass transition temperature of the confined water was estimated to be ~160 K in

the same experiments, the conversion at 200-220 K should be a transition between locally HDL-like liquid to LDL, namely, a 'liquid-liquid transition' (LLT). The analyses on the observed XRD profiles as well as the rotational correlation time of the confined water obtained by the NMR measurements strongly suggested that the LLT is of the first order.

Another important aspect is that the LLT and the WDT seem to take place concomitantly each other. This is naturally understood by considering that the LLT is the driving force for the WDT. It would be expected that the affinity of water with SWCNTs is much lower in LDL than in HDL, resulting in the drying of the LDL to avoid the energetically-unfavorable condition. The origin of the low affinity in LDL should be related to its developed hydrogen-bond network structures.

In addition, we examined the properties of confined water inside ZTC. It was found that isobaric specific heat of the confined water steeply decreased below ~230 K. This is considered as an anomaly related with a fragile-strong crossover (or liquid-liquid crossover).

Taken together, our findings strongly argue for the HDL–LDL conversion taking place inside SWCNTs or ZTC. Assuming that the nano-confinement is equivalent with application of pressure by breaking favorable hydrogen bonds as in solute addition, the confined water may be a mimic of bulk water under pressure. In this point of view, the present results support the existence of a first order LLT in the bulk water under pressure and the possible liquid-liquid critical point scenario.

Appendix

1. XRD Simulations for Cubic Ice Confined in SWCNTs

Cubic Ice (Ic) is a metastable form of ice in bulk, wherein the oxygen atoms are arranged in a diamond structure. In previous studies, it has been reported that water confined in MCM-41 with a diameter more than ~2 nm crystallizes into ice Ic at low temperature (see Section 2.2.2. in Chapter 2). Thus ice Ic may form inside thick SWCNTs at low temperatures. To examine this possibility, we calculated XRD patterns for confined ice Ic inside SWCNTs and compared them with the observed patterns.

The XRD pattern calculations were performed using the Debye formula. The simulated XRD pattern for an ice Ic crystal is shown in **Fig. A1.1**. In the simulation, the ice Ic crystal consisting of 125 unit cells (3.18 nm × 3.18 nm × 3.18 nm) was used. The cubic lattice parameter for the crystal was set to be 0.6355 nm. As shown in **Fig. A1.1**, the simulated pattern well reproduces the observed one for bulk ice Ic in a literature[147].

Next, we discuss XRD patterns for confined ice Ic inside an SWCNT of D=2.40 nm. In the simulation, the XRD patterns only contributed from the confined ice Ic were calculated, omitting contribution from the SWCNT. The simulated patterns are shown in **Fig. A1.2**. The length of the SWCNT and the crystal orientation of the confined ice Ic were taken as parameters. It was found from the simulation results that the width and relative intensities of the peaks slightly depend on the crystal orientation.

Figure A1.3 shows the comparison between the simulated pattern for

confined ice Ic and the observed pattern. Here, the observed pattern is the data taken for the water-SWCNT sample with D=2.40 nm at 113 K, while the simulated pattern is the sum of the three patterns shown in panel i) of **Fig. A1.2**, just as an example. The peaks at Q~28 and 32 nm^{-1}, if exist, in the observed pattern may reflect those of the simulated ice Ic. However, the amount of ice Ic must be small as shown in the green line in **Fig. A1.3**.

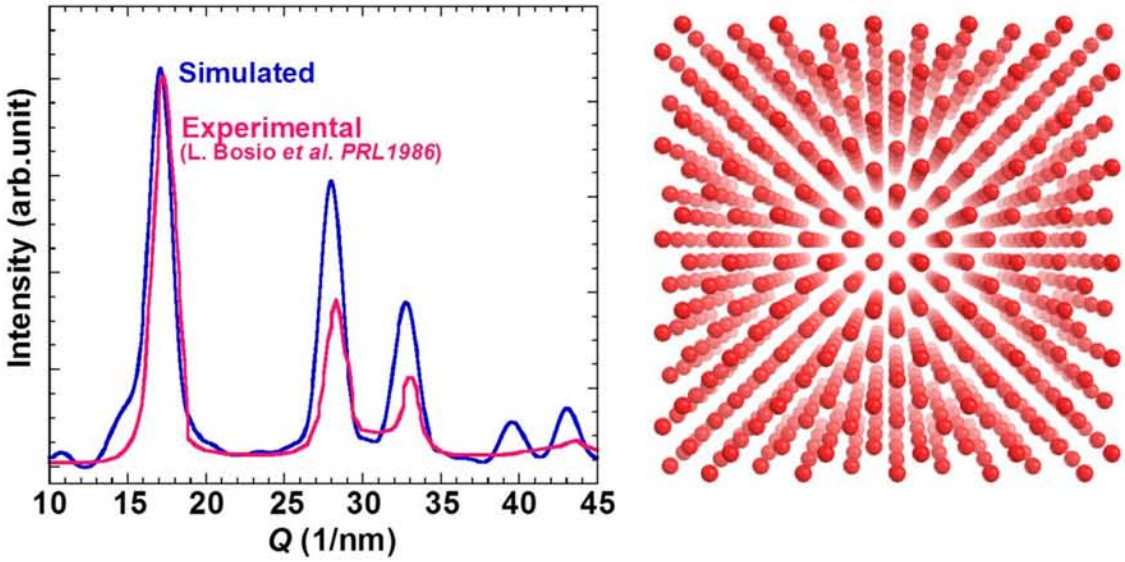

Fig. A1.1. Experimental and simulated XRD patterns for ice Ic. The simulated pattern was obtained for an ice Ic crystal consisting of 125 unit cells (3.18 nm × 3.18 nm × 3.18 nm). The right figure shows the structure of the ice Ic crystal used in the simulation. Only the oxygen atoms in water molecules are shown. The experimental pattern is from ref. 147.

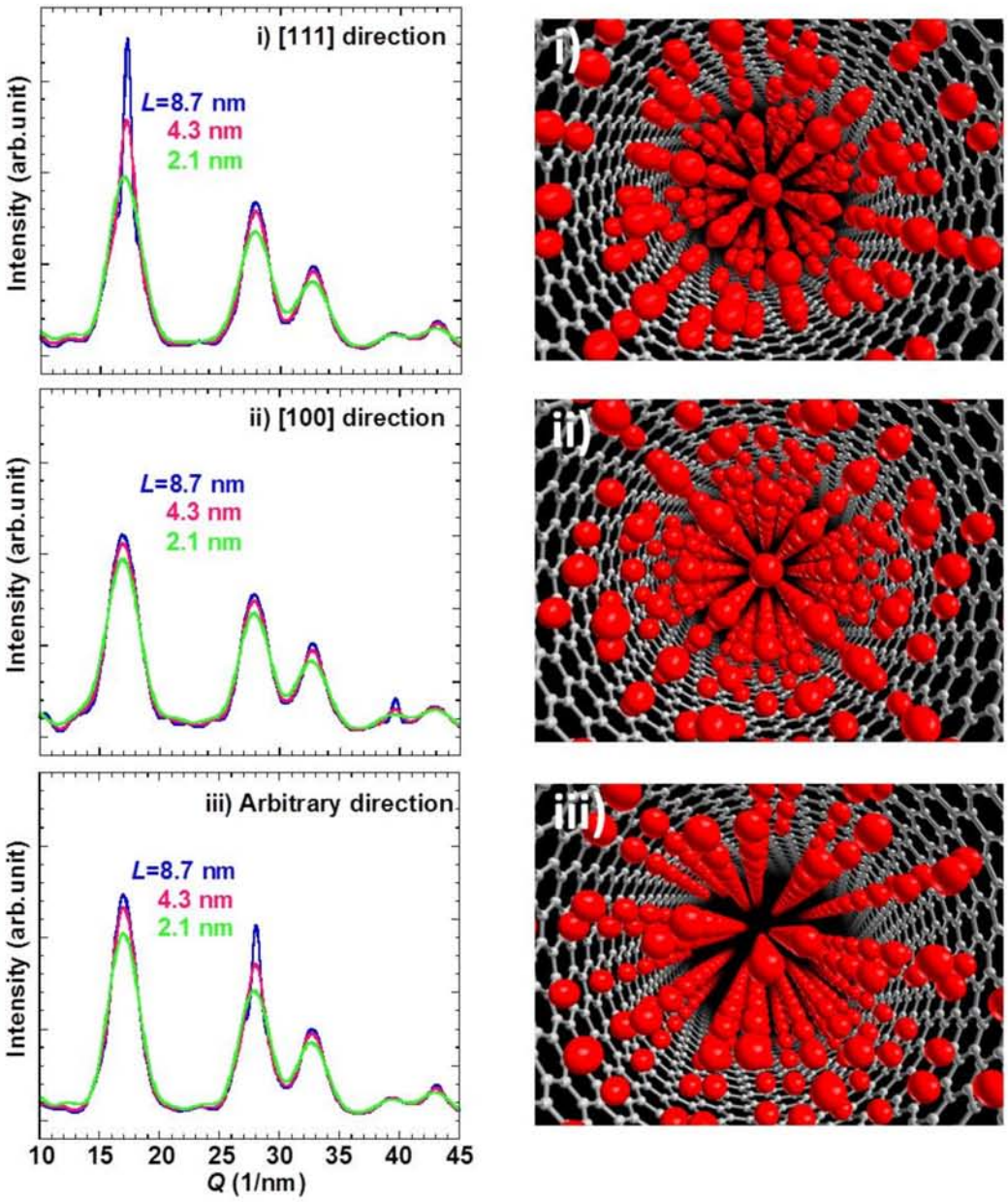

Fig. A1.2. Simulated XRD patterns for ice Ic inside an SWCNT of D=2.40 nm. In the simulations, only contribution from water-water correlation was taken into account. The right panels show the top views of the simulated ice Ic encapsulated inside the SWCNTs. Only the oxygen atoms in water molecules are shown in the figures. The crystal orientations of ice Ic along the tube axis of the SWCNTs are [111], [100], and an arbitrary direction for i), ii), and iii), respectively. The length of the SWCNT, L, was also taken as a parameter.

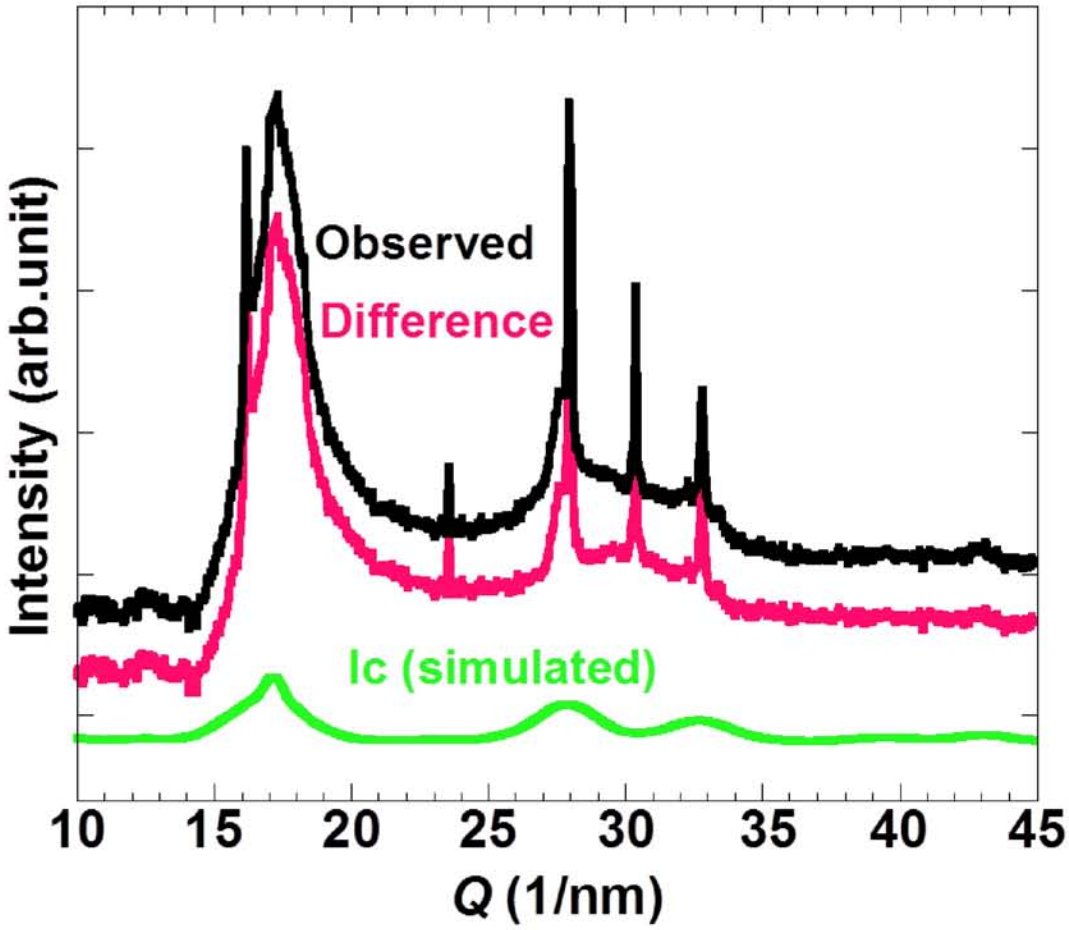

Fig. A1.3. The observed XRD pattern for a water-SWCNT sample with D=2.40 nm at 113 K (black line), simulated pattern for ice Ic inside the SWCNT (green line), and their difference (red line). Here, the pattern for ice Ic is the sum of the three patterns shown in panel i) of **Fig. A1.2**.

2. XRD Simulations for Multilayer Ice Nanotubes or Ice Helixes Confined in SWCNTs

Simulation studies have predicted the existence of complex ice structures such as multilayer ice NTs and multilayer ice helixes inside SWCNTs with diameters more than 1.35 nm, in addition to hollow and filled ice NTs, as mentioned in Section 2.2.3 in Chapter 2. Therefore, we calculated the XRD patterns for such multilayer ice structures inside SWCNTs to discuss whether such ices exist.

As mentioned in refs. 122, ice NTs can be formed by rolling up a two dimensional (2D) square lattice of water molecules, similar to folding a hexagonal-lattice sheet of carbon atoms to form SWCNTs. **Fig. A2.1** shows the schematic illustration of a 2D square lattice to roll up the (n, m) ice NT. Here, the index (n, m) denotes the chirality of the ice NT. An n-gonal ice NT is obtained when the 2D sheet is folded by vector (n, 0). On the other hand, a helical ice NT is formed if the sheet is rolled by vector (n, m) with $m \neq 0$ and $m \neq n$. In the present simulations, a lattice constant of the square lattice was set to be 0.28 nm. **Figure A2.2** shows the simulated XRD patterns for i) an empty SWCNT, ii) a triple-walled ice NT within the SWCNT, iii) the difference between i) and ii), and iv) the triple-walled ice NT without the SWCNT. Each calculated XRD pattern for outer, middle, and inner ice NTs in the triple-walled ice NT is also shown in **Figure A2.3**. As shown in the figure, they have distinct peak patterns. The chirality dependence of the simulated XRD patterns, along with the side views of (20, 0) and (14, 14) ice NTs, are shown in **Figure A2.4**. On comparing the simulated patterns with the side view illustrations, it can be found that the distinct peaks reflect one

dimensional (1D) arrangement of oxygen atoms in ice NTs along their tube direction. More specifically, the peaks at Q~22 nm^{-1} and Q~32 nm^{-1} correspond to the (10) and (11) Bragg peaks for the 2D square lattice shown in **Figure A2.1,** respectively. On the other hand, the observed XRD patterns do not have these peak structures [see **Fig. A1.3** as an example of the observed patterns]. Therefore, in the present study, there is no evidence for the formation of ice NTs and helical ice NTs inside thick SWCNTs of D >1.6 nm.

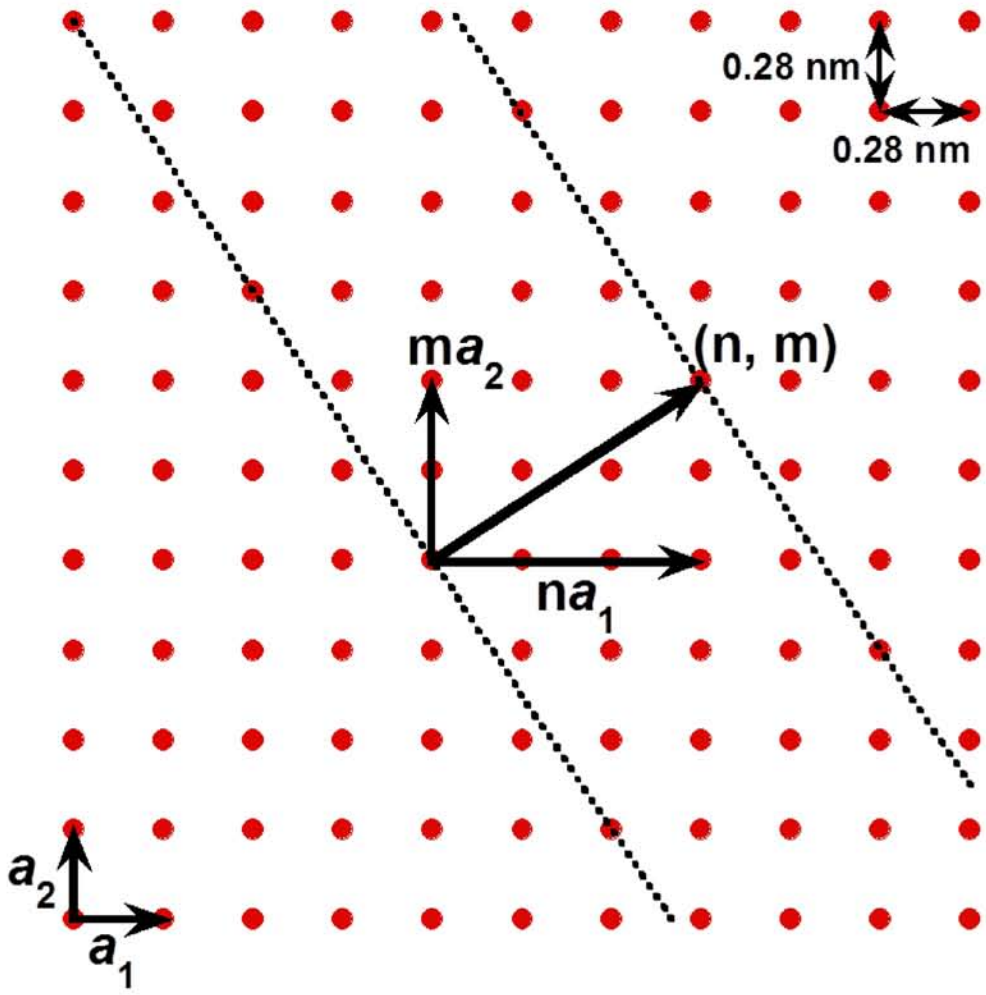

Fig. A2.1. Schematic illustration of a 2D square lattice. An ice NT can be formed by rolling up this 2D sheet. The red circles represent the oxygen atoms in water molecules. The lattice constant was set to be 0.28 nm in the present simulations. The chirality of an ice NT is described by an index (n, m).

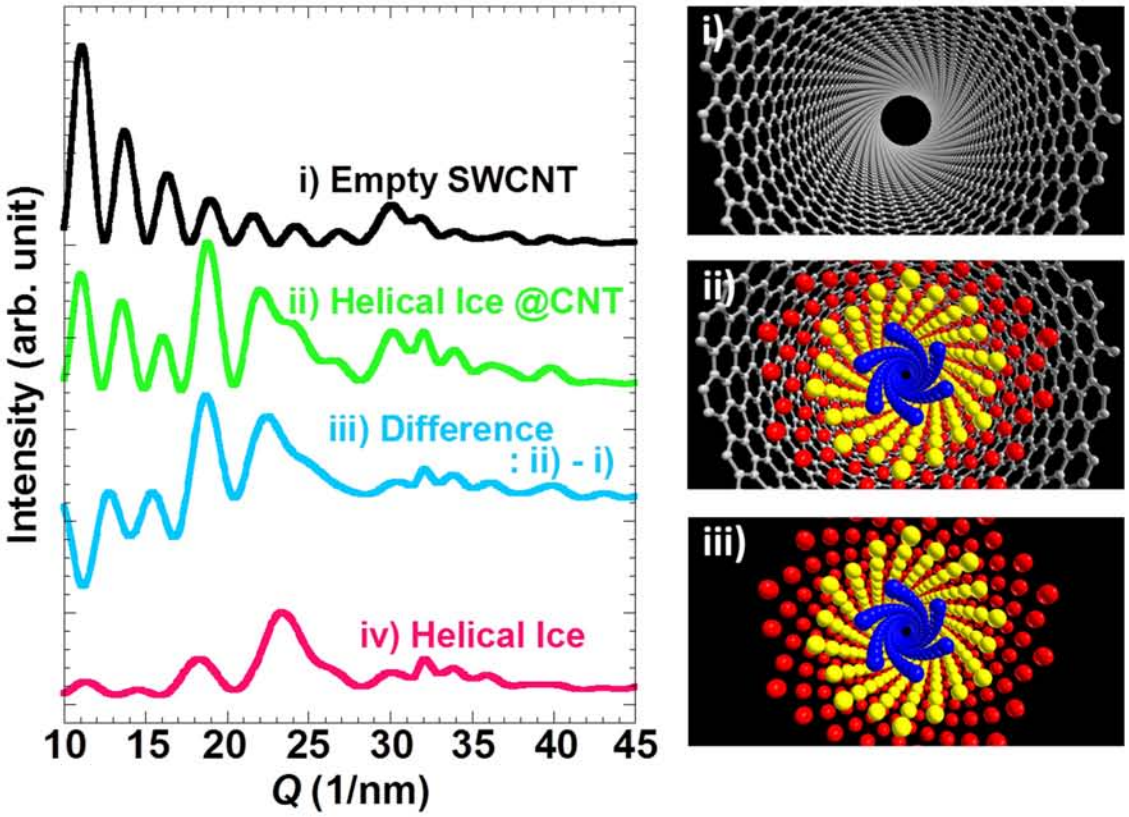

Fig. A2.2. Simulated XRD patterns. i) an empty-SWCNT with D=2.4 nm, ii) a triple-walled ice NT inside the SWCNT, and iii) their difference. The chiralities for outer, middle, and inner walls of the ice NT are (17, 10), (10, 8), and (6, 1), respectively. The pattern for the triple-walled ice NT without the SWCNT, iv), is also shown for comparison. The right panels show the top views of the simulated systems. Colored spheres represent the oxygen atoms in water molecules.

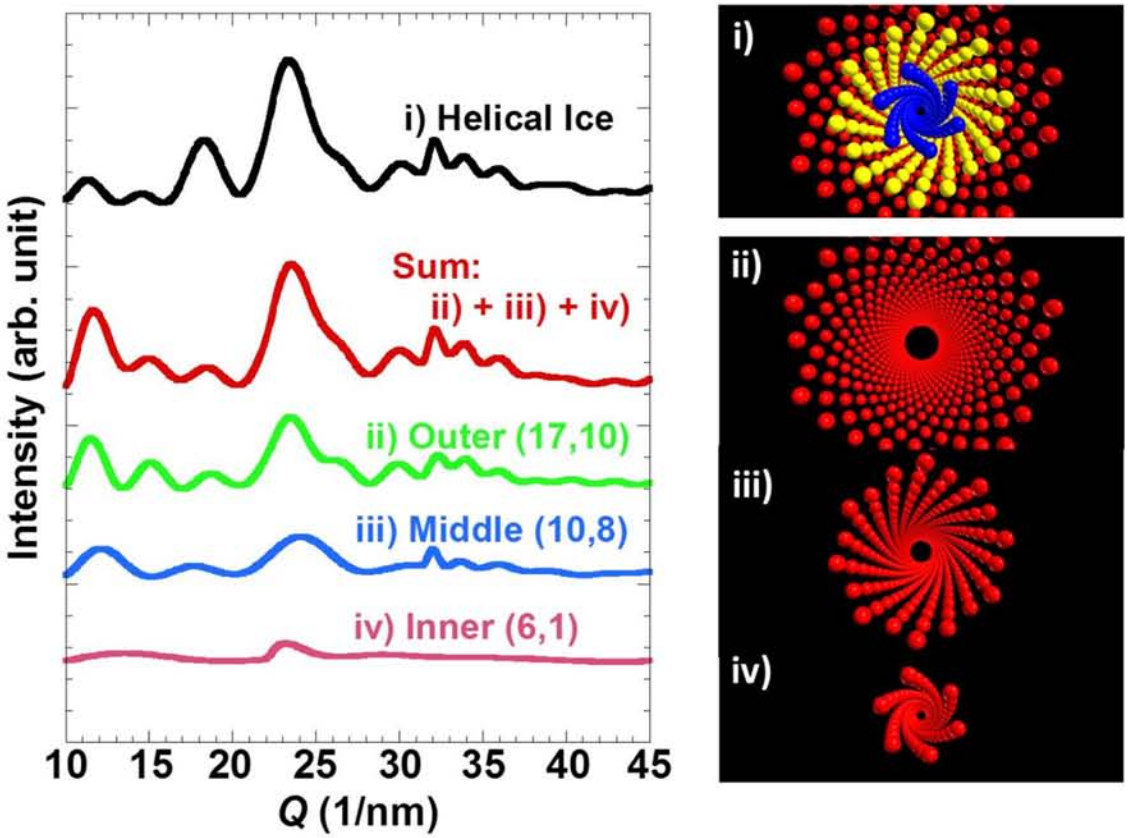

Fig. A2.3. Simulated XRD patterns for ice NTs. i) triple-walled ice NTs, the same data in **Fig. A2.2**. Patterns for outer, middle, and inner walls of the triple-walled ice NT were calculated separately in ii), iii), and iv), respectively. Their sum is also shown in the figure for comparison. The index (n, m) in the figure represents the chirality of the ice NTs. The right panels show the top views of the simulated systems. Only the oxygen atoms in water molecules are shown in the figures as colored spheres.

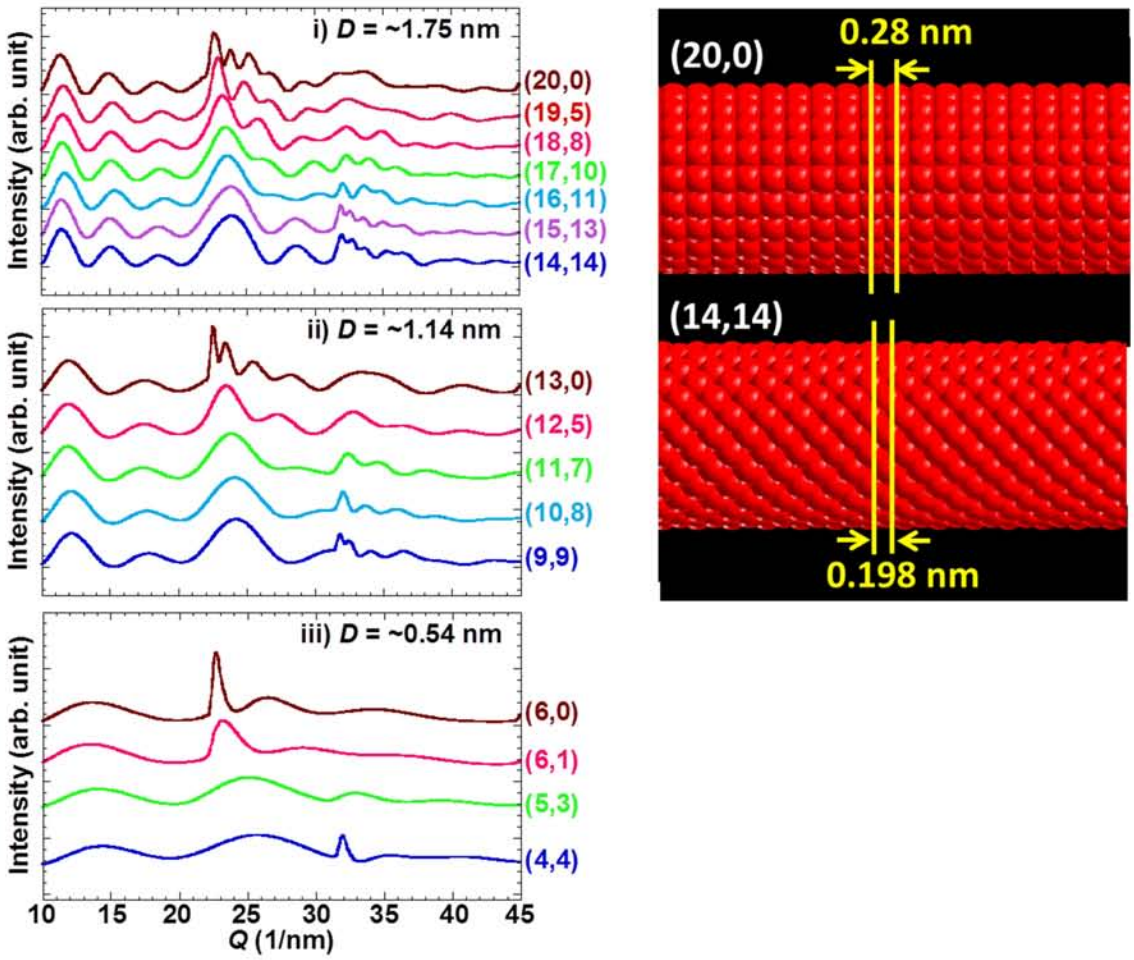

Fig. A2.4. Simulated XRD patterns for ice NTs with different diameters, *D*. The index (n, m) in the figure represents the chirality of the ice NTs. The right panels show the side views of (20, 0) and (14, 14) ice NTs, respectively. Only the oxygen atoms in water molecules are shown in the figures. In the XRD patterns, sharp peaks at Q~22 nm^{-1} and Q~32 nm^{-1} reflect the lattice spacing of 1D arrangement of oxygen atoms along the tube direction of the ice NTs.

3. XRD Patterns for Water in Different Phases

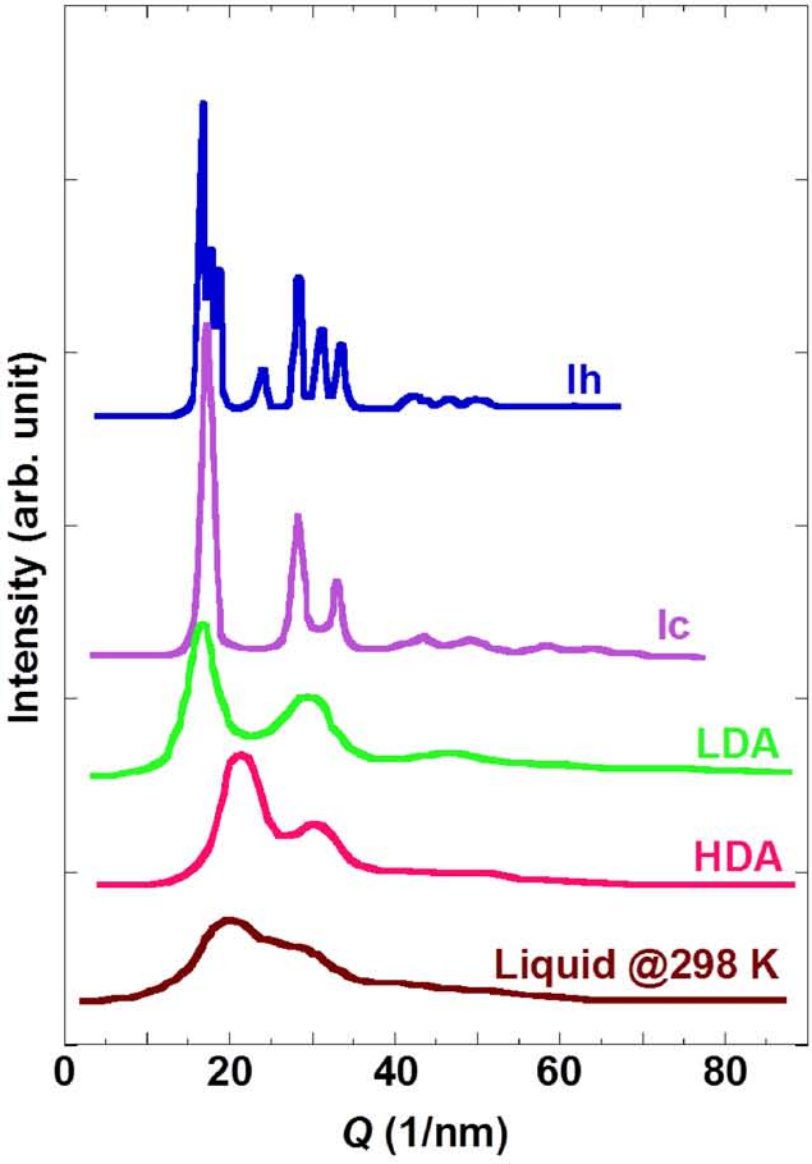

Fig. A3.1. Observed XRD patterns for water in different phases (replotted from ref. 147).

Acknowledgements

I would like to express my appreciation sincerely to all who involved in my Ph.D. study. I owe my deepest gratitude to Professor Yutaka Maniwa for his continuous guidance, extensive discussion, and positive encouragement. He is the one who brought me into the science of water. I wouldn't get to where I am now without his guidance. Associate Professor Kazuyuki Matsuda gave me kind instruction and detailed advice in NMR studies. I was really encouraged by frank and valuable discussion with him. Dr. Hiromichi Kataura and Dr. Takeshi Saito provided us with high-purity SWCNT samples. Also Professor Takashi Kyotani and Associate Professor Hirotomo Nishihara provided ZTC samples. Without their excellent samples, this thesis would not have been possible.

I am deeply grateful to all the members in our research group for their daily support and encouragement. Associate Professor Yasumitsu Miyata, Assistant Professor Yusuke Nakai, and Assistant Professor Hirokazu Sakamoto offered useful comments and advice. Ms. Hitomi Yahiro, Ms. Yu Inami, and Ms. Tomoko Fukuoka, as well as many graduates and undergraduate students contributed greatly to many important experimental results to form the basis of this thesis. I appreciate assistance given by Ms. Tomomi Nonaka. She helped office work, and also made me really relaxed by daily talking.

Finally, I would like to thank my family for their understanding and support for my studying.

References

1. P. G. Debenedetti, and H. E. Stanley, Supercooled and glassywater. *J. Phys.: Condens. Matter* **15**, R1669 (2003).
2. P.G. Debenedetti, H.E. Stanley. Supercooled and glassy water. *Physics Today* **56**, 40 (2003).
3. H.E. Stanley, P. Kumar, L. Xu, Z. Yan, M.G. Mazza, S.V. Buldyrev, S.-H. Chen, F. Mallamace. The puzzling unsolved mysteries of liquid water: Some recent progress. *Physica A* **386**, 729 (2007).
4. A. Angell. Thermodynamics: Highs and lows in the density of water. *Nature Nanotech.* **2**, 396-398 (2007).
5. A. Nilsson, and L.G.M. Pettersson. Perspective on the structure of liquid water. *Chem. Phys.* **389**, 1 (2011).
6. P.H. Poole, F. Sciortino, U. Essmann, and H.E. Stanley. Phase behavior of metastable water. *Nature* **360**, 324 (1992).
7. S. Sastry, P.G. Debenedetti, F. Sciortino, and H.E. Stanley. Singularity-free interpretation of the thermodynamics of supercooled water. *Phys. Rev. E* **53**, 6144 (1996).
8. O. Mishima, H.E. Stanley. The relationship between liquid, supercooled and glassy water. *Nature* **396**, 329 (1998).
9. C.A. Angell. Insights into phases of liquid water from study of its unusual glass-forming properties. *Science* **319**, 582 (2008).
10. K. Stokely, M.G. Mazza, H.E. Stanley, G. Franzese. Effect of hydrogen bond cooperativity on the behavior of water. *Proc. Natl. Acad. Sci. U.S.A.* **107**, 1301 (2010).

11. S. Cerveny, G.A. Schwartz, R. Bergman, J. Swenson. Glass transition and relaxation processes in supercooled water. *Phys. Rev. Lett.* **93**, 245702 (2004).

12. S. Maruyama, K. Wakabayashi, M. Oguni. Thermal properties of supercooled water confined within silica gel pores. *AIP Conf. Proc.* **708**, 675 (2004).

13. L. Liu, S.-H. Chen, A. Faraone, C.-W. Yen, C.-Y. Mou. Pressure dependence of fragile-to-strong transition and a possible second critical point in supercooled confined water. *Phys. Rev. Lett.* **95**, 117802 (2005).

14. F. Mallamace, M. Broccio, C. Corsaro, A. Faraone, L. Liu, C.-Y. Mou, S.-H. Chen. Dynamical properties of confined supercooled water: an NMR study *J. Phys.: Condens. Matter* **18**, S2285 (2006).

15. X.-Q. Chu, A. I. Kolesnikov, A. P. Moravsky, V. Garcia-Sakai, and S.-H. Chen. Observation of a dynamic crossover in water confined in double-wall carbon nanotubes. *Phys. Rev. E* **76**, 021505 (2007).

16. M. Oguni, S. Maruyama, K. Wakabayashi, A. Nagoe. Glass transitions of ordinary and heavy water within silica-gel nanopores. *Chem. Asian J.* **2**, 514 (2007).

17. M. Oguni, Y. Kanke, A. Nagoe, S. Namba. Calorimetric study of water's glass transition in nanoscale confinement, suggesting a value of 210 K for Bulk Water. *J. Phys. Chem. B* **115**, 14023 (2011).

18. C.A. Angell. Liquid fragility and the glass transition in water and aqueous solutions. *Chem. Rev.* **102** ,2627 (2002).

19. K.-I. Murata, H. Tanaka. Liquid–liquid transition without macroscopic

phase separation in a water–glycerol mixture. *Nature Mater.* **11**, 436 (2012).

20. S. A. Lusceac, C. Gainaru, D. A. Ratzke, M. F. Graf, M. Vogel. Secondary water relaxation in a water/dimethyl sulfoxide mixture revealed by deuteron nuclear magnetic resonance and dielectric spectroscopy. *J. Phys. Chem. B* **115**, 11588 (2011).
21. O. Mishima. Volume of supercooled water under pressure and the liquid-liquid critical point. *J. Chem. Phys.* **133,** 144503 (2010).
22. M. Kobayashi and H. Tanaka. Possible link of the V-shaped phase diagram to the glass-forming ability and fragility in a water-salt mixture. *Phys. Rev. Lett.* **106**, 125703 (2011).
23. S. Iijima and T. Ichihashi. Single-shell carbon nanotubes of 1-nm diameter. *Nature* **363**, 603 (1993).
24. H. Nishihara, Q.H. Yang, P.X. Hou, M. Unno, S. Yamauchi, R. Saito, J.I. Paredes, A. Martinez-Alonso, J.M.D. Tascon, Y. Sato, M. Terauchi, T. Kyotani. A possible buckybowl-like structure of zeolite templated carbon. *Carbon* **47**, 1220 (2009).
25. Y. Maniwa, H. Kataura, M. Abe, S. Suzuki, Y. Achiba, H. Kira, and K. Matsuda. Phase transition in confined water inside carbon nanotubes. *J. Phys. Soc. Jpn.* **71**, 2863 (2002).
26. Y. Maniwa, H. Kataura, M. Abe, A. Udaka, S. Suzuki, Y. Achiba, H. Kira, K. Matsuda, H. Kadowaki, and Y. Okabe. Ordered water inside carbon nanotubes: formation of pentagonal to octagonal ice-nanotubes. *Chem. Phys. Lett.* **401**, 534 (2005).

27. Y. Maniwa, K. Matsuda, H. Kyakuno, S. Ogasawara, T. Hibi, H. Kadowaki, S. Suzuki, Y. Achiba, and H. Kataura. Water-filled single-wall carbon nanotubes as molecular nanovalves. *Nat. Mater.* **6**, 135 (2007).

28. F. Mikami, K. Matsuda, H. Kataura, and Y. Maniwa. Dielectric properties of water inside single-walled carbon nanotubes. *ACS Nano.* **3**, 1279 (2009).

29. K. Koga, R.D. Parra, H. Tanaka, and X.C. Zeng. Ice nanotube: What does the unit cell look like? *J. Chem. Phys.* **113**, 5037 (2000).

30. K. Koga, G.T. Gao, H. Tanaka, and X.C. Zeng. Formation of ordered ice nanotubes inside carbon nanotubes. *Nature* **412**, 802 (2001).

31. J. Bai, C.R. Su, R.D. Parra, X.C. Zeng, H. Tanaka, K. Koga, and J.M. Li. Ab initio studies of quasi-one-dimensional pentagon and hexagon ice nanotubes. *J. Chem. Phys.* **118**, 3913 (2003).

32. J.L. Finney. Water? What's so special about it? *Phil Trans R Soc Lond B* 359,1145 (2004).

33. E.F. Burton, and W.F. Oliver. The crystal structure of ice at low temperatures. *Proc. R. Soc. Lond. A* **153**,166 (1936).

34. P. BruÈggeller, and E. Mayer. Complete vitrification in pure liquid water and dilute aqueous solutions. *Nature* **288**, 569 (1980).

35. O. Mishima, L.D. Calvert, and E. Whalley. `Melting' ice I at 77 Kand 10 kbar: a new method of making amorphous solids. *Nature* **310**, 393 (1984).

36. O. Mishima, L.D. Calvert, and E. Whalley. An apparently first-order transition between two amorphous phases of ice induced by pressure. Nature **314**, 76 (1985).

37. S. Klotz, Th. Stra¨ssle, R.J. Nelmes, J.S. Loveday, G. Hamel, G. Rousse, B. Canny, J.C. Chervin, and A.M. Saitta. Nature of the polyamorphic transition in ice under pressure. *Phys. Rev. Lett.* **94**, 025506 (2005).

38. K. Ito, C.T. Moynihan, and C.A. Angell. Thermodynamic determination of fragility in liquids and a fragile-to-strong liquid transition in water. Nature **398**, 492 (1999).

39. V. Velikov, S. Borick, C.A. Angell. The glass transition of water, based on hyperquenching experiments. *Science* **294**, 2335 (2001).

40. S. Cerveny, G.A. Schwartz, R. Bergman, J. Swenson. Glass transition and relaxation processes in supercooled water. *Phys. Rev. Lett.* **93**, 245702 (2004).

41. J.L. Finney, A. Hallbrucker, I. Kohl, A.K. Soper, and D.T. Bowron. Structures of high and low density amorphous ice by neutron diffraction. Phys. Rev. Lett. **88**, 225503 (2002).

42. R.J. Speedy. Stability-limit conjecture. An interpretation of the properties of water. *J. Phys. Chem.* **86**, 982 (1982).

43. F. Sciortino, P.H. Poole, U. Essmann, and H.E. Stanley. Line of compressibility maxima in the phase diagram of supercooled water. *Phys. Rev. E* **55**, 727 (1997).

44. H.E. Stanley, C.A. Angell, U. Essmann, M. Hemmati, P.H. Poole, and F.

Sciortino. Is there a second critical point in liquid water? *Physica A* **205**, 122 (1994).

45. I. Brovchenko, A. Geiger, and A. Oleinikova. Liquid-liquid phase transitions in supercooled water studied by computer simulations of various water models. J. Chem. Phys. **123**, 044515 (2005).

46. I. Brovchenko, and A. Oleinikova. Multiple phases of liquid water. Chem. Phys. Chem. **9**, 2660 (2008).

47. T.M. Truskett, P.G. Debenedetti, S. Sastry, and S. Torquato. A single-bond approach to orientation-dependent interactions and its implications for liquid water. *J. Chem. Phys.* **111**, 2647 (1999).

48. C.A. Angell. Glass transition dynamics in water and other tetrahedral liquids: 'order–disorder' transitions versus 'normal' glass transitions. *J. Phys.: Condens. Matter* **19**, 205112 (2007).

49. M. Tadokoro, S. Fukui, T. Kitajima, Y. Nagao, S. Ishimaru, H. Kitagawa, K. Isobe, and K. Nakasuji. Structures and phase transition of multi-layered water nanotube confined to nanochannels. *Chem. Commun.* 1274 (2006).

50. M. Tadokoro, T. Ohhara, Y. Ohhata, T. Suda, Y. Miyasato, T. Yamada, T. Kikuchi, I. Tanaka, K. Kurihara, M. Oguni, K. Nakasuji, O. Yamamuro, and K. Ryota. Anomalous water molecules and mechanistic effects of water nanotube clusters confined to molecular porous crystals. *J. Phys. Chem. B* **114**, 2091 (2010).

51. H. Yui, Y. Guo, K. Koyama, T. Sawada, G. John, B. Yang, M. Masuda, and T. Shimizu. Local environment and property of water inside the

hollow cylinder of a lipid nanotube. *Langmuir* **21**, 721 (2005).

52. K. Morishige and K. Nobuoka. X-ray diffraction studies of freezing and melting of water confined in a mesoporous adsorbent (MCM-41). *J. Chem. Phys.* **107**, 6965 (1997).

53. K. Morishige and K. Kawano. Freezing and melting of water in a single cylindrical pore: The pore-size dependence of freezing and melting behavior. *J. Chem. Phys.* **110**, 4867 (1999).

54. A. Schreiber, I. Ketelsen and G.H. Findenegg. Melting and freezing of water in ordered mesoporous silica materials. *Phys. Chem. Chem. Phys.* **3**, 1185 (2001).

55. S. Ja¨hnert, F.V. Cha´vez, G.E. Schaumann, A. Schreiber, M. Scho¨nhoff, and G.H. Findenegg. Melting and freezing of water in cylindrical silica nanopores. *Phys. Chem. Chem. Phys.* **10**, 6039 (2008).

56. C. E. Bertrand, Y. Zhang, and S.-H. Chen. Deeply-cooled water under strong confinement: neutron scattering investigations and the liquid–liquid critical point hypothesis. *Phys. Chem. Chem. Phys.* **15**, 721 (2013).

57. J. Martı´ and M.C. Gordillo. Temperature effects on the static and dynamic properties of liquid water inside nanotubes. *Phys. Rev. E* **64**, 021504 (2001).

58. N.E. Levinger. Water in Confinement. *Science* **298**, 1722 (2002).

59. M.S.P. Sansom and P.C. Biggin. Water at the nanoscale. *Nature* **414**, 156 (2001).

60. V. Buch, J.P. Devlin (Eds.), Water in Confining Geometries.

Springer-Verlag, Berlin, 2003.

61. Y. Harano and M. Kinoshita. Translational-entropy gain of solvent upon protein folding. *Biophys. J.* **89**, 2701 (2005).

62. H. Sui, B.G. Han, J.K. Lee, P. Walian, and B.K. Jap. Structural basis of water-specific transport through the AQP1 water channel. *Nature* **414**, 872 (2001).

63. K. Murata, K. Mitsuoka, T. Hirai, T. Walz, P. Agre, J.B. Heymann, A. Engel, and Y. Fujiyoshi. Structural determinants of water permeation through aquaporin-1. *Nature* **407**, 599 (2000).

64. K.A. Jackson and B. Chalmers. Freezing of liquids in porous media with special reference to frost heave in soils. *J. Appl. Phys.* **29**, 1178 (1958).

65. E.J.M. Hensen and B. Smit. Why Clays Swell. *J. Phys. Chem. B* **106**, 12664 (2002).

66. T.J. Tambach, P.G. Bolhuis,E.J.M. Hensen, and B. Smit. Hysteresis in Clay Swelling Induced by Hydrogen Bonding: Accurate Prediction of Swelling States. *Langmuir* **22**, 1223 (2006).

67. A. Noy, H.G. Parka, F. Fornasiero, J.K. Holt, C.P. Grigoropoulos, and O. Bakajin. Nanofluidics in carbon nanotubes. *Nano Today* **2**, 22 (2007).

68. C. Luo, W. Fa, J. Zhou, J. Dong, and X.C. Zeng. Ferroelectric ordering in ice nanotubes confined in carbon nanotubes. *Nano Lett.* **8 (9)**, 2607 (2008).

69. T.D. Nguyen, H.R. Tseng, P.C. Celestre, A.H. Flood, Y. Liu, J.F. Stoddart, and J.I. Zink. A reversible molecular valve. *Proc. Natl. Acad. Sci. U.S.A.* **102**, 10029 (2005).

70. M. Tanaka, and A. Mochizuki. Clarification of the blood compatibility mechanism by controlling the water structure at the blood-poly (meth) acrylate interface. *J. Biomater. Sci. Polymer Ed.* **21**, 1849 (2010).

71. S.I. Outcalt. An algorithm for needle ice growth. *Water Resources Research* **7**, 394 (1971).

72. R.P. Gilpin. A model for the prediction of ice lensing and frost heave in soils. *Water Resources Research* **16**, 918 (1980).

73. C.T. Kresge, M.E. Leonowicz, W.J. Roth, J.C. Vartuli, and J. S. Beck. Ordered mesoporous molecular sieves synthesized by a liquid-crystal template mechanism. *Nature* **359**, 710 (1992).

74. J.S. Beck, J.C. Vartuli, W.J. Roth, M.E. Leonowicz, C.T. Kresge, K.D. Schmitt, C.T.W. Chu, D.H. Olson, E.W. Sheppard, S.B. McCullen, J.B. Higgins, and J.L. Schlenker. A new family of mesoporous molecular sieves prepared with liquid crystal templates. *J. Am. Chem. Soc.* **114**, 10834 (1992).

75. P.G. Debenedetti, F.H. Stillinger. Supercooled liquids and the glass transition. *Nature* **410**, 259 (2001).

76. C.A. Angell. Glass formation and glass transition in supercooled liquids, with insights from study of related phenomena in crystals. *J. Non-Cryst. Solids* **354**, 4703 (2008).

77. J. Swenson, H. Jansson, R. Bergman. Relaxation processes in supercooled confined water and implications for protein dynamics. *Phys. Rev. Lett.* **96**, 247802 (2006).

78. J. Hedstrom, J. Swenson, R. Bergman, H. Jansson, S. Kittaka. Does

confined water exhibit a fragile-to-strong transition? *Eur. Phys. J. Special Topics* **141**, 53 (2007).

79. A.K. Soper. Density profile of water confined in cylindrical pores in MCM-41 silica. *J. Phys.: Condens. Matter* **24**, 064107 (2012).
80. S. Iijima. Helical microtubles of graphitic carbon. *Nature* **354**, 56 (1991).
81. D.S. Bethune, C.H. Kiang, M.S. de Vries, G. Gorman, R. Savoy, J. Vasquez, and R. Beyers. Cobalt-catalysed growth of carbon nanotubes with single-atomic-layer walls. *Nature* **363**, 605 (1993).
82. Y. Maniwa, Y. Kumazawa, Y. Saito, H. Tou, H. Kataura, H. Ishii, S. Suzuki, Y. Achiba, A. Fujiwara, and H. Suematsu. Anomaly of x-ray diffraction profile in single-walled carbon nanotubes. *Jpn. J. Appl. Phys.* **38**, L668 (1999).
83. A.I. Kolesnikov, J.M. Zanotti, C.K. Loong, P. Thiyagarajan, A.P. Moravsky, R.O. Loutfy, and C. J. Burnham. Anomalously soft dynamics of water in a nanotube: A revelation of nanoscale confinement. *Phys. Rev. Lett.* **93**, 035503 (2004).
84. S. Ghosh, K.V. Ramanathan, and A.K. Sood. Water at nanoscale confined in single-walled carbon nanotubes studied by NMR. *Europhys. Lett.* **65**, 678 (2004).
85. K. Matsuda, T. Hibi, H. Kadowaki, Y. Maniwa, and H. Kataura. Water dynamics inside single-wall carbon nanotubes: NMR observations. *Phys. Rev. B* **74**, 073415 (2006).
86. W. Sekhaneh, M. Kotecha, U. Dettlaff-Weglikowska, and W.S. Veeman.

High resolution NMR of water absorbed in single-wall carbon nanotubes. *Chem. Phys. Lett.* **428**, 143 (2006).

87. H.J. Wang, X.K. Xi, A. Kleinhammes, Y. Wu. Temperature-induced hydrophobic-hydrophilic transition observed by water adsorption. *Science* **322**, 80 (2008).

88. A. Das, S. Jayanthi, H.S.M. V. Deepak, K.V. Ramanathan, A. Kumar, C. Dasgupta, and A.K. Sood. Single-file diffusion of confined water inside SWNTs: An NMR study. *ACS Nano*, **4**, 1687 (2010).

89. O. Byl, J.C. Liu, Y. Wang, W.L. Yim, J.K. Johnson, and J.T. Yates, Jr.. Unusual Hydrogen Bonding in Water-Filled Carbon Nanotubes. *J. Am. Chem. Soc.* **128**, 12090 (2006).

90. S. Cambre´, B. Schoeters, S. Luyckx, E. Goovaerts, and W. Wenseleers. Experimental observation of single-file water filling of thin single-wall carbon nanotubes down to chiral index (5,3). *Phys. Rev. Lett.* **104**, 207401 (2010).

91. A. Striolo, A.A. Chialvo, K.E. Gubbins, and P.T. Cummings. Water in carbon nanotubes: Adsorption isotherms and thermodynamic properties from molecular simulation. *J. Chem. Phys.* **122**, 234712 (2005).

92. A. Striolo, A.A. Chialvo, P.T. Cummings, and K.E. Gubbins. Simulated water adsorption in chemically heterogeneous carbon nanotubes. *J. Chem. Phys.* **124**, 074710 (2006).

93. N. Naguib, H. Ye, Y. Gogotsi, A.G. Yazicioglu, C.M. Megaridis, and M. Yoshimura. Observation of water confined in nanometer channels of closed carbon nanotubes. *Nano Lett.* **4**, 2237 (2004).

94. D. Mattia and Y. Gogotsi. Review: static and dynamic behavior of liquids inside carbon nanotubes. *Microfluid Nanofluid* **5**, 289 (2008).

95. M.C. Gordillo and J. Martí. Hydrogen bond structure of liquid water confined in nanotubes. *Chem. Phys. Lett.* **329**, 341 (2000).

96. I. Hanasaki and A. Nakatani. Hydrogen bond dynamics and microscopic structure of confined water inside carbon nanotubes. *J. Chem. Phys.* **124**, 174714 (2006).

97. A.I. Skoulidas, D.M. Ackerman, J.K. Johnson, and D.S. Sholl. Rapid Transport of Gases in Carbon Nanotubes. *Phys. Rev. Lett.* **89**, 185901 (2002).

98. A. Kalra, S. Garde, and G. Hummer. Osmotic water transport through carbon nanotube membranes. *Proc. Natl. Acad. Sci. U.S.A.* **100**, 10175 (2003).

99. M. Majumder, N. Chopra, R. Andrews, and B.J. Hinds. Enhanced flow in carbon nanotubes. *Nature* **438**, 44 (2005).

100. J.K. Holt, H.G. Park, Y. Wang, M. Stadermann, A.B. Artyukhi, C.P. Grigoropoulos, A. Noy, and O. Bakajin. Fast mass transport through sub–2-nanometer carbon nanotubes. *Science* **312**, 1034 (2006).

101. S. Joseph and N.R. Aluru. Why are carbon nanotubes fast transporters of water? *Nano Lett.* **8**, 452 (2008).

102. C. Dellago, M.M. Naor, and G. Hummer. Proton transport through water-filled carbon nanotubes. *Phys. Rev. Lett.* **90**, 105902 (2003).

103. G. Hummer, J.C. Rasaiah, and J.P. Noworyta. Water conduction through the hydrophobic channel of a carbon nanotube. *Nature* **414**, 188

(2001).

104. C. Peter, and G. Hummer. Ion transport through membrane-spanning nanopores studied by molecular dynamics. *Biophys. J.* **89**, 2222 (2005).

105. J.H. Park, S.B. Sinnott, and N. R. Aluru. Ion separation using a Y-junction carbon nanotube. *Nanotechnology* **17**, 895 (2006).

106. S. Joseph, R.J. Mashl, E. Jakobsson, and N.R. Aluru. Electrolytic transport in modified carbon nanotubes. *Nano Lett.* **3**, 1399 (2003).

107. B. Corry. Designing carbon nanotube membranes for efficient water desalination. *J. Phys. Chem. B* **112**, 1427 (2008).

108. A. Kalra, G. Hummer, and S. Garde. Methane Partitioning and transport in hydrated carbon nanotubes. *J. Phys. Chem. B*, **108**, 544 (2004).

109. X. Gong, J. Li, H. Lu, R. Wan, J. Li, J. Hu, and H. Fang. A charge-driven molecular water pump. *Nature Nanotech.* **2**, 709 (2007).

110. P. Kral and M. Shapiro. Nanotube electron drag in flowing liquids. *Phys. Rev. Lett.* **86**, 131 (2001).

111. S. Ghosh, A. K. Sood, and N. Kumar. Carbon nanotube flow sensors. *Science* **299**, 1042 (2003).

112. Y. Zhao, L. Song, K. Deng, Z. Liu, Z. Zhang, Y. Yang, C. Wang, H. Yang, A. Jin, Q. Luo, C. Gu, S. Xie, and L. Sun. Individual water-filled single-walled carbon nanotubes as hydroelectric power converters. *Adv. Mater.* **20**, 1772 (2008).

113. T. Kurita, S. Okada, and A. Oshiyama. Energetics of ice nanotubes and their encapsulation in carbon nanotubes from density-functional theory.

Phys. Rev. B **75**, 205424 (2007).

114. B.K. Agrawal, V. Singh, A. Pathak, and R. Srivastava. Ab initio study of ice nanotubes in isolation or inside single-walled carbon nanotubes. *Phys. Rev. B* **75**, 195420 (2007).

115. W.H. Noon, K.D. Ausman, R.E. Smalley, and J.Ma. Helical ice-sheets inside carbon nanotubes in the physiological condition. *Chem. Phys. Lett.* **355**, 445 (2002).

116. R. Schmidt, E.W. Hansen, M. Stocker, D. Akporiaye, and O.H. Ellestad. Pore size determination of MCM-41 mesoporous materials by means of ^{1}H NMR spectroscopy, N_2 adsorption, and HREM. A preliminary study. *J. Am. Chem. Soc.* **117**, 4049 (1995).

117. M.S.-Bartkowiak, G. Dudziak, R. Sikorski, R. Gras, K.E. Gubbins and R. Radhakrishnan. Dielectric studies of freezing behavior in porous materials: Water and methanol in activated carbon fibres. *Phys. Chem. Chem. Phys.* **3**, 1179 (2001).

118. M.S.-Bartkowiak, G. Dudziak, R. Sikorski, R. Gras, R. Radhakrishnan, and K.E. Gubbins. Melting/freezing behavior of a fluid confined in porous glasses and MCM-41: Dielectric spectroscopy and molecular simulation. *J. Chem. Phys.* **114**, 950 (2001).

119. Z. Liu, K. Muldrew, R.G. Wan, and J.A. W. Elliott. Measurement of freezing point depression of water in glass capillaries and the associated ice front shape. *Phys. Rev. E* **67**, 061602 (2003), and references therein.

120. M.S.-Bartkowiak, M. Jazdzewska, L.L. Huang, and K.E. Gubbins.

Melting behavior of water in cylindrical pores: carbon nanotubes and silica glasses. *Phys. Chem. Chem. Phys.* **10**, 4909 (2008).

121. J. Shiomi, T. Kimura, and S. Maruyama. Molecular dynamics of ice-nanotube formation inside carbon nanotubes. *J. Phys. Chem. C* **111**, 12188 (2007).
122. D. Takaiwa, I. Hatano, K. Koga, and H. Tanaka. Phase diagram of water in carbon nanotubes. *Proc. Natl. Acad. Sci. U.S.A.* **105,** 39 (2008).
123. J. Bai, J. Wang, and X.C. Zeng. Multiwalled ice helixes and ice nanotubes. *Proc. Natl. Acad. Sci. U.S.A.* **103**, 19664 (2006).
124. S.O. Diallo, M.Jazdzewska, J.C. Palmer, E. Mamontov, K.E. Gubbins, and M. Sliwinska-Bartkowiak. Dynamics of nanoconfined water under pressure. *Phys. Rev. E* **88**, 022316 (2013).
125. K. Yanagi, Y. Miyata, and H. Kataura. Optical and conductive characteristics of metallic single-wall carbon nanotubes with three basic colors; Cyan, magenta, and yellow. *Appl. Phys. Express* **1**, 034003 (2008).
126. T. Saito, W.C. Xu, S. Ohshima, H. Ago, M. Yumura, and S. Iijima. Supramolecular catalysts for the gas-phase synthesis of single-walled carbon nanotubes. *J. Phys. Chem. B* **110**, 5849 (2006).
127. T. Saito, S. Ohshima, T. Okazaki, S. Ohmori, M. Yumura, and S. Iijima. Selective diameter control of single-walled carbon nanotubes in the gas-phase synthesis. *J. Nanosci. Nanotechnol.* **8**, 6153 (2008).
128. A. Thess, R. Lee, P. Nikolaev, H.D. Pierre, J. Robert, C. Xu, Y.H. Lee, S.G. Kim, D.T. Colbert, G. Scuseria, D. Tomanek, J.E. Fischer, and R.E.

Smalley. Crystalline ropes of metallic carbon nanotubes. *Science* **273**, 483 (1996).

129. H. Kadowaki, A. Nishiyama, K. Matsuda, Y. Maniwa, S. Suzuki, Y. Achiba, and H. Kataura. Rietveld analysis and maximum entropy method of powder diffraction for bundles of single-walled carbon nanotubes. *J. Phys. Soc. Jpn.* **74**, 2990 (2005).
130. A. Abragam, Principles of nuclear Magnetism, Oxford University Press, Oxford, 1985, p. 313 and p. 424.
131. J.A. Jackson, S.W. Rabideau. Deuteron magnetic resonance in polycrystalline heavy ice (D_2O). *J. Chem. Phys.* **41**, 4008 (1964).
132. M.J. O'Neill. Measurement of specific heat functions by differential scanning calorimetry. *Anal. Chem.* **38**, 1331 (1966).
133. W.L. Jorgensen, J. Chandrasekhar, J.D. Madura, R.W. Impey, and M.L. Klein. Comparison of simple potential functions for simulating liquid water. *J. Chem. Phys.* **79**, 926 (1983).
134. H.J.C. Berendsen, J.R. Grigera, T.P. Straatsma. The missing term in effective pair potentials. *J. Phys. Chem.* **91**, 6269 (1987).
135. D. van der Spoel, P.J. van Maaren, and H.J.C. Berendsen. A systematic study of water models for molecular simulation: Derivation of water models optimized for use with a reaction field. *J. Chem. Phy.* **108**, 10220 (1998).
136. P. Mark and L. Nilsson. Structure and dynamics of the TIP3P, SPC, and SPC/E water models at 298 K. *J. Phys. Chem. A* 105, 9954 (2001).
137. G. Hinze, G. Diezemann, Th. Basche. Rotational correlation functions of

single molecules. *Phys. Rev. Lett.* **93**, 203001 (2004).

138. C. Kittel, Introduction to Solid State Physics, 7th ed., Wiley, New York, 1996.

139. Y. Maniwa, Y. Kumazawa, Y. Saito, H. Tou, H. Kataura, H. Ishii, S. Suzuki, Y. Achiba, A. Fujiwara, and H. Suematsu. Gas storage in single-walled carbon nanotubes. *Mol. Cryst. Liq. Cryst.* **340**, 671 (2000).

140. A. Zahab, L. Spina, and P. Poncharal. Water-vapor effect on the electrical conductivity of a single-walled carbon nanotube mat. *Phys. Rev. B* **62**, 10000 (2000).

141. R. Pati, Y. Zhang, S. K. Nayak, and P. M. Ajayan. Effect of H_2O adsorption on electron transport in a carbon nanotube. *Appl. Phys. Lett.* **81**, 2638 (2002).

142. H. Yokoi, F. Okabe, A. Watanabe, Y. Hayamizu, and K. Hata. FT-IR study of water adsorption effect on the electronic states of single-walled carbon nanotube. *AIP Conference Proceeding Series* **1399**, 805 (2011).

143. K. Yanagi, H. Udoguchi, S. Sagitani, Y. Oshima, T. Takenobu, H. Kataura, T. Ishida, K. Matsuda, and Y. Maniwa. Transport mechanisms in metallic and semiconducting single-wall carbon nanotube. *ACS Nano* **4**, 4027 (2010).

144. In the present paper, the peak intensity was replotted after correction of the linearity of the IP reader in the XRD measurements, and is slightly different from that in the previous paper (ref. 145).

145. H. Kyakuno, K. Matsuda, H. Yahiro, T. Fukuoka, Y. Miyata, K. Yanagi, Y. Maniwa, H. Kataura, T. Saito, M. Yumura, and S. Iijima. Global

phase diagram of water confined on the nanometer scale. *J. Phys. Soc. Jpn.* **79**, 083802 (2010).

146. Z. Liu, K. Muldrew, R.G. Wan, and J.A. W. Elliott. Measurement of freezing point depression of water in glass capillaries and the associated ice front shape. *Phys. Rev. E* **67**, 061602 (2003), and references therein.

147. L. Bosio, G. P. Johari, and J. Teixeira. X-ray study of high-density amorphous water. *Phys. Rev. Lett.* **56**, 460 (1986).

148. C. U. Kim, B. Barstow, M. W. Tate, and S. M. Gruner. Evidence for liquid water during the high-density to low-density amorphous ice transition. *Proc. Natl. Acad. Sci. U.S.A.* **106**, 4596 (2009).

149. P.W. Deutsch and T.D. Stanik. A temperature dependent simulation of the x-ray powder spectrum of ice Ih using metropolis monte carlo sampling. J. Chem. Phys. **85**, 4660 (1986).

150. R. Kurita, K.-I. Murata, and H. Tanaka. Control of fluidity and miscibility of a binary liquid mixture by the liquid–liquid transition. *Nature Mater.* **7**, 647 (2008).

151. J. H. Roh, J. E. Curtis, S. Azzam, V. N. Novikov, I. Peral, Z. Chowdhuri, R. B. Gregory, and A. P. Sokolov. Influence of Hydration on the Dynamics of Lysozyme. *Biophys. J.* **91**, 2573 (2006).

152. M. Vogel. Origins of Apparent Fragile-to-Strong Transitions of Protein Hydration Waters. *Phys. Rev. Lett.* **101**, 225701 (2008).

153. Y. Maniwa, R. Fujiwara, H. Kira, H. Tou, H. Kataura, S. Suzuki, Y. Achiba, E. Nishibori, M. Takata, M. Sakata, A. Fujiwara, H. Suematsu.

Thermal expansion of single-walled carbon nanotube (SWNT) bundles: X-ray diffraction studies. *Phys. Rev. B* **64**, 241402 (2001).

154. H. Sato, N. Kawatsu, T. Enoki, M. Endo, R. Kobori, S. Maruyama, K. Kaneko. Drastic effect of water-adsorption on the magnetism of carbon nanomagnets. *Solid State Commun.* **125**, 641 (2003).
155. V.F. Petrenko, R.W. Whitworth, Physics of Ice, Oxford University Press, Oxford, 2002, p. 40.
156. K. Komatsu, T. Nagamiya. Theory of the specific heat of graphite. *J. Phys. Soc. Jpn.* **6**, 438 (1951).
157. E. Tombari, C. Ferrari, G. Salvetti. Heat capacity anomaly in a large sample of supercooled water. *Chem. Phys. Lett.* **300**, 749 (1999).
158. J. Ropp, C. Lawrence, T. C. Farrar, J. L. Skinner. Rotational motion in liquid water is anisotropic: A nuclear magnetic resonance and molecular dynamics simulation study. *J. Am. Chem. Soc.* **123**, 8047 (2001).
159. J. Rault, R. Neffati, P. Judeinstein. Melting of ice in porous glass: why water and solvents confined in small pores do not crystallize? *Eur. Phys. J. B* **36**, 627 (2003).
160. A.K. Soper. Structural transformations in amorphous ice and supercooled water and their relevance to the phase diagram of water *Mol. Phys.* **106**, 2053 (2008).
161. Y. Tu, J. Tersoff, G. Grinstein. Properties of a continuous random network model for amorphous systems. *Phys. Rev. Lett.* **81**, 4899 (1998).
162. I. Brovchenko, A. Oleinikova. Effect of confinement on the liquid-liquid

phase transition of supercooled water. *J. Chem. Phys.* **126**, 214701 (2007).

163. E. Mamontov, A. Faraone, E. W. Hagaman, K. S. Han, E. Fratini. A low-temperature crossover in water dynamics in an aqueous LiCl solution: diffusion probed by neutron spin-echo and nuclear magnetic resonance. *J. Phys. Chem. B* **114**, 16737 (2010).

Supplement

List of Published Papers

[1] Water-filled single-wall carbon nanotubes as molecular nanovalves.
Y. Maniwa, K. Matsuda, H. Kyakuno, S. Ogasawara, T. Hibi, H. Kadowaki, S. Suzuki, Y. Achiba, and H. Kataura.
Nat. Mater. **6**, 135-141 (2007).

[2] Global Phase Diagram of Water Confined on the Nanometer Scale.
H. Kyakuno, K. Matsuda, H. Yahiro, T. Fukuoka, Y. Miyata, K. Yanagi, Y. Maniwa, H. Kataura, T. Saito, M. Yumura, and S. Iijima.
J. Phys. Soc. Jpn. **79**, 083802 (2010).

[3] Confined water inside single-walled carbon nanotubes: Global phase diagram and effect of finite length.
H. Kyakuno, K. Matsuda, H. Yahiro, Y. Inami, T. Fukuoka, Y. Miyata, K. Yanagi, Y. Maniwa, H. Kataura, T. Saito, M. Yumura, and S. Iijima.
J. Chem. Phys. **134**, 244501 (2011).

[4] Single Chirality Extraction of Single-Wall Carbon Nanotubes for the Encapsulation of Organic Molecules.
M. Kawai, H. Kyakuno, T. Suzuki, T. Igarashi, H. Suzuki, T. Okazaki, H. Kataura, Y. Maniwa, and K. Yanagi.
J. Am. Chem. Soc. **134**, 9545-9548 (2012).

[5] ^{13}C-NMR Shift of Highly Concentrated Metallic and Semiconducting Single-Walled Carbon Nanotubes.
K. Matsuda, K. Yanagi, H. Kyakuno, S. Sagitani, H. Kataura, and Y. Maniwa.
J. Phys. Soc. Jpn. **82**, 015001 (2013).

[6] Amorphous Water in Three-Dimensional Confinement of Zeolite–templated Carbon.
H. Kyakuno, K. Matsuda, Y. Nakai, T. Fukuoka, Y. Maniwa, H. Nishihara, and T. Kyotani.
Chem. Phys. Lett. **571**, 54-60 (2013).